Copyright © 2005, by the author(s).
All rights reserved.

Permission to make digital or hard copies of all or part of this work for personal or classroom use is granted without fee provided that copies are not made or distributed for profit or commercial advantage and that copies bear this notice and the full citation on the first page. To copy otherwise, to republish, to post on servers or to redistribute to lists, requires prior specific permission.

MODELING INNOVATIONS IN EUV AND NANOIMPRINT LITHOGRAPHY

by

Yunfei Deng

Memorandum No. UCB/ERL M05/27

1 June 2005

MODELING INNOVATIONS IN EUV AND NANOIMPRINT LITHOGRAPHY

by

Yunfei Deng

Memorandum No. UCB/ERL M05/27

1 June 2005

ELECTRONICS RESEARCH LABORATORY

College of Engineering
University of California, Berkeley
94720

Modeling Innovations in EUV and Nanoimprint Lithography

by

Yunfei Deng

B.S. (University of Science and Tecnhology of China) 1998
M.A. (University of California, Berkeley) 2000

A dissertation submitted in partial satisfaction of the
requirements for the degree of

Doctor of Philosophy

in

Engineering - Electrical Engineering and Computer Sciences

in the

GRADUATE DIVISION

of the

UNIVERSITY OF CALIFORNIA, BERKELEY

Committee in charge:

Professor Andrew R. Neureuther, Chair
Professor David Attwood
Professor Ming Gu

Spring 2005

The dissertation of Yunfei Deng is approved:

Chair Date

Date

Date

University of California, Berkeley

Spring 2005

Modeling Innovations in EUV and Nanoimprint Lithography

Copyright © 2005

by

Yunfei Deng

Abstract

Modeling Innovations in EUV and Nanoimprint Lithography

by

Yunfei Deng

Doctor of Philosophy in Engineering-Electrical Engineering and Computer Sciences

University of California at Berkeley

Professor Andrew R. Neureuther, Chair

This thesis investigates the application and use of electromagnetic simulation and modeling to a broad range of emerging lithography techniques. The scope of the work includes the extensions of the Finite-Difference Time-Domain algorithm as well as the creation of auxiliary programs for the construction of the input and application specific analysis of the near field output. The dissertation also gives in-depth characterization studies of applications to defect printability and mask performance in EUV lithography, nanoimprint alignment and inspection, and the design of optoelectronic mirrors.

A geometry to refractive index converter, SAM2TEM was developed to link TEMPEST with 3D topography simulation in SAMPLE-3D, and thus extend the capability of electromagnetic simulation to a large range of applications involving modeling topographic changes during process. An average material properties technique was developed to provide subcell resolution description of the geometry. This improved accuracy without memory and runtime penalty enables electromagnetic simulation on large 3D EUV multilayer structures on a network of workstations.

Simulation of the printability for EUV Gaussian defects shows that analytical models are limited by the coherent illumination assumption when defects are large, while its single surface approximation limits the model's validity for small but relatively high defects. Exploration of using d-spacing modified or patterned multilayer directly as photomask in EUV Lithography shows the feasibility of this approach. Lithography imaging performance studies show that the etched and refilled multilayer masks have better image quality in H-V bias, IPE, smaller CD variations, and larger depth of focus than the EUV multilayer masks with absorber stacks.

Electromagnetic simulation was also used to explore the novel Step and Flash Imprint Lithography process with clear-opaque binary molds. This study assesses the material choices and provides design data for the exposure and differential alignment process. The study of complementary inspection shows a cross polarization of up to 15% of incident UV radiation. It is shown that the inspection signal can be improved with the use of shorter wavelength, higher material contrast and immersion liquid.

Electromagnetic simulation was also successfully applied to optoelectronic mirrors and yielded a design of novel sub-wavelength gratings which has a very broad reflection spectrum and very high reflectivity.

Professor Andrew R. Neureuther

Committee Chairman

To my parents

Acknowledgements

First of all, I would like to express my sincerest thanks to my advisor, Professor Andrew R. Neureuther for his inspiration, encouragement, kindness and invaluable guidance. I enjoyed very much being able to work under him throughout my graduate study. He always provides great advices with his knowledge, intuitive thinking and free-spirited ideas. He not only guides me with patience in the research, but also in other areas. He spent hours teaching me how to write a good presentation and give an excellent talk, and always encourage me to improve my English and give advices on future career. I would also like to thank Professor David Attwood, Professor Jeffrey Bokor and Professor Ming Gu for their severing in my qualifying exam committee, their suggestions in research and their excellent courses.

During my graduate years I had the opportunity to work as a summer intern at Advanced Micro Devices. Special thanks to Bruno La Fontaine, Harry J. Levinson, Jongwook Kye and other members of Strategic Lithography Technology group for their support and the great time enjoyed together. I would also like to thank other collaborators throughout my graduate study: Eric Gullikson from Lawrence Berkeley National Lab, Paul. B. Mirkarimi and Anton Barty of Lawrence Livermore National Lab, Don White and Obert Wood at the time from Agere System.

Many thanks are also directed to fellow colleagues in the research group for all their help. It has been so wonderful to study and work with them: Kostas Adam, Junwei Bao, Dan Ceperley, Yijian Chen, Mosong Cheng, Ebo Croffie, Frank Gennari, Scott

Hafeman, Michael Lam, Yanwei Liu, Greg McIntyre, Tom Pistor, Garth Robins, Yashesh Shroff, Michael Shumway, Mike Williamson, Bo Wu, Lei Yuan, and many other friends for enriching my graduate school experience.

Last but not least, I also wish to take this chance to express my deep appreciation to my family. Without their love, support, and care, this work would never have been possible. Thanks, mom and dad, brother and sisters!

This research was funded by the Lithography Network with SRC Contract 96-LC-460/01-MC-460 and DARPA Grant MDA972-97-1-0010/MDA972-01-1-002, and the Millennium Project with NSF Grant EIA-9802069.

Table of contents

1 Introduction 1

1.1 Background 1

1.2 Electromagnetic simulation and modeling 3

1.3 Applications of electromagnetic simulation 5

1.3.1 Applications in EUV Lithography 6

1.3.2 Applications in Nanoimprint Lithography 7

1.3.3 Applications in Opto-electronics and other areas 9

1.4 Thesis content layout 10

1.5 References 13

2 Methods of electromagnetic simulation and modeling 17

2.1 Introduction 17

2.2 SAM2TEM interface between SAMPLE-3D and TEMPEST 20

2.3 Average Material Properties Technique 24

2.4 Parallel simulation with TEMPEST 29

2.5 Conclusions 34

2.6 References 36

3 Modeling EUV Multilayer Structures 38

3.1 Introduction 38

3.2 EUV Multilayer substrate defect structures 40

3.2.1 Structure of substrate defect in EUV multilayer 40

3.2.2 EUV multilayer substrate defect printability: analytical model 42

3.2.3 EUV multilayer substrate defect printability: simulation results 45

3.2.4 Effect of multilayer roughness on defect printability 52

3.2.5 Substrate defect printability after E-beam repair 57

3.3 EUV multilayer mask patterning structures 60

3.3.1 Multilayer mask with absorber stack 62
3.3.2 Etched multilayer mask 64
3.3.3 Refilled multilayer mask 67
3.3.4 Ion-mixed multilayer mask 71
3.3.5 E-beam heated multilayer mask 72
3.4 Conclusions 75
3.5 References 77
4 Modeling Effects of EUV Masks on Lithographic Performance 81
4.1 Introduction 81
4.2 EUV multilayer mask imaging performance 82
4.2.1 CD variation with mask stack thickness variation 84
4.2.2 Effects of sidewall profile in mask imaging 86
4.2.3 Image placement error (IPE) and H-V bias 87
4.2.4 Process window and depth of focus 90
4.2.5 Experimental results 93
4.3 Effects of defects in multilayer mask on imaging performance 94
4.3.1 Effects of multilayer substrate defects 94
4.3.2 Patterning defects and repair in refilled multilayer masks 96
4.4 Discussion and conclusions 99
4.5 References 101
5 Nanoimprint Lithography with clear-opaque mold 105
5.1 Introduction 105
5.2 Clear-opaque mold in Nanoimprint Lithography 106
5.3 Modeling exposure process 108
5.3.1 Effects of feature topography 110
5.3.2 Effects of mold material properties 114
5.3.3 Effects of gap size between the mold and the substrate 116
5.4 Modeling alignment process 118
5.4.1 Alignment marks on transparent molds 118
5.4.2 Alignment marks on clear-opaque molds during printing 121
5.4.3 Alignment marks on clear-opaque molds during inspection 122

5.5 Conclusions 123

5.6 References 125

6 Complementary inspection for Nanoimprint Lithography 128

6.1 Introduction 128

6.2 Complementary inspection of clear-opaque mold 130

6.2.1 Signals from gate test structure 132

6.2.2 Signal enhancement via filtering 134

6.2.3 Effects of system errors on signal 136

6.3 Scattering from small defects 138

6.3.1 Effects of defect size on scattering 139

6.3.2 Effects of material contrast and immersion 141

6.3.3 Effects of incident angle 141

6.3.4 Effects of wavelength scaling with immersion on total scattered light 141

6.4 Conclusions 144

6.5 References 145

7 Applications in Opto-electronics 147

7.1 Introduction 147

7.2 1D sub-wavelength gratings 148

7.3 2D sub-wavelength gratings 151

7.4 Conclusions 153

7.5 References 154

8 Conclusions 156

8.1 Summary 156

8.2 Future work 160

List of Figures

Chapter 1

Figure 1-1. Simplified schematics of optical lithography system 4

Chapter 2

Figure 2-1: Process overview of simulation flow with EUV multilayer Gaussian defect printability study as the example 18

Figure 2-2: Conversion from SAMPLE-3D surface geometry to TEMPEST volume geometry... 22

Figure 2-3: Example of SAM2TEM run 22

Figure 2-4: Effective permittivity for the averaged material computed as the volume average of individual material's permittivity 25

Figure 2-5: Geometry of low-profile Gaussian defect under different number of materials used. 26

Figure 2-6: Reflected E-field from the Gaussian defect converges with more material indexes (M) used 27

Figure 2-7: Reflection from a sinusoid air/dielectric interface for three simulation cases 28

Figure 2-8: Benchmarks of parallel TEMPEST running on the Millennium Cluster:. 31

Figure 2-9: An example of pattern and probe based aberration monitors. 33

Chapter 3

Figure 3 1: The system diagram of EUV Engineering Test 39

Figure 3-2: Geometry of multialyer substrate defect: 40

Figure 3-3: Aerial images of 2D Gaussian defect under two different coherence factors. 46

Figure 3-4: Aerial image minimum of top-hat defect at NA=0.25 47

Figure 3-5: Aerial image minimum of top-hat defect at NA=0.1 47

Figure 3-6: Comparison of Imin for Gaussian defects between rigorous simulation and analytical model 49

Figure 3-7: Imin for the worst-sized defect as a function of defect height 50

Figure 3-8: Diffracted order powers for 3D Gaussian defects 51

Figure 3-9: Topography of multilayer structures with Model X 54

Figure 3-10: Aerial image minimum for Gaussian defects of different defect sizes with various types of roughness 56

Figure 3-11: (a) sketch of e-beam repair of phase defects (b) geometry of phase defect after repair 58

Figure 3-12: (a) Near field phase and (b) aerial images of phase defects after several amounts of e-beam treatment 60

Figure 3-13: The 3D geometry of EUV mask 61

Figure 3-14: The binary mask with absorber stacks on the top of planar multilayer 63

Figure 3-15: The etched binary multilayer mask 64

Figure 3-16: The etched phase shift multilayer mask 65

Figure 3-17: The linear relationship between the phase shift and the etched depth 66

Figure 3-18: The etched multilayer structures 68

Figure 3-19: Variations in the structures and functionalities of refilled multilayer masks 68

Figure 3-20: (a) CD obtained for different etched and refilled depth when they are equal (b) CD obtained for different refilled thickness when the multilayer is etched 210 nm deep .. 69

Figure 3-21: The refilled multilayer binary mask 70

Figure 3-22: Ion-mixed multilayer mask: (a) geometry (b) near field intensity 71

Figure 3-23: (a) The sketch of phase well created by e-beam treatment and (b) the geometry of example attPSM in multilayer 73

Figure 3-24: (a) Near field amplitude and (b) phase reflected from the 20 bi-layer Mo/Si multilayer 74

Figure 3-25: (a) Near field phase and (b) aerial images of attPSM structures 74

Chapter 4

Figure 4-1: The line width variation of 45 nm line space features 85

Figure 4-2: (a) Near fields for three types of masks with negative and positive sidewall angles (b) Measured CD dependence on sidewall angle of METAL1 masks 87

Figure 4-3: The image placement error variations 88

Figure 4-4: The combined process window for the set of features 91

Figure 4-5: The respective process window for three mask structures 92

Figure 4-6: SEM images of mask used and ETS prints 93

Figure 4-7: The 3D Gaussian buried substrate defect centered on the Cr edge 94

Figure 4-8: The 2D aerial image contour at 0.3 threshold for multiple defect locations 95

Figure 4-9: (a) Void defect in the multilayer stack (b) dependence of measured CD on the refilling depth after repaired with different materials 96

Figure 4-10: Effects of repair with different materials 97

Chapter 5

Figure 5-1: The sketch of step-and-flash imprint lithography 106

Figure 5-2: The electrical field intensity in the structure of small dimension holes 109

Figure 5-3: Field intensities plotted at the center of the feature 110

Figure 5-4: The dependence of average light intensities upon the feature size under both TE and TM polarizations 111

Figure 5-5: Light intensity for an over-etched and refilled structure 112

Figure 5-6: Light intensity for a variable thickness Cr layer 113

Figure 5-7: The example clear opaque mold with the semi-opaque layer of n=0.2 and k=1.33: (a) geometry with the semi-opaque layer thickness of 50nm (b) light intensity 115

Figure 5-8: The average light intensity at various positions in the 3D hole simulated for opaque materials with n=3 and k from 1.33 to 6.69 116

Figure 5-9: The example clear opaque mold with the semi-opaque layer of n=0.306 and k=3.19 117

Figure 5-10: Effects of gap size 117

Figure 5-11: Simulation results on alignment marks: 119

Figure 5-12: Alignment mark with an asymmetrical trench bottom 120

Figure 5-13: Alignments marks on both mold and substrate during printing 121

Figure 5-14: Diffracted orders in complementary mold inspection 123

Chapter 6

Figure 6-1: A schematic diagram of complementary mold inspection system 129

Figure 6-2: The geometry of the L-shaped test structure with defects placed in various positions for inspection 131

Figure 6-3: The transmitted light intensities in the bottom mold from the test structure without defects 132

Figure 6-4: The transmitted light intensities in the bottom mold from the test structure with defect 1 133

Figure 6-5: The sketch of complementary inspection scheme for clear opaque nanoimprint mold and the sketch diagrams for ten angular filters 135

Figure 6-6: The same-polarization light signals from defects at four positions normalized to the signal without defects under ten different filters 135

Figure 6-7: The cross-polarization light signals from defects at four positions normalized to the signal without defects under ten different filters 136

Figure 6-8: (a) Dependence of total light after filtering on alignment position (b) Dependence of total light after filtering on separation gap size 137

Figure 6-9: The geometries of the small rectangle defects 138

Figure 6-10: Effects of defect size 140

Figure 6-11: Effects of material contrast and immersion 140

Figure 6-12: Effects of off-axis incident angle 142

Figure 6-13: The total scattered light of same and cross polarizations for unsupported post defects in air compared with in water 143

Figure 6-14: The total scattered light of the same and cross polarizations for supported post and void defects in air compared with in water 143

Chapter 7

Figure 7-1: Scheme of the 1D sub-wavelength grating reflector 148

Figure 7-2: Reflected power for light polarized perpendicularly to the grating lines 149

Figure 7-3: Scheme of the 2D sub-wavelength grating reflector 151

Figure 7-4: TEMPEST simulation results on 2D gratings under both polarizations 152

Figure 7-5: TEMPEST simulation results on 1D gratings under both polarizations 152

List of Tables

Chapter 1

Table 1-1: Applications of electromagnetic simulation and modeling 5

Chapter 4

Table 4-1: The properties of three absorber stacks 83

Table 4-2: Refractive indices of all materials at EUV wavelength (13.4 nm). 84

Table 4-3: The imaging properties for different EUV mask stacks 88

1 Introduction

1.1 Background

Lithography [1-3] refers to the printing process in which patterns of integrated circuits are transferred from a template onto wafers in semiconductor processing. Optical projection lithography, also called photolithography, uses optical methods to transfer the circuit patterns. The ability of optical lithography systems to reproduce an entire integrated circuit (IC) layout in a single exposure provides tremendous throughput advantages over other technologies addressing field point by point. It can also share the resources for infrastructure development with other optical and photographic applications. Thus the overall cost advantages has made optical lithography the manufacturing of choice in the modern IC era.

There are several steps in the lithography process. First the wafer surface is treated to ensure proper adhesion prior to resist coating. After the resist coating is applied, a soft-bake is used to solidify the resist film for later processing. The alignment is performed to ensure the proper overlay of the new layer to the circuit patterns already on the wafer. Then resist materials are exposed to light selectively in some areas and not others by imaging of patterned masks. These photomasks are sheets of glass covered partial by an opaque material according to the patterns of circuits. The projection of transmitted images

from masks creates the circuit patterns in the resist film. An optional bake can be used to drive additional chemical reactions or diffusion in the resist film. Finally the resist is removed depending upon it has been exposure or not. Additional hardbake step may be performed to prepare for the next semiconductor processing steps, such as etch or ion implantation. During these steps, measurements and inspections are often used to check the line widths of resist features, overlay between layers, and defects in the processing for the purpose of process control.

Optical lithography has been the key enabling technology for the miniaturization of integrated circuits. The economics with this continuing reduction of lithography resolution leads to the spectacular exponential growth of semiconductor industry, as predicted as Moore's law [4]. After almost forty years, the end of this extraordinary growth has yet to happen. However, optical lithography has been pushed near to its practical limit of resolution with several extensions by reducing the wavelength λ of the optical source to deep ultraviolet (DUV) 193 nm light, increasing the numerical aperture (NA) of the optical system up to 0.85 now or as far as 0.95, and reducing k_1 down to 0.3 via many resolution enhancement techniques [5-7]. As the ultimate lithographic resolution can be characterized by the critical dimension (CD) as a function of above three parameters,

$$CD = k_1 \frac{\lambda}{NA}$$

All three measures to improve resolution have been exploited and there is no much room to extend further (NA ≤ 1.0, $k_1 \geq 0.25$). The introduction of immersion lithography, which gives a larger effective NA ($n_{liquid} \sin(\theta)$) at an enhanced depth of focus (DOF), may ex-

tend optical lithography for another generation or two, but the transition to non-optical lithography is inevitable in the near future.

Numerous next generation lithography (NGL) methods have been proposed to replace optical lithography as shown in the International Technology Roadmap for Semiconductors (ITRS) [8]. This list included proximity X-ray lithography (PXL), proximity electron lithography (PEL), ion projection lithography (IPL), electron projection lithography (EPL), maskless lithography (ML2), extreme ultraviolet lithography (EUVL) and innovative technology such as imprint lithography. EUV Lithography [9] won the battle to become the most feasible NGL technique for high volume manufacturing, but it is still pushed further down the roadmap to 32 nm generation because of continuing extension of 193 nm technology. On the other side, imprint lithography poses a disruptive solution with resolution down to 10 nm. Though currently many technology challenges limit it to special applications, imprint lithography may overcome those difficulties and prevail in the applications of large scale integrated circuits.

1.2 Electromagnetic simulation and modeling

In the early days of semiconductor manufacturing, lithography was widely considered as an art. The transformation of lithography from art to science began in the early 1970s with the milestone series of papers from R. Dill *et al.* [10] in optical lithography modeling. After that, many lithography process simulators including SAMPLE [11], DEPICT [12], PROLITH [13], SOLID-C [14] were developed and improved over the time. Now days physical modeling via computer simulation has become a usual practice in modern optical lithography and process development. Simulation not only often is faster

but also cheaper to conduct virtual experiments than doing real experiments given the reduction of computation resources and increasing cost of experiments in the advance integrated circuit fabrication facilities. Simulation also provides the flexibility to decouple physical phenomenon to analyze individual physical process, thus helps to obtain better understanding of advance lithography process and emerging technologies. Simulation can also go beyond the capability of current hardware to investigate issues before lithography tools are ready to use or to explore new technology without building real hardware. This is especially useful in the early stage of lithography technology development.

Simulation is used throughout this thesis to model innovations in lithography applications. Typical lithography simulations involve the modeling of the optical projection system as shown in Figure 1-1. The condenser optics collects the light from source and illuminates the mask (reticle). Then light diffracted from the mask is captured by the objective lens and imaged on to the resist film on the wafer. This lithography imaging simulation is carried out using SPLAT simulator [15]. However, the more essential part of thesis is concentrated on the rigorous electromagnetic simulation of mask diffraction, as physical models better than thin-mask approximation are needed to model aggressive mask patterns in DUV lithography and also new mask structures in next generation li-

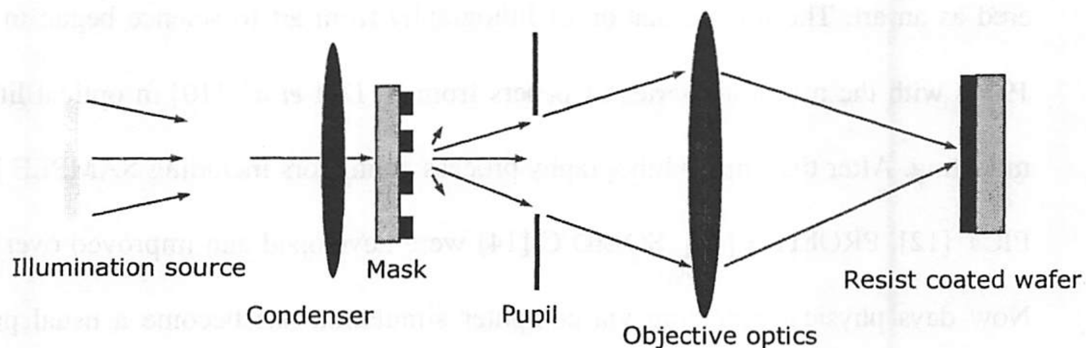

Figure 1-1. Simplified schematics of optical lithography system.

thography techniques. Or complete exposure process needs to be modeled as in Nanoimprint Lithography.

The electromagnetic simulation is carried out with the Finite Different Time Domain (FDTD) [16] Maxwell solver called TEMPEST [17]. Useful extensions, such as the SAM2TEM interface and the average material properties technique, have been made to original program to solve the challenges in modeling electromagnetic process in EUV Lithography and other applications.

1.3 Applications of electromagnetic simulation

Besides many applications in EUV and Nanoimprint Lithography, a wide scope of electromagnetic simulation and modeling applications are also presented in this thesis, including Opto-electronics, laser thermal annealing, and even pupil-plane masks for space telescopes in the Terrestrial Planet Finder (TPF) project as shown in Table 1-1. This di-

Simulation Application	Size (λ^3)	Geometry ganularity (cpw)	Material contrast	Q	Time dependency
DUV masks	normal	normal	normal	low	steady
EUV masks	very large	normal/high	low	low	steady
Nano-imprint	normal	high	normal/high	low	steady or dynamic
Opto-electronics	small	very high	high	high	steady
Laser Thermal annealing	normal	very high	high	low	dynamic
TPF masks	large	normal	normal	low	steady

Table 1-1. Applications of electromagnetic simulation and modeling.

verse set of applications have a wide range of requirements on modeling capability, accuracy and speed for electromagnetic simulation tools, and present a broad range of challenges for the TEMPEST electromagnetic simulation program initially developed for lithography applications. These challenges have stimulated the further development of the simulation methodology, and have provided a large set of use cases to test the performance and usefulness of simulation and modeling.

1.3.1 Applications in EUV Lithography

Extreme ultraviolet (EUV) lithography [18] follows the path of projection optical lithography system but with a radical reduction of wavelength to the 11 – 14 nm region. This shorter wavelength provides a continued path to reduce resolution while keeping modest values of k_1 and NA over several generations with a large depth of focus (DOF). However, at this short wavelength region, most materials absorb EUV radiation, including nitrogen and oxygen, so that the whole system must always be placed in a vacuum, and masks and projection lens can only use mirrors. Together with other primary issues such as source power and EUV resists, the mirrors and masks are major concerns for EUV Lithography to be adopted commercially.

Simulation has been used for a wide range of applications during developing EUV technologies, such as calculating the optical properties of thin films at extreme ultraviolet and soft X-ray wavelengths, computation of reflected images from multilayer masks by S. Bollepalli *et al.* [19] and early TEMPEST simulations by Nguyen *et al.* [20-21] for EUV mask topography effects in two dimensions. T. Pistor continued the study with 3 dimen-

sional simulations of EUV mask features [22] and multilayer mirror defects [23]. He also introduced the Fourier Boundary Condition [22] as an approximation to replace multilayer in the electromagnetic simulations to reduce computation.

In the beginning of this thesis study, the multilayer defects became a critical issue in manufacturing EUV masks as they are hard to detect and repair. The initial project started with modeling these low-profile Gaussian shaped substrate defects in EUV multilayer collaborated with E. Gullikson of Lawrence Berkeley National Lab, P.B. Mirkarimi and A. Barty of Lawrence Livermore National Lab. Later the study was expended to the imaging simulations of non-planar multilayer structures such as the multilayer substrate defects after e-beam repair. These simulations stimulated the collaboration work with B. La Fontaine, H. J. Levinson of Advanced Micro Devices on the etched and refilled EUV multilayer masks as an alternative choice for EUV mask architecture. Electromagnetic simulation was applied to systematically investigate the mask diffraction and imaging performance of such multilayer structures.

1.3.2 Applications in Nanoimprint Lithography

Nanoimprint Lithography is also one of the candidates for next generation lithography techniques. This disruptive technique has gained more momentum with rapid progress in recent years. Imprint lithography was first proposed for semiconductor patterning by S. Chou *et al.* [24]. In 1990s, researchers have systematically studied various imprint lithography techniques, which can be divided into two camps. The first camp of imprint lithography techniques is based on imprinting into a thermaplastic or thermoset polymer

at elevated temperature under high pressure, such as techniques from S. Chou *et al.* [25], H-C., Scheer *et al.* [26], R. W. Jaszewski *et al.* [27], H. Schultz *et al.* [28]. Thermal imprint lithography has demonstrated remarkable resolution with features down to 10 nm and the first functional devices, though overlay can be difficult under such high temperature and high pressure process.

The second group of imprint lithography techniques relies on curing a low viscosity, photosensitive polymer with ultraviolet light. These techniques include Philips photopolymer process [29], microcontact printing [30], micromolding in capillaries [31] and solvent-assisted micromolding [32]. They may be well suited for specific applications but not suited for general sub-100 nm patterning in the high volume semiconductor manufacturing. G. Willson *et al.* [33] proposed the step and flash imprint lithography (SFIL) process which now competes with EUV Lithography and holds the possibility to overtake it, though there are sill major hurdles to be addressed.

All the above imprint lithography techniques have a common theme that the patterning is accomplished via pressing a template or mold with prefabricated topography into a resist material. The resist material conforms to the topography of the master template and then is solidified. Thus this is a contact printing process which transfers patterns without reduction. The important advantage of such imprint techniques is that the resolution no longer depends on optical lenses, but is rather limited by the resolution of structures on the template. However, this also brings the major challenges of imprint lithography process including the 1X template fabrication and defect susceptibility.

To address many of above issues, D. White and O. Wood [34] proposed a variant of SFIL that uses a clear-opaque mold instead of a transparent template. The collaboration

work with them investigated the exposure, alignment, and defect inspection processes in such approach, and provided enormous modeling data and design choices for such complete nanoimprint lithography system for semiconductor manufacturing.

1.3.3 Applications in Opto-electronics and other areas

The electromagnetic scattering simulator, TEMPEST, was first developed for lithography process. However, its finite difference time domain algorithm for solving Maxwell Equations is equally applicable to many other electromagnetic processes, such as the collaboration work with Professor Connie J. Chang-Hasnain's group on broadband mirrors. This led to the design of a novel sub-wavelength grating [35] with very high reflectivity in a very broad reflection spectrum. Such broadband mirrors can have a wide range of applications in Opto-electronics.

TEMPEST was also applied to investigate the complex electromagnetic process in Ultratech's advanced Laser Spike Annealing technology [36], where a high energy laser beam is incident on a thin poly layer on doped silicon substrate. Though this process happens in microseconds to milliseconds timeframe and the substrate doping is dynamically varied with absorbed energy, simulations with simplified treatment of material properties gave correct prediction of interference effects at poly line edges and defect locations where peak light intensity happens or largest dose of energy is abosrbed.

The ability of accurate modeling mask edge scattering also attracted researchers at Ball Aerospace to collaborate on modeling the Coronagraph pupil mask for the Terrestrial

Planet Finder project [37]. The early work on this kind of pupil mask resulted in a research proposal to JPL.

1.4 Thesis content layout

This thesis documents the improvements to TEMPEST and simulation study in many applications. Due to the broad breadth of topics discussed, each chapter will first give a short introduction specific to the subsequent topics. Then the main ideas with descriptions of each simulation structure and result are presented, followed by the final conclusions with summary of important results and observations.

Chapter 2 starts with a more detailed introduction to electromagnetic simulation and modeling. The typical electromagnetic simulation and lithography modeling flow used throughout this thesis study is presented. Then the SAM2TEM interface between SAMPLE-3D and TEMPEST simulators is presented with its application to EUV multilayer deposition. The average material properties technique is introduced and its improvement to accuracy and speed of TEMPEST is discussed. Finally the parallel simulation with TEMPEST is demonstrated and benchmarked on a large scale cluster of workstations.

The combinations of the above enhancements to TEMPEST enabled rigorous electromagnetic simulation and modeling of large EUV non-planar multilayer structures. Starting with defect printability study of Gaussian shaped EUV multilayer substrate defect, Chapter 3 examines various non-planar multilayer mask structures, such as Gaussian shaped substrate defect with features, substrate defects repaired with e-beam heating and d-spacing modified multilayer attenuated phase shift masks via e-beam heating, and in-

novative subtractive multilayer structures including the etched and refilled multilayer EUV masks. EUV light diffraction on these multilayer mask structures are analyzed to show their intrinsic advantages over the traditional EUV masks with absorber stacks.

Chapter 4 continues the discussion of three multilayer mask stacks with concentration on their lithography imaging performance. Their imaging quality are compared in areas of horizontal-vertical (H-V) bias, imaging placement error (IPE) and CD variations. It is also shown that the etched and refilled multilayer masks have larger process window and less affected by the sidewall profile in etching. The processing challenges are pointed out for the etched and refilled multilayer masks to be a practical alternative architecture for EUV masks. A new pattern defect repair scheme for these etched and refilled multilayer masks is proposed and analyzed.

Chapter 5 and 6 cover the application of electromagnetic simulation and modeling to the Step and Flash Imprint Lithography with clear-opaque molds in White and Wood's approach. Chapter 5 starts with the systematical study of the mold exposure process which provides design guidelines for feature geometry and mold material selections. The second part of Chapter 5 discusses the differential alignment scheme for nanoimprint lithography either with transparent molds or with clear-opaque molds. Alignment signals are analyzed in both cases.

Chapter 6 continues the study of nanoimprint lithography on characterization of defect inspection. The new complementary inspection scheme with clear-opaque molds is examined with test structures. It is shown the defect signals from typical defects at 45 nm generations are too small with UV radiation. Several ways to improve inspection signals are discussed, such as the angular filtering of inspection signals, inspecting with a smaller

wavelength radiation. In the second part of the Chapter, the scattering signals from small defects are analyzed for its dependence on defect size, materials contrasts and immersion environment.

The applications of electromagnetic simulation and modeling in other areas outside of lithography are covered in Chapter 7. Here the innovative sub-wavelength grating structures used as broadband mirrors in opto-electronics are also simulated with TEMPEST simulator. The reflection spectrums for both polarizations on one dimensional and two dimensional grating structures are systematically analyzed.

Finally, Chapter 8 concludes the thesis with a summary of the most important results and addresses future research.

1.5 References

[1] H. J. Levinson, *Principles of Lithography*, SPIE Press, 2005.

[2] J. Sheats and B. Smith, eds. *Microlithography: Science and Technology*, Marcel Dekker, 1998.

[3] P. Rai-Choudhury, ed., *Handbook of Microlithogarphy, Micromachining, and Mcirofabracation*, SPIE Press, 1997

[4] G. E. Moore, "Lithography and the Furture of Moore's Law", *Proc. SPIE*, vol 2440, pp.2-17 (1995).

[5] A. Wong, *Resolution Enhancement Techniques in optical lithography,* SPIE Press, 2001.

[6] F. M. Schellenberg, ed., *Selected Papers on Resolution Enhancement Techniques in Optical Lithography,* SPIE Press, 2001.

[7] A. Wong, *Optical Imaging in Microlithography,* SPIE Press, 2005.

[8] International Technology Roadmap for Semiconductors, http://public.itrs.net/

[9] D. Attwood, *Soft X-rays and Extreme Ultraviolet Radiation: Principles and Applications*, Cambridge University Press, 1999.

[10] F. H. Dill, A. R. Neureuther, J.A. Tuttle, and E. J. Walker, "Modeling Projection Printing of Positive Photoresists", *IEEE Trans. Electron Devices*, ED-22, No 7, pp. 456-464, 1975.

[11] W. G. Oldham, S.N. Nandgaonkar, A. R. Neureuther, and M. M. O'Toole, "A General Simulator for VLSI Lithography and Etching Process: Part I – Applications to Projection Lithography", *IEEE Trans. Electron Devices*, ED-26, No 4, pp. 717-722, 1979.

[12] Technology Modeling Associates, DEPECT-2, Technology Modeling Associates, 1990.

[13] C. A. Mack, "PROLITH: A Comprehensive Optical Lithography Model", *Proc SPIE*, vol 538, pp. 207-220 (1985).

[14] SIGMA-C GmbH, Solid-C, http://www.sigma-c.com

[15] SPLAT User's Guide ver 6.0, University of California at Berkeley, http://cuervo.eecs.berkeley.edu/Volcano/docs/splat/misc/contents.html.

[16] A. Taflove, *Computational Electrodynamics The Finite-Difference Time-Domain Method,* Artech House, Norwood, MA, 1995.

[17] T. Pistor, "Electromagnetic Simulation and Modeling with Applications in Lithography", Ph.D. Dissertation, University of California at Berkeley, 2001.

[18] G. D. Kubiak and D. R. Kania, eds, *Extreme Ultraviolet Lithography*, OSA Trends in Optics and Photonics, Vol. 4 (Optical Society of America, Washington, DC 1996).

[19] S. B. Bollepalli, F. Cerrina, "Computation of reflected images from extreme ultraviolet masks", *Proc. SPIE,* vol. 3676, pp. 587-597 (1999).

[20] K. B. Nguyen *et a.l*, "Printability of substrate and absorber defects on extreme ultraviolet lithographic masks", *J. Vac. Sci. Technol*, B 13(6), pp.3082-2088, Nov/Dec 1995.

[21] K. B. Nguyen, A. K. Wong, A. R. Neureuther, D. T. Attwood, T. D. Nguyen, "Aerial Images of EUV Projection Lithography Masks with Defects in Reflective Coatings: Electromagnetic Simulation", *OSA Proceedings on Soft X-Ray Projection Lithography*, vol 18, pp. 47-53, 1993.

[22] T. Pistor *et al.*, "Rigorous simulation of mask corner effects in extreme ultraviolet lithography", *J. Vac. Sci. Technol*, B 16(6), pp.3449-3455, Nov/Dec 1998.

[23] T. Pistor *et a.l*, "Extreme ultraviolet defect simulation", *J. Vac. Sci. Technol*, B 17(6), pp.3019-3023, Nov/Dec 1999.

[24] Chou, S. Y., Keimel, C. and Gu, J. *Nature, 417*, pp. 835 – 837, 2002.

[25] Chou, S. Y., P. R. Krauss, P. R. Renstrom, "Nanoimprint Lithography", *J. Vac. Sci. Technol.* B, 14(6), pp. 4129-4133 (1996).

[26] H-C. Scheer, H. Schults, F. Gottschalch, T. Hoffmann, C. M. Sotomayor Torres, "Prolems of the Nanoimprint Technique for nm-scale Pattern Definition", *J. Vac. Sci. Technol.* B, 16(6), pp. 3917-3921 (1996).

[27] R. W. Jaszewski, H. Schift, J. Gobrecht, P.; Smith, *Microelectronics Engineering*, 41/42, pp. 575-578 (1998).

[28] H. Schults, H-C. Scheer, T. Hoffmann, C. M. Sotomayor Torres, K. Pfeiffer, G. Bleidiessel, G. Grutzner, Ch. Cardinaud, F. Gaboriau, M.-C. Peignon, J. Ahopelto, and B. Heidari, *J. Vac. Sci. Technol.* B, 18(4), 1861 (2000).

[29] J. Haisma, M. Verheijenm, K. van der Huevel, J van den Berg, "Template-assisted nanolithography: A process for reliable pattern replication", *J. Vac. Sci. Technol.* B, 14(6), pp. 4124-4129 (1996).

[30] A. Kumar, G. M. Whitesides, Appl. Physics Lett, 63, pp.2002-2004 (1993).

[31] E. Kim, Y. Xia, G. M. Whitesides, *Adv. Mater.* 376, pp. 581-584 (1995).

[32] E. Kim, Y. Xia, G. M. Whitesides, *Adv. Mater.* 9, pp. 651-654 (1997).

[33] M. Colburn, S. Johnson, M. Stewart, S. Damle, T. Bailey, B. Choi, M. Wedlake, T. Michaelson, S.V. Sreenivasan, J.G. Ekerdt and C.G. Willson. "Step and Flash Imprint Lithography: A new approach to high resolution patterning." *Proc. SPIE,* vol 3676, p. 379 (1999).

[34] D. L. White, O. R. Wood II, *A complete system of nano-imprint lithography for IC production*, *Proc. SPIE,* vol 4688, pp. 214-222 (2002).

[35] C. F. R. Mateus, M. C. Y. Huang, Y. Deng, A. R. Neureuther, C. J. Chang-Hasnain, "Ultra Broadband Mirror Using Low-Index Cladded Sub-Wavelength Grating", *IEEE Photonics Technology Letters*, vol. 16, no. 2, Feb 2004.

[36] Ultratech, http://www.ultratech.com/products/laser_family.shtml

[37] Terrestrial Planet Finder, JPL, http://planetquest.jpl.nasa.gov/TPF/tpf_index.html

2 Methods of electromagnetic simulation and modeling

2.1 Introduction

Simulation and modeling play a key role in developing new photolithography technologies. With the improvement of computation capability and better physical models built into today's simulators, they are now not only used as tools which just augment or aid the process development, but they are also used to provide quantitative design data to enable innovation in many emerging technologies. Via simulation and modeling of the complicated physical phenomena in emerging lithography and inspection processes, more physical insight and innovative solutions can be explored for challenging technical issues.

Electromagnetic simulation refers to the computation of electromagnetic fields propagated through various objects. These objects usually are, but are not limited to, photomasks in the lithography applications. The problem of electromagnetic field propagation or scattering is common to many other fields and advances in simulation approaches are applicable there as well as vice versa.

In the lithography applications, the electromagnetic simulation is often the essential step of modeling complicated processes. But usually lithographers care most about the end result of the whole process, such as the final images obtained at wafer. Thus additional simulation modules are needed to provide lithographers a complete solution. Such suite of simulation tools usually consists of an optical simulator for modeling the optics,

an electromagnetic simulator for modeling the light diffraction at photomasks, a resist simulator for modeling resist exposure, bake and development processes, and sometimes a topography simulator which models the topography profile changes during the semiconductor processing such as etching and deposition. The SAMPLE TCAD group at University of California at Berkeley has developed such package of simulations tools including the integrated tool SAMPLE-3D [1], and individual simulators such as TEMPEST (EM) [2-4], SPLAT (aerial imaging) [5-6], and STORM (resist) [7].

The electromagnetic simulation and modeling applied this thesis study includes the mask topography simulation with SAMPLE-3D, the mask diffraction modeling with TEMPEST, and the aerial image simulation with SPLAT. Resist modeling is not included

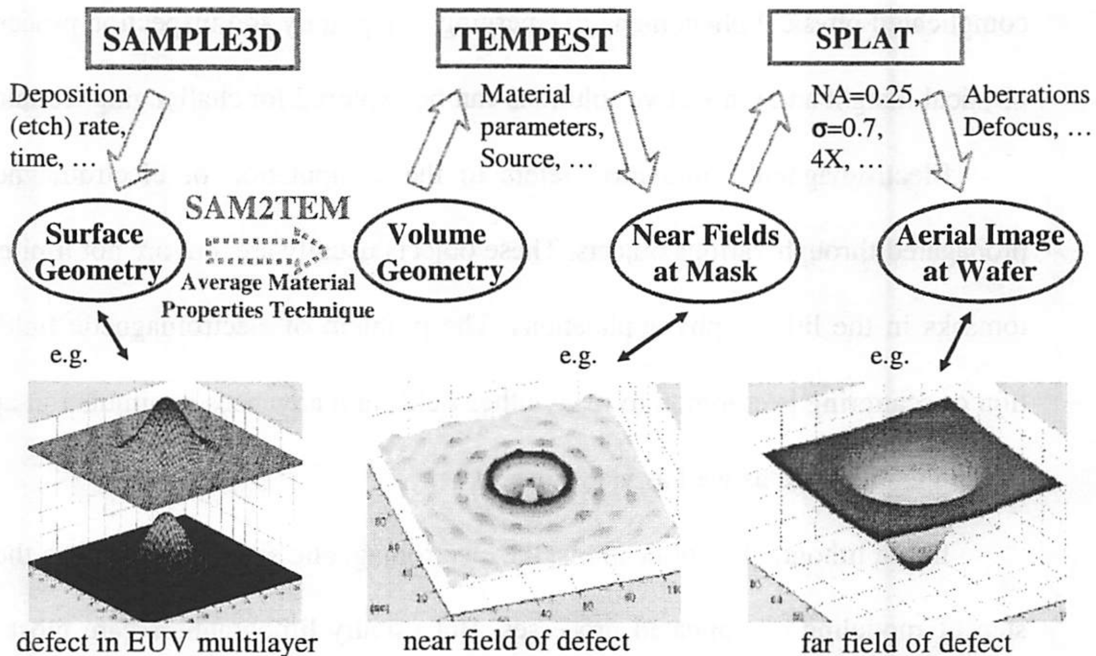

Figure 2-1. Process overview of simulation flow with EUV multilayer Gaussian defect printability study as the example.

as resist images are not considered in this study.

Figure 2-1 shows the simplified flow of the usual electromagnetic simulation and modeling process using the study of EUV multilayer substrate with a Gaussian shaped substrate defect as the example.

The simulation flow begins with running SMAPLE-3D with processing parameters such as etching and deposition rates and time of their duration. The simulation result is the topography formed on the mask that is described by a series of surfaces, such as bi-layers of the EUV multilayer structure with a 3D Gaussian shape defect in this example. Then these surface geometry descriptions are converted to a volumetric description of the refractive index using SAM2TEM interface. TEMPEST reads in this volume description of the materials that reside on every node inside the simulation domain. With other input parameters such as a table of the refractive index of each material and source excitations, TEMPEST then solves the Maxwell equations and outputs the steady-state electrical fields reflected from the 3D structure. Figure 2-1 shows an example of the near field intensity reflected from the multilayer with the Gaussian defect. Then SPLAT is used to simulate the aerial images in the far field at the wafer plane under desired optical conditions such as the numerical aperture NA, coherence factor σ, demagnification factor M, and amount of defocus or aberrations. The example of aerial image from the multilayer with the Gaussian defect shown above has a dip caused by the presence of the defect.

These near fields and aerial images are usually analyzed further, qualitatively for more physical insight and understanding of process effects and quantitatively to systematically characterize the dependence on input parameters. The results can then be compared with experimental results or simulation can be continued with another iteration of the structure or imaging conditions under study. All of the steps mentioned above form

the typical work flow for the electromagnetic simulation and modeling. With the fast progress of computer hardware and software and with reasonable computation power, most of above simulations can performed within a reasonable time frame, such as minutes or hours. However, the electromagnetic scattering simulation with TEMPEST is still often the 'bottleneck' for 3D structures with large domain sizes. For this reason parallel computation is exploited in TEMPEST and applied frequently throughout this study.

In following sections, a more detailed discussion is presented on SAM2TEM [8], which links the existing topography simulator in SAMPLE-3D and the electromagnetic simulator TEMPEST. The FDTD algorithm involved is shown and its application on the deposition of EUV multilayer is presented. Additionally the average material properties technique implemented in SAM2TEM is discussed. The last part of chapter discusses parallel simulations with TEMPEST and benchmark statistics from use cases.

2.2 SAM2TEM interface between SAMPLE-3D and TEMPEST

Previously there was a missing link between the existing topography simulator in SAMPLE-3D, and the electromagnetic simulator TEMPEST, because SAMPLE3D outputs surface description of topography, while TEMPEST requires a volume description of material properties. Now they can be linked with the new interface called SAM2TEM.

SAMPLE-3D is an integrated package of lithography process simulators. The part which does topography simulations is called NETCH [9]. NETCH uses a surface advancing algorithm and generates series of surfaces which defines material boundaries. Each surface is described by a list of triangles which form a mesh on the entire surface.

From this series of surfaces outputted by NETCH, SAM2TEM first generates a three dimensional regular array of nodes which fills the entire simulation domain and then assigns material information to each node based on the material associated with the region between the adjacent 3D surfaces (in this case, whether the material is silicon or molybdenum). While there exists a well-established test to determine the position of a point relative to the individual triangles of a surface [10-11], that technique does not scale well for relating a point with a multi-triangle surface. For one thing, the process would require the testing of each node in the domain with all triangles of several nearby layers. In a full three-dimensional simulation, this may easily run into the millions of nodes and tens of thousands of triangles. Matters would further be complicated by the nature of the surfaces because the triangles may be oriented over a wide range of solid angles, a node may be falsely interpreted as being 'above' a triangle while it lies below that triangle's surface. Thus, additional steps would need to be taken to properly interpret the triangles' orientations as they relate to the surfaces.

The new program SAM2TEM generates a 2-D or 3-D index of refraction matrix readable by TEMPEST in the following manner. Given domain boundaries and desired node density, SAM2TEM creates a grid in the X-Y plane. Then it reads in series of surfaces outputted from NETCH. Each SAMPLE triangle in these surfaces is then superimposed on the grid, temporarily ignoring the vertical dimension. X-Y coordinates in the vicinity of each triangle are examined to determine whether or not they lie within the triangle. If they do, then the program finds the position of these points, called surface intersection marker nodes, on their respective triangles in 3-space, making use of the property that every triangle defines a plane. Applying that process to every triangle in the SAM-

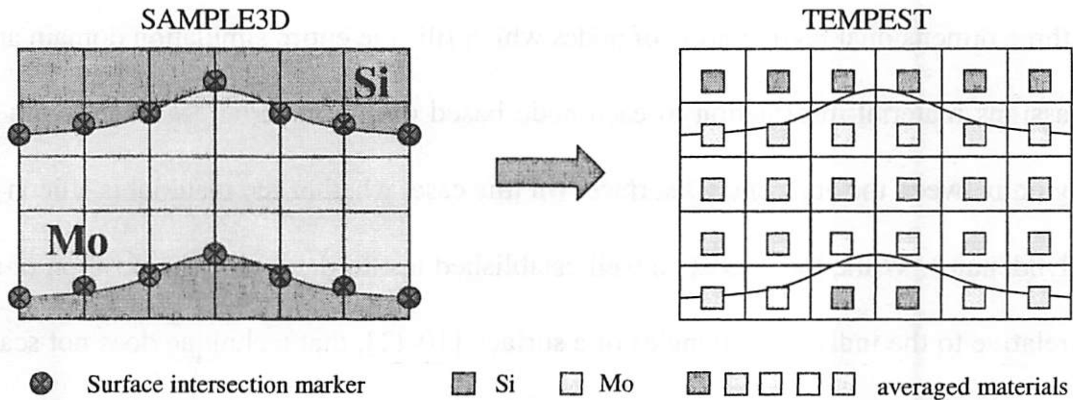

Figure 2-2. Conversion from SAMPLE-3D surface geometry to TEMPEST volume geometry.

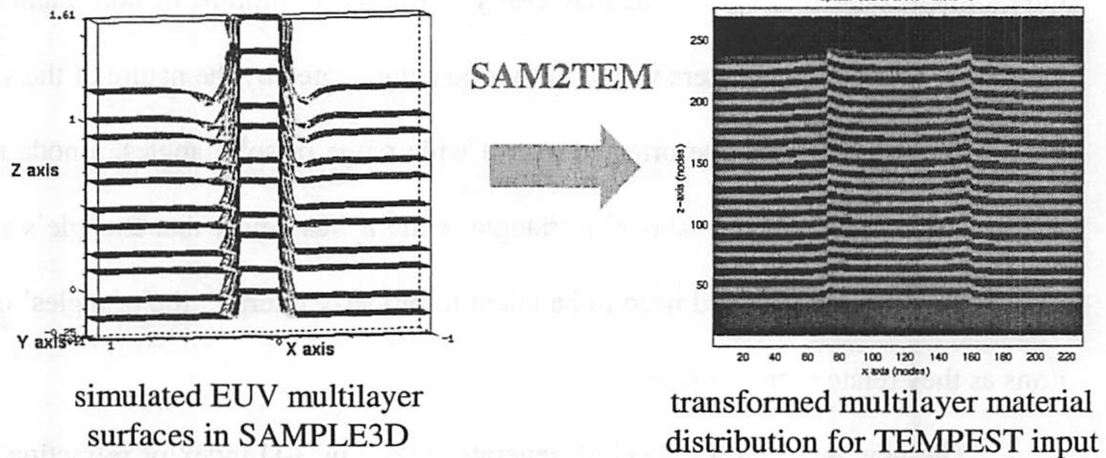

Figure 2-3. Example of SAM2TEM run: (a) EUV multilayer surfaces generated in SAMPLE-3D (b) converted volume geometry inputed to TEMPEST.

PLE surface set has the effect of defining each surface as a set of marker nodes uniformly spaced in X-Y space. The program then has the task of completing the 3-dimensional matrix. This is accomplished by tracing along a auxiliary vertical ray from each node in the z = 0 plane and labeling the material type at nodes between surfaces (which are now defined by the marker nodes), changing the material index every time the vertical ray crosses a surface, In this three-material case, this process creates a 3-D matrix consisting

of the index values for all materials. The program also generates the TEMPEST instruction file that defines the simulation parameters and maps the index values of materials in the matrix to the indices of refraction for vacuum and whatever materials are used in the domain. Figure 2-2 shows the sketch of the surface intersection marker nodes on Si/Mo/Si surfaces in EUV multilayer. Figure 2-3 (a) shows the series of surfaces obtained from NETCH. Figure 2-3 (b) plots the material index in the domain after SAM2TEM conversion.

It is noticed that when the node size is larger than the smallest distances between two neighboring surfaces, there are some volume elements intersected by multiple surfaces. Which material the volume element is located in is not clearly defined. These nodes rather have a mixture of two or more materials. The other issue that needed to be treated is that for each surface intersection marker node there are also at least two materials existing. The simple decision on which material the node is located in can cause a digitizing error. This issue is more apparent in the case of EUV multilayer with a very low profile Gaussian shaped defect, such as when the height of Gaussian profile is smaller than one node size. This digitizing error can greatly affect the electromagnetic simulation in TEMPEST as the inputted geometry loses its fidelity.

Improvement of the original algorithm was made with the new average material properties technique. This technique basically asks SAM2TEM to maintain all surface intersections in their order along Z direction for each point in the X-Y grid, and then calculate a volume average of material properties for each surface intersection marker node. For the multilayer case, only two materials are involved, so SAM2TEM can set a number to index pure Si and pure Mo or any weighted average of these two materials. If there are

more materials involved, several look-up tables need to be established and combined to index all material properties. Figure 2-2 illustrates the averaged materials existing in the surface intersection nodes.

The SAM2TEM program is sufficiently robust to handle surfaces folding back on upon themselves and contains provisions for all other known singularities. Some speed benchmarks are the following: the 62 surfaces x 120 triangles/surface ideal flat multilayer is created by NETCH in 15 seconds, generating 2.4 million nodes in the full 3-D domain. SAM2TEM takes 8 seconds to produce the 2-D TEMPEST .top file with 43 x 240 nodes, or 10 seconds for the 3-D array with 43 x 43 x 240 nodes. Both examples were performed on a 200 MHz UltraSparc machine.

As discussed, there is nothing in the SAM2TEM process that is specific to EUV multilayer simulations so that the program may be applied to other areas of optical lithography, where the etching or deposition process is of interest, such as in the study of phase defect due to phase trench etching in the Phase-shift masks. With SAM2TEM fills the missing link, NETCH, TEMPEST and SPLAT can be combined to a more complete package for lithography process simulation and modeling.

2.3 Average Material Properties Technique

The average material properties technique introduced in the above section coincides with the Dey-Mittra technique developed independently by Dey and Mittra for modeling cylindrical dielectric ring resonators [12].

This average material properties technique is based on the calculation of an effective local dielectric constant for the electrical fields. Its principle is very simple, but it

treats dielectric structures with curved surfaces very efficiently and improves the accuracy significantly relatively to staircasing.

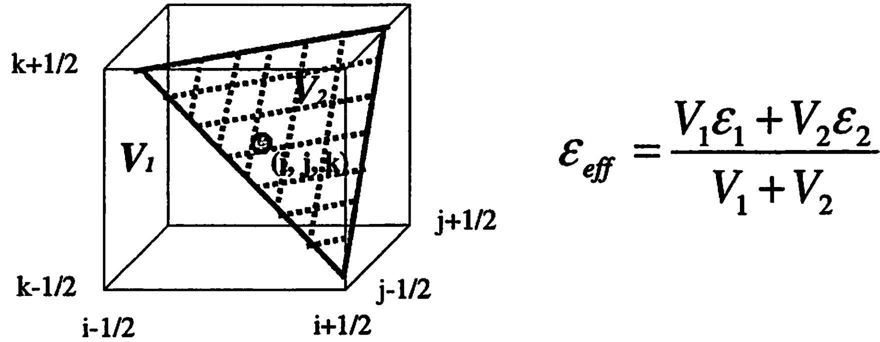

Figure 2-4. Effective permittivity for the averaged material computed as the volume average of individual material's permittivity.

Figure 2-4 illustrates the geometry of a FDTD cell at node (i, j, k) with a surface of dielectric structure cutting in a planar manner through the cell. An effective permittivity is calculated by weighted volume average of the material permittivities on each side of the dielectric interface. This effective permittivity is then assigned to this node and used in the Finite Difference Time Domain (FDTD) update equations [2]. Such as in the update equation for *Ez(n+1)* component, the form of equation is not changed but only two coefficients α and β are changed at this node with ε replaced by ε_{eff}:

$$E_z^{n+1}[i,j,k] = \alpha(E_z^{n}[i,j,k]) + \beta(H_x^{n+1/2}[i,j+1/2,k] - H_x^{n+1/2}[i,j-1/2,k] + H_y^{n+1/2}[i,j+1/2,k] - H_y^{n+1/2}[i,j-1/2,k])$$

$$\alpha = \frac{2\varepsilon - \sigma\Delta t}{2\varepsilon + \sigma\Delta t}, \beta = \frac{\Delta t}{\Delta x}\frac{2}{2\varepsilon + \sigma\Delta t}$$

The improved speed and accuracy by using this average material properties technique can be illustrated by following simulation examples.

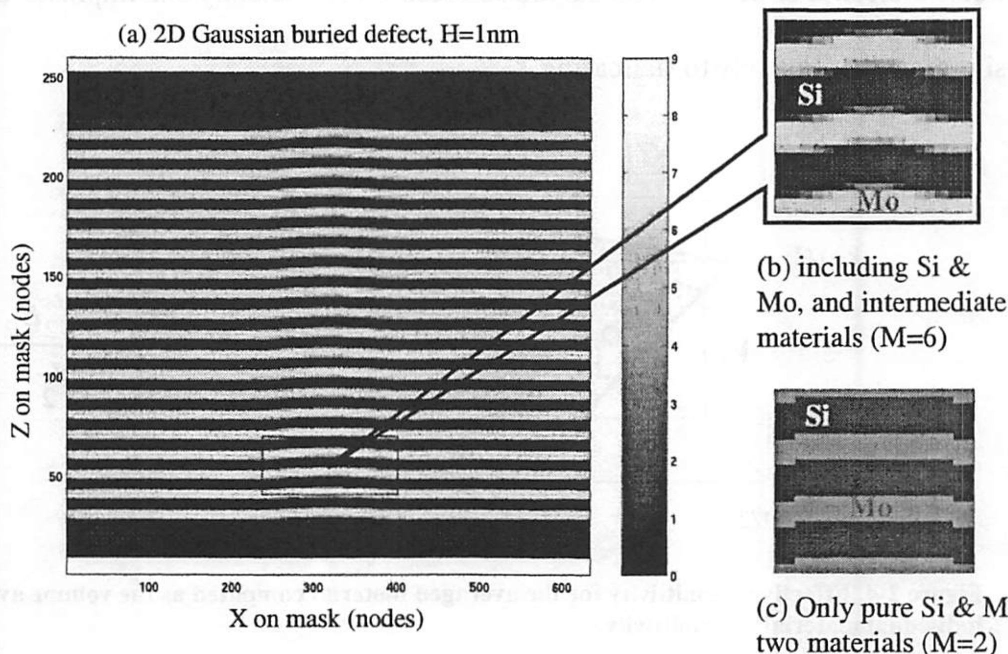

Figure 2-5. Geometry of low-profile Gaussian defect under different number of materials used: (a) full domian when M=6 (b) zoom-in view when M=6 (c) zoom-in view when M=2.

A EUV multilayer stack with Gaussian shaped substrate defect is simulated. The Gaussian shaped defect has a height of only 1 nm, and a sigma width of 28 nm. Figure 2-5 (a) shows the geometry generated using this average material properties technique with the number of materials M = 6. For comparison, the geometry in the staircasing case when M = 2 is also shown in Figure 2-5 (c). As the TEMPEST cell size is 0.7nm, this 1 nm high Gaussian defect shows up as only one step, which clearly indicates that such a discretization cannot be accurate for a 1nm high defect. This presents a problem in modeling these low-profile Gaussian shaped defects by electromagnetic simulation with TEMPEST, as using a smaller cell size is impractical because of the increase of memory usage and run time. However, if using the average material properties technique, as shown in Figure 2-5 (b), effectively a subcell resolution can be obtained without using smaller cell size. Thus the FDTD gridding error is greatly reduced.

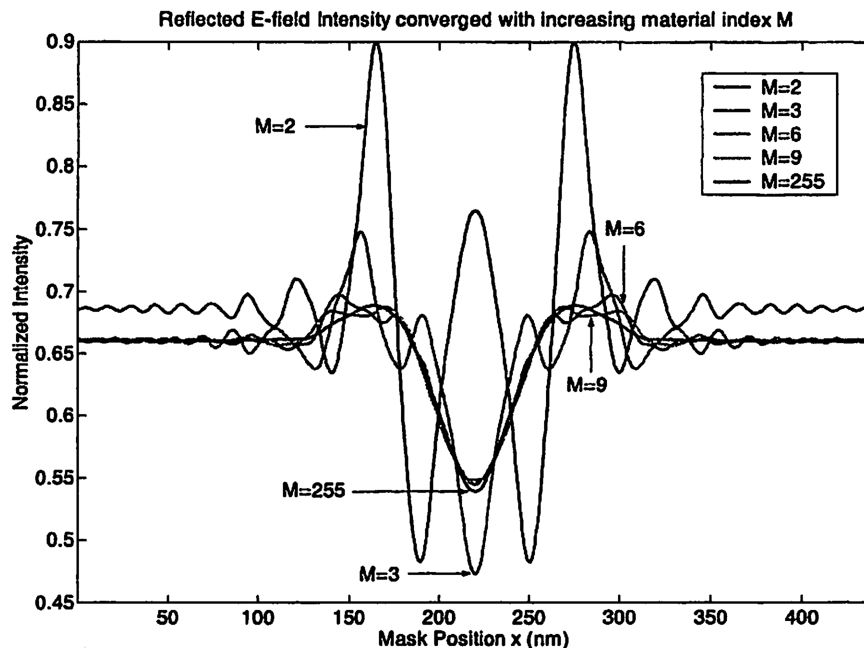

Figure 2-6. Reflected E-field from the Gaussian defect converges with more material indexes (M) used.

A series of two dimensional simulations of this Gaussian defect were carried out to investigate how many material grades (M) are required. In Figure 2-6, the near field intensity reflected from this 2D Gaussian line defect is plotted for various numbers of materials from 2 to 255. When only two materials are used (pure Si and pure Mo) the discretized representation of the defect looks like Figure 2-5 (c) and the near field intensity has strong ringing at the edges of the defect. This ringing is non-physical and due mostly to the step-discontinuities introduced by the poor discretization. As the number of materials increases, the near field intensity curve converges to a smoother, more physically believable curve. The error between using only 9 material grades and 255 material grades is minimal.

The second example is the study of the reflection signal from a sinusoid air/dielectric interface as shown in the insert plot of Figure 2-7. A refractive index of 2.0

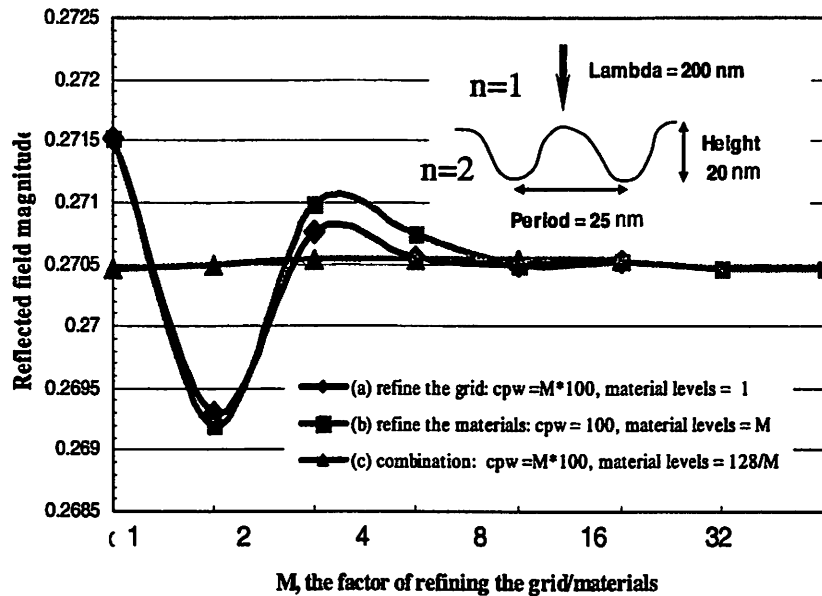

Figure 2-7. Reflection from a sinusoid air/dielectric interface for three simulation cases: (a) refining the grid with increasing cells per wavelength (cpw) and constant material levels (b) refining the materials with constant cpw and increasing the material levels (c) combination with increasing cpw and decreasing material levels such that the product is 12800. The number *M* gives the factor of refining grid density cpw in case (a) and (c), and the factor of increasing material levels in case (b).

for the dielectric and a wavelength of 200 nm are used. The sinusoid has a period of 25 nm and peak-to-peak height of 20 nm. This sinusoidal structure is studied by observing the magnitude of the reflected field using methods of refining the grid, refining the materials by the average material properties technique, and a combination of the two.

Figure 2-7 shows the magnitude of reflected field for different levels of refinement. The curve (a) is for refining the grid from 100 cells per wavelength (cpw) to 12800 cpw and using only refractive indexes of actual materials, air or dielectrics. The curve (b) is for keeping the grid at 100 cpw and refining the material levels from 1 to 128 using the refractive indexes of hypothetical materials that are weighted mixtures of air and dielectrics. The curve (c) is for the combination of two refinements and keeping the product of

the two refining factors at a constant value of 12800. Curves (a) and (b) show that the deviation from the asymptotic value of 0.2705 decreases from 0.4% to 0.04% in the same manner for two refining methods. Curve (c) shows that increased material refinement can be used to compensate the reduced grid refinement while maintaining the same accuracy level. The benefits are great speed improvement and a reduction in memory requirements, as TEMPEST simulation CPU runtime is related to the number of node n by n^4 and memory usage is related to n by n^3. Thus if refine the grid by a factor of M, effectively memory usage is increased by M^3, CPU run time is increased by M^4. But if refine the materials by a factor of M, it costs the same amount of memory and almost same CPU runtime. From this data, the advantage on memory usage and CPU run time by using this average material properties technique is significant. Thus it is used throughout the simulations in this thesis work, especially in the study of EUV multilayer structure with curved surfaces.

2.4 Parallel simulation with TEMPEST

Even with the above speed and memory improvement introduced by the average material properties technique, TEMPEST simulation still often is the 'bottleneck' of the whole simulation flow in the study of 3D EUV multilayer structures. This is because the EUV wavelength is only 13.4 nm which is relatively small compared to the size of EUV multilayer structures or simulation domain. To avoid numerical dispersion issues in the Finite Difference Time Domain computation, the cell size must be smaller than 1/15 of the wavelength in all dielectrics. Thus a cell size of 0.7 nm is usually chosen in EUV multilayer simulations. But the EUV multilayer needs at least 20 bilayers in the modeling

to capture majority of its reflection. Because low-profile Gaussian defects can have a lateral standard deviation of up to 100 nm, a 440 nm lateral dimension is often chosen in the simulation to make the defect fully isolated and avoid the effects of neighboring defects due to the periodic boundary conditions used on X and Y directions. Thus the 3D simulation domain needs 634 x 634 x 260 nodes in total to describe the EUV multiplayer topography. In the end, this 3D simulation approximately requires 3.5G bytes of memory, that exceeds the typical memory available in workstations and it takes more than 2 days to run.

This problem is solved by dividing the simulation domain and running the Finite Difference Time Domain algorithm respectively in each subdomain over a cluster of workstations. The communication between subdomains is handled by the Message Passing Interface (MPI) [13], a protocol of routines that allow multiple processes to communicate across an inhomogeneous network of workstations.

This parallel version of TEMPEST was first developed by T. Pistor [14] on small clusters. Later it was extended to run on the Millennium Cluster [15] at UC Berkeley, which has over 100 workstations interconnected by high-speed networks. Each of these workstations has 4 CPUs and was at 450MHz in the beginning. For the above 3D EUV multilayer simulations, it only takes about 5 hours to run in parallel on 16 processors.

The parallel version of TEMPEST was tested on the Millennium Cluster with a smaller sized problem to provide benchmark data on the performance of parallel operation. Series of simulations with domain size of 1000 x 1 x 220 nodes were tested for only 22 cycles on 1 to 80 processors. The execution time is plotted against the number of processors used in each run in Figure 2-8 (a). The execution time drops rapidly with the num-

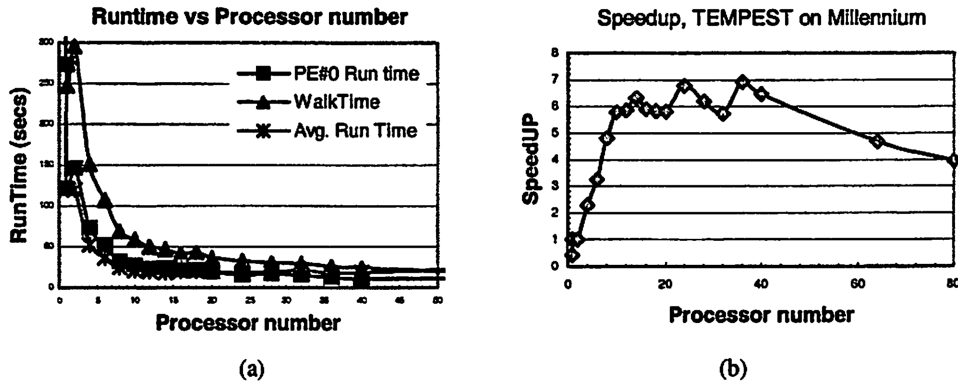

Figure 2-8. Benchmarks of parallel TEMPEST running on the Millennium Cluster: (a) the execution time (b) the speed-up.

ber of processors initially and then reaches a constant level. Figure 2-8 (b) plots the speed-up of TEMPEST simulations respect to the processor number. The speed-up factor is defined as the ratio of the execution time on 1 processor to the execution time on N processors. Figure 2-8 (b) shows that the speed-up is initially linearly increased to 6, which occurs at 10 processors. In the configuration of the Millennium Cluster, only four processors in the same workstation have the fast access to the share memory space between them. Any number larger than 4 means that communications happen across network and would be slower. It is encouraging that the speed-up continues beyond this shared memory boundary. When running with more than 10 processors, the speedup does not improve much and even decreases when the number of processors is larger than 40. The ripple in the data is likely due to conducting the tests in the presence of other users.

This behavior is expected according to Amdahl's Law [16] of parallel computation, which states that the maximum speedup that can be achieved by using N processors is:

$$\frac{1}{F+(1-F)/N}$$

where F is the fraction of computation must be executed sequentially, and (1-F) is the fraction that can be parallelized. So when N increases, the speedup does not increase as fast as N times but saturates at 1/F. The speedup in Figure 2-8 (b) actually decreases at very large N because of the communication overhead between processors and parallelization setup overhead.

The performance of parallel simulation with TEMPEST was demonstrated in another simulation of the pattern and probe based aberration monitors [17]. It is used as an practical test for performance of EUV nonplanar phase-shifting masks. Due to limited computation resources, a simple coma target is simulated instead of the full scale advance coma ring monitor. This simple coma target is composed with a small probe ($0.4*M*\lambda/NA = 21.76$ nm) in the center and two rectangle sidebars ($0.6*M*\lambda/NA$ x $1.2*M*\lambda/NA$). The underline multiplayer structure is assumed to have 20 Mo/Si bilayers. The whole domain has the width of $2.4*M*\lambda/NA$, and the height of $1.8*M*\lambda/NA$. With $M = 4$, $\lambda = 13.4$ nm, $NA = 0.25$, this coma target has sizes of 650 nm x 390 nm x 280 nm, or about 30000 λ^3. With a cell size of 0.7 nm, the whole simulation domain has 927 x 556 x 400 = 206 million nodes. The simulation runtime observed is about 10 hours when running on 16 Processors (699MHz).

Figure 2-9 shows the typical results extracted from simulations for this coma aberration target. The first kind of result is the topography or geometry setup in the simulation domain. Figure 2-9 (a) shows the sideview of the target, which has a 180° phase at the central probe and at the right sidebar. Figure 2-9 (b) shows the top view of the structure. The second kind of result is near fields diffracted from mask structures. Figure 2-9 (c) shows the near field intensity at the output plane, and Figure 2-9 (d) shows the near field

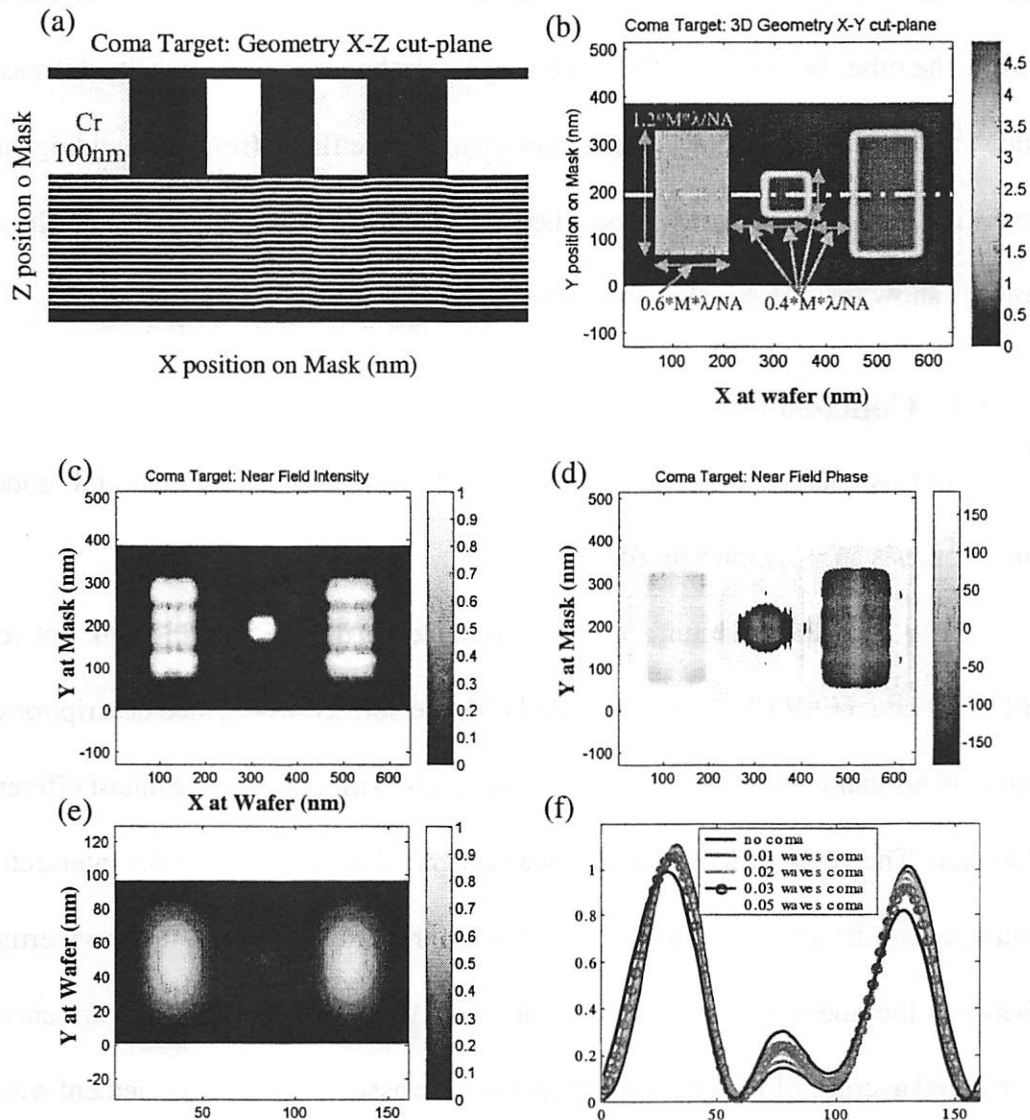

Figure 9. An example of pattern and probe based aberration monitors: (a) side view of coma target (b) top view of coma target (c) near-field intensity (d) near-field phase (e) aerial image without aberration (f) aerial image cut-lines with various amount of coma aberration.

phase, which has the correct phases for the probe and sidebars. The third kind of result is the aerial images formed at the wafer plane. Figure 2-9 (e) shows the aerial image of this coma target when no aberration is present. Figure 2-9 (f) plots the aerial image cut lines when there are different amounts of coma aberration present. The imaging intensity at the central probe increases quickly as the amount of coma aberration present increases. When

the coma aberration is 0.03 rms waves, the peak of the probe intensity increases 75% while the other two peaks at the sidebar openings have smaller intensity decreases. This is due to special design of the coma target such that the fields from surrounding patterns add constructively at the central probe when this specific aberration is present. The simulation results show that the simple coma target functions correctly as designed.

2.5 Conclusions

In this chapter, the process flow of electromagnetic simulation and modeling used in this thesis study is introduced.

The SAM2TEM interface was developed to fill the missing link between SAMPLE-3D and TEMPEST. With SAM2TEM, the surface-by-surface descriptions of multilayer films can be discretized for electromagnetic simulation via Finite-Difference Time-Domain. The volumetric description was generated by first finding the intersections of the surface with an array of vertical lines through the grid nodes and then converting regions between the nodes to indice of material types. Where fractional nodes are encountered a weighted average of material properties over the associated volume element was used.

The accuracy of this average material properties technique is examined. The test on EUV multilayer structure with 1 nm high Gaussian defect concludes that diffracted near fields converge to the physical result with the increase number of material grades used. The test on air/dielectrics sinusoid surface concludes that the use of the average material properties technique achieves roughly the same accuracy with the use of refined cell sizes for simulations with curved geometries while it also maintains roughly the original mem-

ory usage and run time. These significant advantages enable electromagnetic simulation on EUV non-planar multilayer structures.

Another enabling factor is the parallel simulation with TEMPEST on large clusters of workstations. TEMPEST was extended and tested on the Millennium Cluster. The benchmark on a typical 2D multilayer simulation shows that 6x speedup is obtained with 10 processors. The speedup factor reaches 7 at 24 processors and decrease with more processors due to the overhead of parallelization and communication. A large 30,000 cubic wavelength simulation on a EUV coma target is used to demonstrate the capability of parallel simulation with TEMPEST.

2.6 References

[1] E. W. Scheckler, A. R. Neureuther, *IEEE Trans. on CAD of Integrated Circuits and Systems*, pp. 219-230, 1994.

[2] A. Taflove, *Computational Electrodynamics The Finite-Difference Time-Domain Method* (Artech House, Norwood, MA, 1995).

[3] A. Wong, "Rigorous Three-Dimensional Time-Domain Finite-Difference Electromagnetic Simulation," Ph.D. Dissertation, University of California at Berkeley, 1994.

[4] T. Pistor, "Electromagnetic Simulation and Modeling with Applications in Lithography", Ph.D. Dissertation, University of California at Berkeley, 2001.

[5] P. D. Flanner III, "Two-dimensinal Optical Imaging for Potolithography Simulation", M.S. Thesis, University of California at Berkeley, May 1986.

[6] K. Toh, "Two Dimensional Images with Effects of Lens Aberrations in Optical Lithography," M.S. Thesis, Memorandum #UCB/ERL M88/30, University of California at Berkeley, May 1988.

[7] Ebo Croffie, "Moving boundary models and methods for deep submicron resist process simulation", M.S. Thesis, Memorandum #UCB/ERL M96/26, University of California at Berkeley, May 1999.

[8] M. Brukman, Y. Deng, A. R. Neureuther, "Simulation of EUV Multi-layer Mirror Buried Defects", *Proc. SPIE, Optical and EUV Lithography*, March 2000.

[9] K. K. H. Toh, A. R. Neureuther and E. W. Scheckler, *Algorithms for Simulation of Three-Dimensional Etching*, IEEE Trans. CAD, Vol. CAD-13, No 5, pp. 616-624, May 1994.

[10] T. Pavlidis, *Algorithms for Graphics and Image Processing* (Springer-Verlag, Berlin, 1982).

[11] F. Preparata and M. I. Shamos, *Computational Geometry, an Introduction*, (Springer-Verlag, New York, 1985).

[12] Dey, S. and R. Mittra, "A conformal finite-difference time-domain technique for modeling cylindrical dielectric resonators", IEEE Trans. Microwave Theory and Techniques, vol. 47, pp. 1737-1739, 1999.

[13] Message Passing Interface Forum, "MPI: A message-passing interface standard", *International Journal of Supercomputer Applications*, 8(3/4), 1994.

[14] T. Pistor, *Expending the Simulation Capability of TEMPEST*, Electronics Research Laboratory, University of California, Berkeley, 1997.

[15] Millennium Cluster website, http://www.millennnium.berkeley.edu/.

[16] G. Amdahl, "Validity of the Single Processor Approach to Achieving Large-Scale Computing Capabilities", *AFIPS Conference Processdings*, (30), pp. 483-485, 1967.

[17] G. Robins, K. Adam, and A. R. Neureuther, "Measuring Optical Image Aberrations with Pattern and Probe Based Targets", *J. Vac. Sci. Technol.* B, Nov/Dec (2001).

3 Modeling EUV Multilayer Structures

3.1 Introduction

Extreme Ultraviolet Lithography (EUVL) [1-2] is the leading candidate of next generation lithography (NGL) technologies, and considered as the likely successor to optical projection lithography or DUV Lithography. Though in many ways EUV Lithography may be viewed as the natural extension of DUV Lithography as it keeps many aspects of optical project printing, there are major differences between these two technologies. These differences are mainly because the material properties at EUV wavelengths are very different from their properties at DUV wavelengths, such as the strong absorption in almost all materials preventing from the use of refractive elements. Due to these differences, many unique technology challenges arise such as the needs for near vacuum environment, stand-alone light sources powerful enough for high-throughput volume production, reflective-only optical elements with surfaces polished to an unprecedented degree of perfection, ultra thin resists, replacement of pellicle, and so on [3-4].

EUV multilayer structure is an essential part of EUV Lithography multilayer coatings are on surfaces of all reflective optical components in the system. The multilayer reflector is also the component which provides high reflection in the EUV mask blanks. The multilayer reflector consists of alternately deposited layers of high-Z and low-Z ma-

terials with desired layer thickness. Defects or any deviations from ideal geometry in the multilayer structures may cause the degradation of imaging performance or even worse defects in wafer imaging. Thus the quality of the multilayer structure directly relates to the quality of EUV masks and remains a challenge for lowering the cost of ownership (COO) of EUV masks [5-6]. Figure 3-1 shows the system diagram of EUV Engineering Test Stand (ETS) and the EUV light path reflected at the multilayer mask.

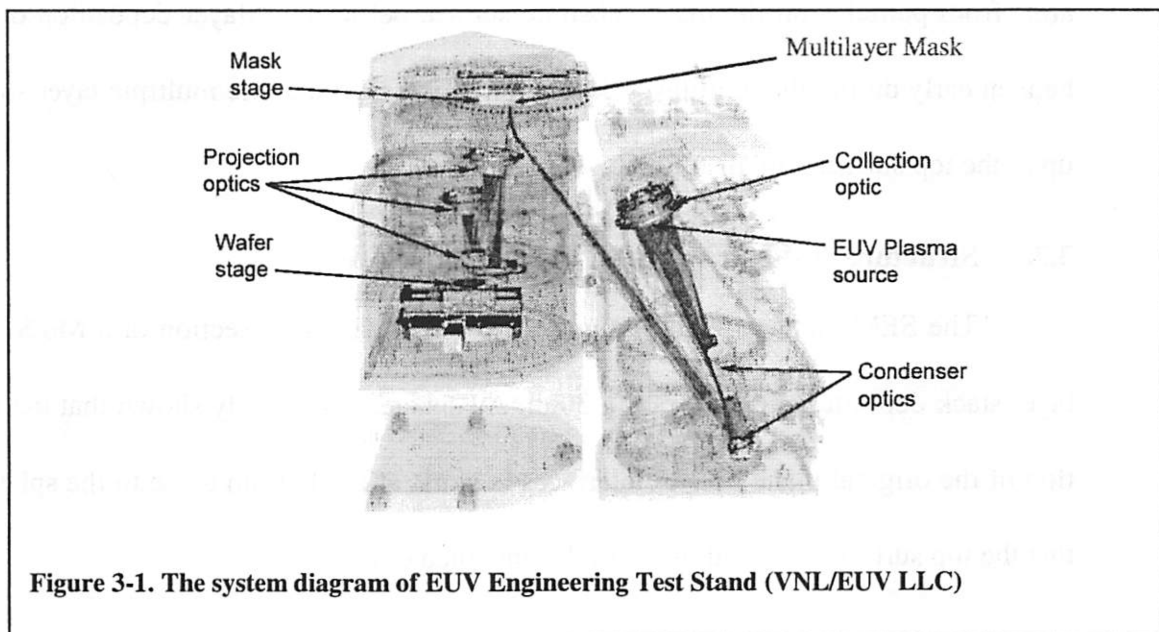

Figure 3-1. The system diagram of EUV Engineering Test Stand (VNL/EUV LLC)

This chapter will discuss the modeling of EUV multilayer mask structures and results from rigorous electromagnetic simulations. There are two main parts in this chapter. In the first part, the buried substrate defect in the multilayer mask blank is analyzed for near field electromagnetic effects with its geometry at first. Then the defect printability in EUV imaging is analyzed algebraically and compared with simulation results under various conditions. The second part of the chapter considers the direct use of patterned or d-spacing modified multilayer structures as photomasks.

3.2 EUV Multilayer substrate defect structures

Mask defects are a major concern in all projection printing systems and especially in EUV Lithography where the multilayer deposition process adds additional sources of defects. Besides those patterning defects similar to DUV Lithography which happen during mask patterning process, one additional kind of EUV mask defects is the defect in the multilayer structure or the mask blank itself. This kind of defect, called substrate defects, arise from particles on the mask substrate surface before multilayer deposition or it can happen early during the multilayer deposition process, so that the multiple layer structure up to the top surfaces are distorted.

3.2.1 Structure of substrate defect in EUV multilayer

The SEM picture [8] in Figure 3-2 (a) shows the cross section of a Mo/Si multilayer stack deposited on the top of a 30nm Au sphere. It is clearly shown that the distortion of the original plane bilayer interfaces is worst at the bottom close to the sphere and that the top surfaces are kind of naturally smoothed out.

As shown in the last chapter, SAMPLE3D NETCH simulator can be used to simulate the general deposition process of multilayers [8]. P. B. Mirkarimi [7] also inves-

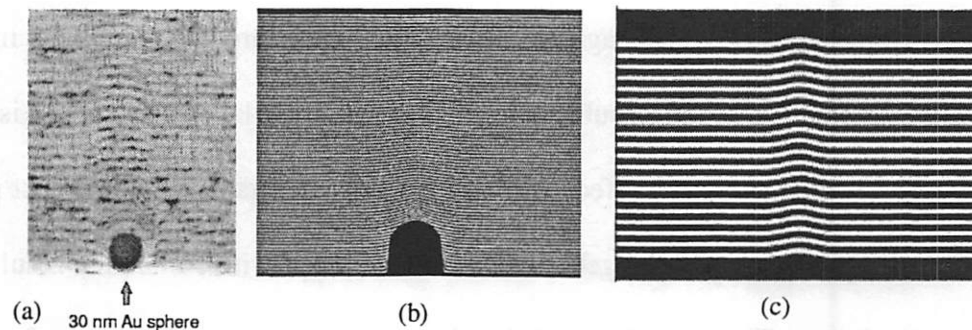

Figure 3-2. Geometry of multialyer substrate defect: (a) SEM picture from P. B. Mirkarimi (b) simulated profile with deposition model (c) simpilied Gaussian profile

tigated the ion-sputtering process experimentally using the programmed gold nanospheres and developed a thin film deposition model. His study offered insights to improve the ion-sputtering process with additional etching in the deposition of each layer so that the final multilayer surfaces are greatly smoothed, especially for the surfaces near the top. Figure 3-2 (b) shows the multilayer geometry simulated from his model. Even surfaces at or close to the top layer are very flat after smoothing, their remaining non-flatness may still be optical significant as EUV radiation has a very small wavelength of 13.4 nm. Thus the prediction of its effects in imaging, *aka* defect printability, is very important to obtain a defect-free multilayer mask blank.

Though it is more rigorous to simulate the full multilayer stack from physical modeling, due to the limited computation resource, the multilayer with substrate defects is often simplified so that there are only 20 Mo/Si bilayers and all surfaces from bottom to top have identical Gaussian shaped profiles, because those 20 bilayers account for essentially all of the reflected light and they have almost exact profile after smoothing.

TEMPEST is applied for the rigorous electromagnetic simulation study of these substrate defects. In the simulations, the defects are assumed to be isolated in the domain, though the domain has periodic boundary condition applied on X and Y directions. The 3D simulation domain is constant and has physical size $Lx = Ly = 440$ nm, and $Lz = 180$ nm with node density of $dx = dy = dz = 0.7$ nm, which is divisible by the Mo layer thickness (2.8nm) and Si layer thickness (4.2nm) in the multilayer structure. The 2D Gaussian defect simulations in this paper also have the same Lx and Lz. The geometry of such Gaussian defects is shown as in Figure 3-2 (c).

The EUV imaging optics is assumed to have M=4, σ=0.7, NA=0.25. SPLAT program is used for aerial image simulation. At EUV wavelength, λ = 13.4 nm, Si has a refractive index of 0.999931 - j*0.00182108, Mo has a refractive index of 0.922739 - j*0.00621991 and chrome has a refractive index of 0.933328 – j*0.0381974. The EUV radiation is incident from 6° from normal and excited at the top of domain. The reflection output plane is above the excitation plane.

3.2.2 EUV multilayer substrate defect printability: analytical model

A simple analytical model for the substrate defect printability in EUV Lithography is much needed as a quick reference during EUV multilayer mask blank development, because it can provide guidance in drafting specifications of EUV multilayer mask blank at earlier stage. It is desirable that this analytical model can predict the aerial imaging profile and thus the printability of EUV multilayer substrate defects with variable size and height under different imaging conditions. The Gaussian shape profile of a buried substrate defect is more difficult to model algebraically than the traditional small (constant height and phase) top-hat defect. Eric Gullikson [9] has worked out such an analytical model that takes into account the Gaussian shape.

This model makes three basic assumptions when calculating the aerial images of the defect: (1) coherent illumination (2) defect is small and thus unresolved by the optics and (3) the phase of rays reflected from the defect can be estimated by local vertical propagation. We now follow the dev elopment of Gullikson's model and highlight these three assumptions. In the next subsection, the model is compared with rigorous electromagnetic simulations results and three assumptions are analyzed respectively.

Under the first assumption, when the illumination is perfectly coherent, we can calculate the far field U(x, y) in the image plane by integrating the fields at the exit pupil P of the lens.

$$U(x,y) = -\frac{e^{-ik\rho}}{2\pi\rho}\int_P S(u,v)e^{-ik(ux+vy)/\rho}dudv$$

Since the field at exit pupil is just proportional to the scattering amplitude S(u, v). The scattering amplitude is related to the near field at the mask by the diffraction integral. Where (x, y) is the position at the image plane, and (u, v) is the position in the exit pupil which is located at a distance ρ from the image.

Under the second assumption, when the defect is too small to be resolved by the lens optics, the light scattered by the defect can be assumed to be evenly distributed over a wide range of angles. In this condition, the scattering amplitude S(u,v) can be assumed to be constant over the exit pupil of the lens. So the last equation can be rewrite as:

$$U(x,y) \approx -\frac{\lambda^2 S(0)}{2\pi}\int_P e^{-i2\pi(f_x x+f_y y)}df_x df_y, \qquad f_x = \frac{u}{\rho\lambda} \;\; and \;\; f_y = \frac{v}{\rho\lambda}$$

The integration over the pupil gives the amplitude point spread functions of the lens, so that the far field at the image plane can be express by a simple point spread function:

$$U(r) \approx -\frac{\lambda^2 S(0)}{2\pi}PSF(r)$$

The aerial image intensity I(r) is:

$$I(r) = |1+U(r)|^2 \approx 1-\frac{\lambda^2 S(0)}{\pi}PSF(r)$$

Expressing the scattering amplitude by the total extinction cross section according to the optical theorem gives:

$$I(r) \approx 1 - \sigma PSF(r), \quad \sigma = \frac{\lambda^2 S(0)}{\pi}$$

For the sub-wavelength defect usually considered, there is a minimum at the center of the image with dip size:

$$\Delta = 1 - I(0) \approx 1 - \sigma PSF(0) = \frac{\sigma}{r_0}, \quad r_0 = \frac{M\lambda}{\pi NA}$$

For the 2D case of a line defect, the image dip is:

$$\Delta = 1 - I(0) \approx 1 - \frac{\sigma}{L} PSF_1(0) = \frac{2\sigma}{\pi r_0 L}, \quad r_0 = \frac{M\lambda}{\pi NA}$$

Thus the aerial image can be obtained once the total extinction cross section σ for an arbitrary defect under the first two assumptions is known. The total extinction cross section σ can be measure by experiment, but it is good to have a way to calculate it from the topography of the defects. For a full analytic model of Gaussian defects, an analytical formula for the total extinction cross section is needed.

Under the third assumption of the single surface approximation or the vertical propagation model, the reflected near field can be calculated from the topography profile or the optical path function. For a defect with height profile H(x, y), the phase at the extraction plane can be calculated by adding the round trip phase difference, 4π*H(x, y)/λ. The amplitude of the near field is assumed to be unchanged. So the total scattering cross section is:

$$\sigma = \frac{\lambda^2 S(0)}{\pi} = 2\int (1 - \cos(\frac{4\pi * H(x,y)}{\lambda}))dxdy$$

For the Gaussian shaped defects, the height profile has two parameters, peak height=H_0 and width=2*sigma,

$$H(x,y) = H_0 * e^{-2(x^2+y^2)/W^2}$$

The resulted integral cannot be found in closed form but can be obtained via numerical integration. Since the total scattering cross section σ is proportional to the square of the defect width, it can be also calculated for other defects once the scattering cross section of one defect width is obtained through simulation.

3.2.3 EUV multilayer substrate defect printability: simulation results

Gullikson's analytical model is approximate in nature due to three assumptions mentioned in the previous section. The accuracy of the above model needs to be analyzed and verified to determine the scope of its application. Early experimental results of EUV scattering from multilayer with substrate defects are used to validate the analytical model in Gullikson's paper [9]. But rigorous electromagnetic simulation has the advantages of speed and flexibility in investigating various scenarios, so it is more convenient tool to analyze the accuracy degradation due to each of assumptions. We now use simulation to examine each of the three key assumptions of the model [10].

The first assumption in the analytical model is that the EUV lithography system uses perfectly coherent illumination. Figure 3-3 shows the aerial images calculated by TEMPEST simulations for two values of coherence factor, σ=0.1 and σ=0.7. The two curves have almost the identical imaging minimum at the center, and this quickly verifies that the first assumption in the model is valid generally.

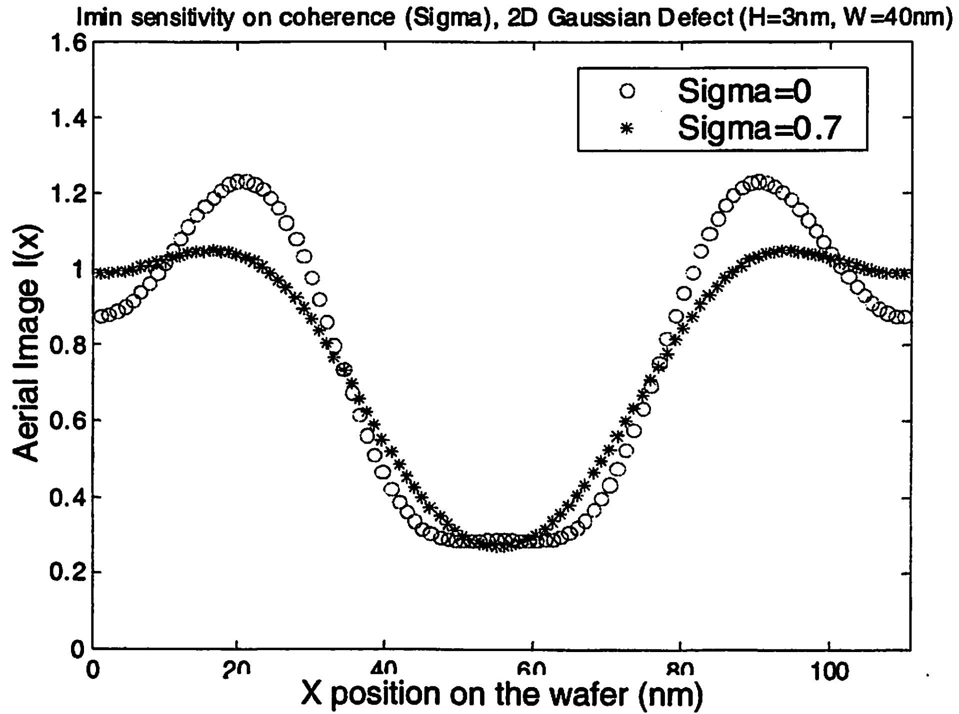

Figure 3-3. Aerial images of 2D Gaussian defect under two different coherence factors

The second assumption is that the defect is sufficiently small that the light scattered from the multilayer fills the lens uniformly. This is so that the scattering amplitude function S(u, v) can be approximated by the constant, S(0). Eric Gullikson provided one criterion based on at most 30% of the broadly scattered light being collected by the lens. This gives

$$FWHM = 2.35 * sigma < 0.2\frac{M\lambda}{NA}$$

Another criterion is the maximum size of defects on which the simulation results and model calculation agree to within 5%.

Top-hat shaped defects are used for checking this criterion than Gaussian shaped defects because they can be simulated via SPLAT with thin-mask model. Figure 3-4 and Figure 3-5 show the aerial image minimums *Imin* calculated from the analytical model

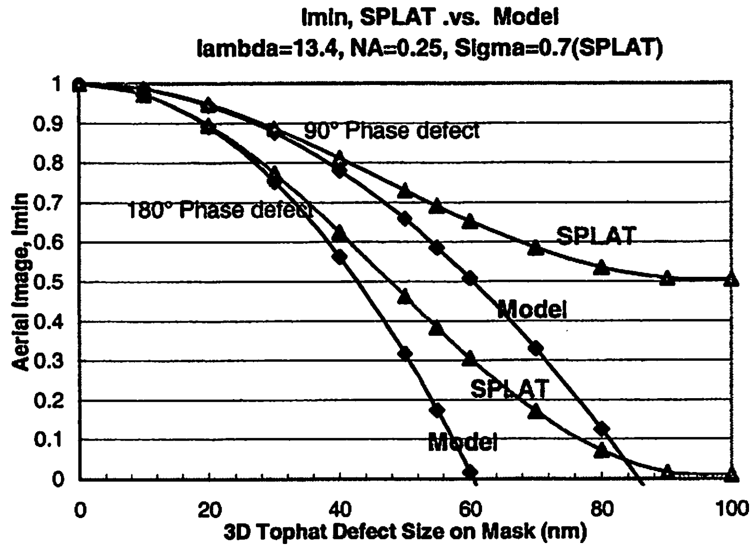

Figure 3-4. Aerial image minimum of top-hat defect at NA=0.25

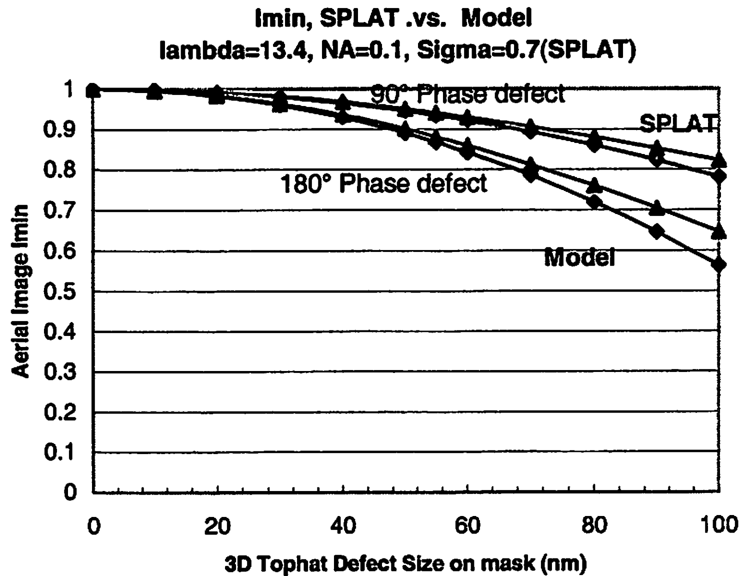

Figure 3-5. Aerial image minimum of top-hat defect at NA=0.1

and SPLAT simulation for a three dimensional top-hat phase defect with sizes from 0 nm to 100 nm. The upper curve is for a height of 1/8 wavelength (90 degree round trip phase difference) and the lower curve is for a height of 1/4 wavelength (180 degree round trip phase difference). Because SPLAT uses the thin-mask approximation which is the same

as the vertical-propagation model in this case, both methods satisfy the third assumption. Thus the difference between these two results must come from the second assumption concerning the angular diffraction.

The simulation results in Figure 3-4 shows the typical trend of the aerial image minimum of EUV substrate defects under the condition of NA=0.25. When the defect size increases, Imin drops from 1 slowly for both methods. Then around a critical defect size of 40 to 50 nm, the model results drop with increasingly larger slope down to 0. From this critical defect size, the simulation results drop more slowly and with decreasing slope and gently reach a minimum then increase again.

The simulation results in Figure 3-5 are under the condition of NA=0.1. The smaller NA gives a smaller collection angle so that the approximation of S(u, v) by S(0) in the second assumption has a smaller error. Since the aerial image dip is less than that predicted by the model, it confirms that less light scattered by the defect is collected by

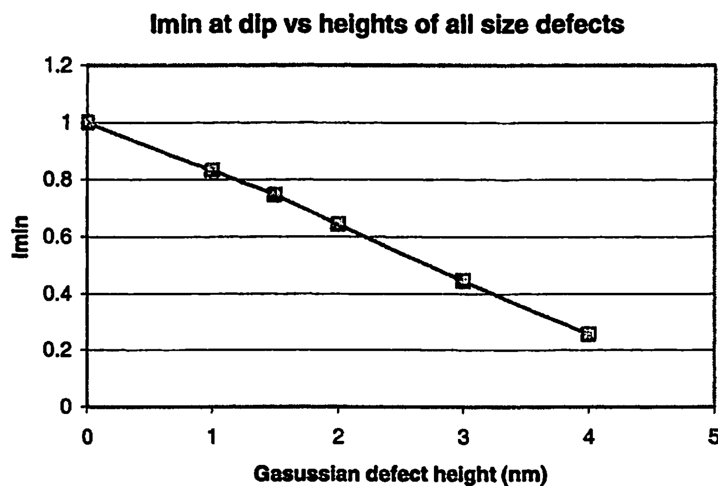

Figure 3-7. Imin for the worst-sized defect as a function of defect height.

the pupil. The critical size where the error in the second assumption is more than 5% is 40nm for NA=0.25, and 100nm for NA=0.1 for 4X reduction systems. Unfortunately, these critical sizes are smaller than the isolated defect sizes that are likely to be acceptable in determining guidelines for defects. Thus guidelines for defect printability derived from the theory will likely be overly conservative.

The third assumption made in the calculation of total scattering cross section is vertical propagation model. This assumption is only valid when the defect height is small enough compared with its width so that the scattering by the small slope keeps the light near its original path and creates little lateral movement or interference. The multilayer structure itself also has an angular bandwidth. Angles of less than a few degrees (<10°) could be tolerated by both phenomena. The low-profile Gaussian defects on the order of 60 nm in size, which might be of concern in printing, have slopes that are at most a few degrees.

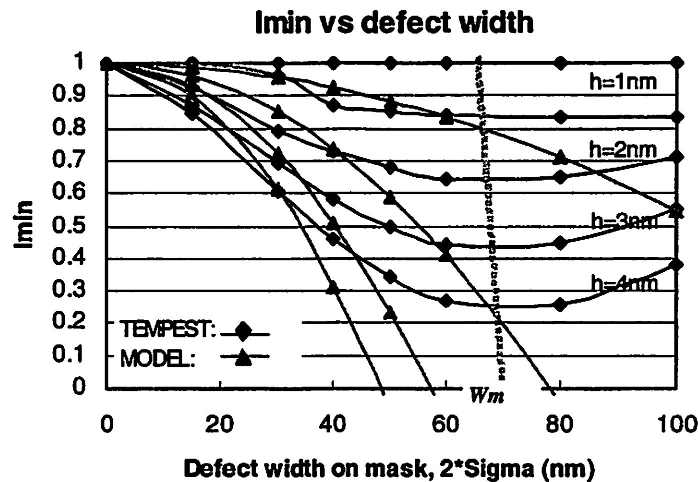

Figure 3-6 . Comparison of Imin for Gaussian defects between rigorous simulation and analytical model.

Simulation and the model results for 3D Gaussian defects are given in Figure 3-6 for a full set of defect heights and sizes. The trend is nearly identical to the top-hat case in Figure 3-4 for top-hat defects. This is a clear indication that the assumption of uniform filling of the lens pupil is breaking down and limiting the model. As expected the Gaussian defects have less of a dip for the same height.

The data in Figure 3-6 shows that when defect width is below 30nm, results from simulation and the analytical model agree quite well. At the width 40nm which is around the critical size *Wc*=2*sigma=36.5nm for the second assumption, two methods agree in the cases of small defect height (<3nm) and they do not agree well at the defect height=4nm. The large difference at height = 4nm is believed to come from the bad approximation by the third assumption because the vertical propagation model over-estimate the total scattering cross section at height=4nm. If calculate the scattering angle approximately by θ = atan(defect height / (defect width/2)), the angle obtained 11.3° is above the threshold of 10°. When the defect width is larger than 40nm, the second assumption breaks down so that the analytical model results do not agree with simulation results.

It is interesting to note that the Gaussian defects also all tend to have their worst-case in the *Wm* around 70 nm. Further, the size of the dip is very linear with the defect height as shown in Figure 3-7. The slope is about 18% of the clear field per nm of Gaussian defect height. Note that for a 2 nm defect the minimum intensity is greater than 60% of the clear-field value. This empirically behavior in Figure 3-7 allows more lenient defect criteria to be stated. Namely, the worst defect size for isolated Gaussian defects in EUV

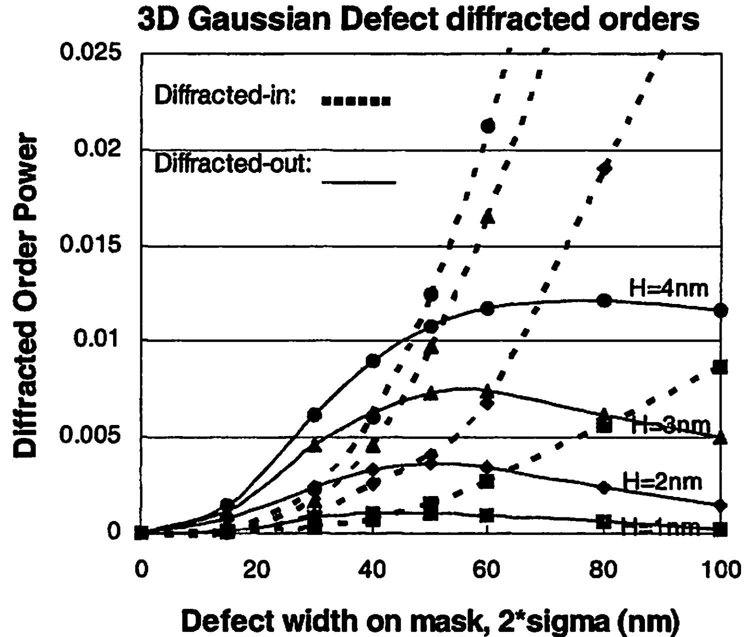

Figure 3-8. Diffracted order powers for 3D Gaussian defects

systems is 0.3 λ/NA at the wafer, and the clear field intensity will be greater than 60% when the height is less than 2 nm.

To understand the critical defect size *Wc* and the worst-case defect size *Wm*, it is helpful to observe the energy distribution among the diffracted orders. After subtracting the contribution of the flat multilayer, the diffracted orders are categorized into two groups: Diffracted-in and Diffracted-out. Diffracted-in orders are the light diffracted by the defect and then collected by the lens. Diffracted-out orders are the light diffracted by the defect out of the lens. Figure 3-8 shows how powers of these two groups vary with the defect height and width. The power of diffracted-in orders increases exponentially with the width so that it exceeds the power of diffracted-out orders at defect size about 40~50 nm. The definition of critical size *Wc* requires that the power of diffracted-in orders

increases to 30% of the power of all diffracted orders at *Wc*, which can be found from Figure 3-8. It reads 36nm which agrees with the formula.

Figure 3-8 also shows that the power of diffracted-out orders increases fast at very small defect sizes, and then increases slowly around *Wc* until it reaches the maximum value around 60~80nm, which suggests that the power of diffracted-out orders reaches a maximum around the worst-case defect size *Wm*. The decreasing of diffracted-out order power is the reason that the aerial image minimum stops decreasing and begins to increase at *Wm*.

3.2.4 Effect of multilayer roughness on defect printability

EUV multilayer is made via multiple depositions of bilayers with two materials using magnetic sputtering or ion-beam sputtering process. With the continued improvement of multilayer deposition process, the reflectivity of multilayer mirrors is near the theoretical limit. Even though the random variations in the deposition process could be small, but those variations would still result non-ideal multilayer profile. Compared with the multilayer profile change resulted from buried particle defects, the surface roughness in the multilayer is a much smaller random variation, such as it would only result a second order effect on the optical imaging of EUV multilayer masks. But as EUV Lithography is advancing beyond the prototype phase, it is important that all factors be well characterized. Previously there has been discussion [11-13] on the multilayer roughness is from optical system point of view, we will study the effects of multilayer roughness on defect printability via rigorous electromagnetic simulation [14].

In this study, two types of roughness are considered. The first type, termed "Model X", describes roughness due to the random local variation of layer heights over a correlation length L_c such as that which might arise due to local grain structure, uneven inter-diffusion at material boundaries, or deposition on a very rough substrate. Here we considered random height variation on only one lateral dimension x for 2D simulation such as shown in Figure 3-9 (b). For 3D cases we apply this surface operator in both x and y directions and term it "Model XY". The second type of roughness, termed "Model Z", describes the roughness due to random variation in global layer thickness caused by variation in deposition rates or deposition time. These two types of roughness may co-exist, in which case two height variations are added.

In Model X, the roughness is described at the k-th interface by a one-dimensional height function $H_{x,k}(x)$ as a random, but correlated, discrete variable. Numerical values are generated using the moving average method. The height at position x_n is the weighted average of N (>>1) independent uncorrelated Gaussian distributed random variables u_n as:

$$H_{x,k}(x_n) = \sum_{m=0}^{N} w_m u_{n-m}$$

The random variable u_n has zero mean and standard deviation equal to the RMS roughness height. The weight parameters are w_n chosen so that the height has a Gaussian correlation function:

$$Cor_m = Cor(m\Delta x) = \exp\left\{-\frac{(m\Delta x)^2}{L_c^2}\right\}$$

where Δx is the node size. For a finite correlation length L_c, the weights are approximated by

$$w_m = w_0 \frac{1}{\sqrt{L_c}} \exp\left\{ -\left[\frac{2(m\Delta x)^2}{L_c^2} \right] \right\}$$

where w_0 is the normalized factor to make $<H_{x,k}(x)^2> = < u_n^2 > = \text{RMS}^2$. For Model Z, each planar surface height is a Gaussian distributed random variable $H_{z,k}$ with zero mean

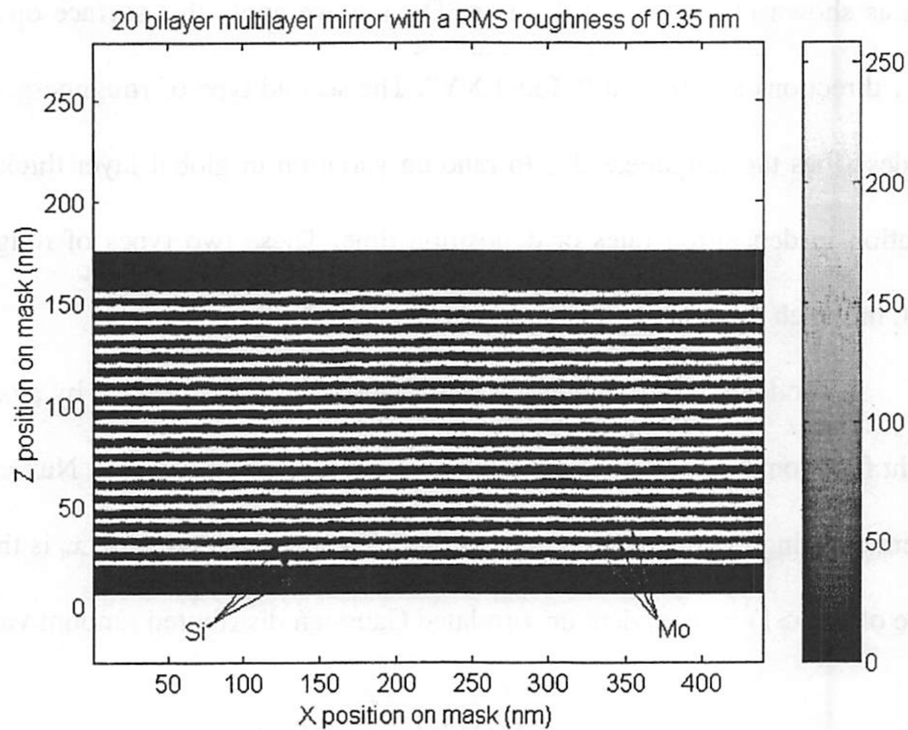

(a)

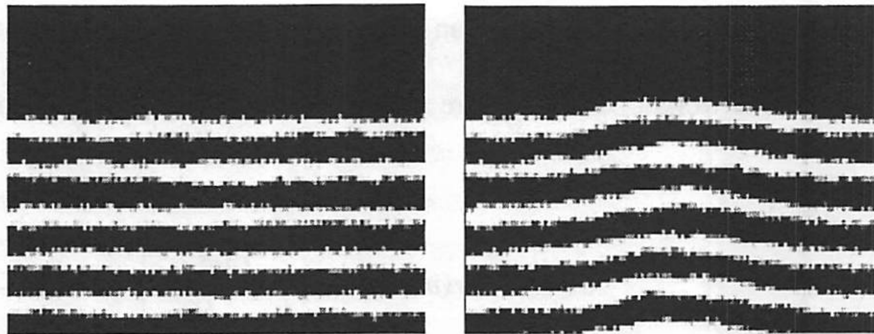

(b) (c)

Figure 3-9. Topography of multilayer structures with Model X for (a) flat multilayer in the whole domain (b) its close up and (c) a close up of a low profile Gaussian defect.

and standard deviation equal to the specified roughness RMS.

Figure 3-9 shows the topography of the multilayer with roughness for (a) flat multilayer, (b) its close up, and (c) the close up for a low profile Gaussian defect for Model X with a RMS roughness of 0.7 nm. For clarity the default RMS roughness value is 0.7 nm and the correlation length L_c is 7 nm in this study.

The multilayer reflectivity will be reduced due to multilayer roughness. In Model Z, the reflectivity drops because the coherent interference is destroyed due to the variation of bilayer thickness different away from one quarter of wavelength. In Model X, reflectivity drops more slowly with RMS roughness because the small random surface roughness only slightly scatters light away from the specular wave.

Besides affecting the reflectivity, the scattering from the rough multilayer mask will also affect the phases of the near fields. Simulation results shows that there is a negative phase shift with the TE polarization and positive phase shift with the TM polarization at small roughness. This appears to be due to the penetrating waves in the TM case. The roughness may also cause the modulation of the image, such as a line width variation [12]. It is estimated that a multilayer roughness of 0.7 nm RMS will cause 0.3 nm RMS in phase roughness and also 0.3 nm RMS in line width variation based on the data in Figure 6 of [12].

Roughness was also introduced in the multilayer structure for low profile Gaussian defects to assess the impact in imaging. Figure 3-10 shows the aerial image minimum I_{min} for Gaussian defects with various sizes under conditions of no roughness, roughness with Model Z, and roughness with Model X. Different random seeds were used in each simulation instance so that the difference in the surface structure also contributes

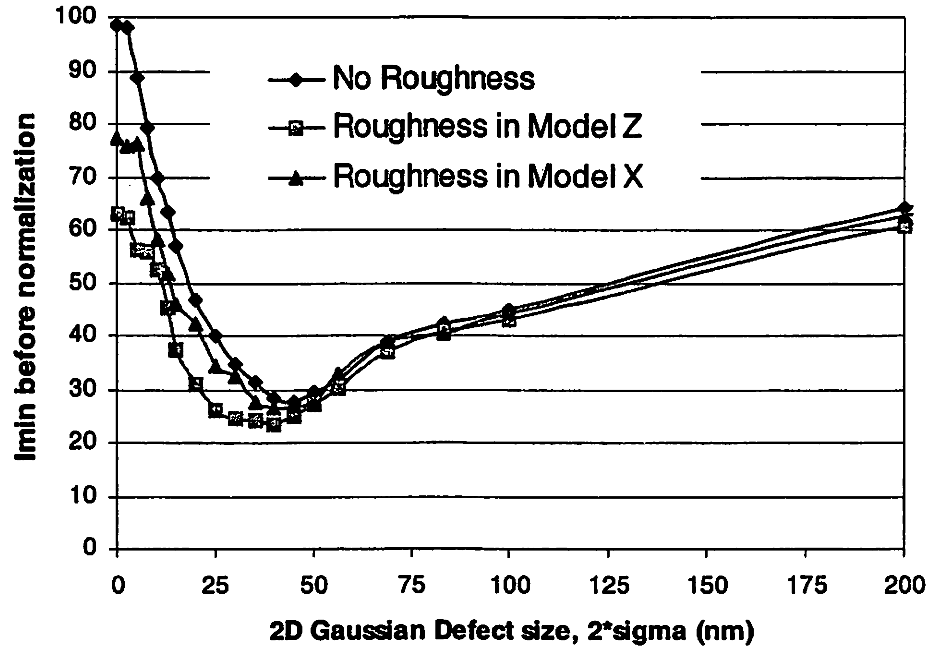

Figure 3-10. Aerial image minimum for Gaussian defects of different defect sizes with various types of roughness.

to the fluctuation among three curves. The effect of roughness on I_{min} is large at small defect sizes since roughness greatly reduces multilayer reflectivity. With increasing defect size, the difference between the three curves becomes smaller. Finally, the curves diverge because the very large Gaussian defects become effectively flat. If the I_{min} for zero width (no Gaussian defect) is used for normalization in each case, the normalized aerial image dip curves are roughly the same in the small defect size range and diverge for a width greater than 35nm. The presence of roughness shows a 16% mitigating effect of defect printability for mid-size defects since the normalized I_{min} with roughness is not as deep. These results were obtained at a large roughness RMS (0.7 nm). For a roughness more typical of EUVL systems (0.15 nm), the difference of I_{min} is under 2% and thus it is insignificant.

3.2.5 Substrate defect printability after E-beam repair

Mask defects are a major concern in all projection printing systems and especially in EUV where the multilayer deposition process adds additional sources of defects. Post mask-writing inspection, defect classification and repair are viewed as essential for mitigating the occasional defects and thereby reducing overall mask costs. However, entirely new approaches are needed for the multilayer structures in EUV. For example, repair treatments must be developed that can deal with the third dimension or depth of the multilayer film and maintain the reflective of multilayer.

Anton Barty [15] systematically classified various multilayer defect types to be matched up with repair approaches. Depending on properties of aerial image caused by these defects, they can be roughly categorized into two categories. One category is called 'amplitude defect' because it mainly change the amplitude of reflected near fields. It might be created by an opaque particle deposited at the top few bi-layers or on the top of the multilayer, or any damage to the top multilayer period structure. The other category is called 'phase defect' because they mainly change the phase in the reflected near fields. They are usually the substrate defects discussed in the previous subsections, which are generated by particles or defects on the substrate before multilayer coating or by defects deposited in the first few bottom layers.

For amplitude defects, T. Liang [16] suggested using a focused ion beam to physically remove the particle and any damaged multilayer coatings around the defect region to restore the multilayer reflectivity. For phase defects, P. B. Mirkarimi [17] suggested using a high-resolution e-beam to locally heat the defect region of multilayer so that the silicide is formed at the interface. Due to the higher atomic density of silicide than that of pure

Mo/Si bilayers, the multilayer structure is contracted. The high electron beam can penetrate through the multilayer deeply down to the substrate so that the entire layer structure is heated and contracted. Thus the change is distributed through the whole multilayer. Effectively, the surface profile at the defect is lowered due to contraction, and the multilayer structure has a slightly smaller period than that of the untreated region. The primary effect is the lowering of the non-planar surface height, which increases the phase of the near field and makes both the phase and amplitude at the defect position similar to that of the region without defects. This subsection we focus on imaging performance of phase defects after such e-beam repair [18].

In the simulation, the period of the multilayer structure at the treated phase defect region is assumed to be uniformly decreased for easy of geometry creation as shown in Figure 3-11 (a). Figure 3-11 (b) shows the multilayer geometry modeled in TMEPEST after the e-beam treatment has been applied. Here again only the top 20 bi-layers are modeled. The repaired multilayer profiles are obtained by deceasing the multilayer period at the Gaussian defect position and applying an erfc function to characterize the transition from this decreased period to the normal period. The sigma of the erfc function has been

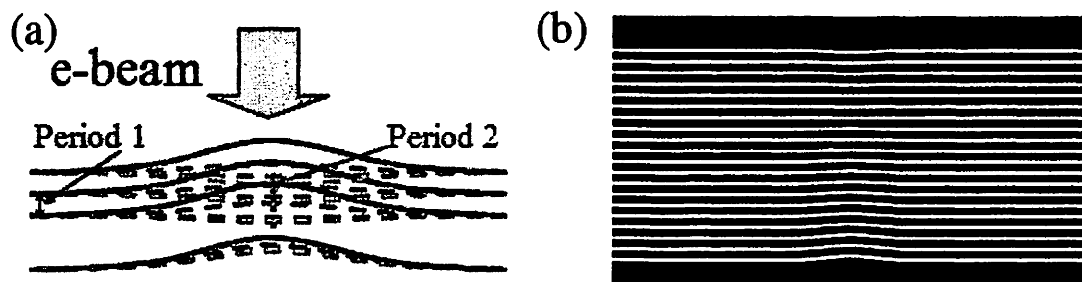

Figure 3-11. (a) sketch of e-beam repair of phase defects (b) geometry of phase defect after

chosen to match the sigma of the Gaussian defect profile.

A 2D Gaussian defect with height of 3 nm and 2-σ width of 40nm is simulated with several amounts of repair applied (0, 3, 4.5, and 6 nm respectively). The amount of defect repair is defined as the decrease of the peak height of the top surface layer profile relative to the flat multilayer, which is modeled as the product of the number of bi-layers and difference between the multilayer period at the repaired region and the nominal period.

Figure 3-12 (a) shows the reflected near field phase of the repaired defect. When there is no repair, the maximum phase difference at defect location is about -150°. Then the repair increases the phase at the defect position and almost planarizes the phase at a 4.5 nm repair. The phase difference becomes positive when the repair amount is 6 nm. As shown in Figure 3-12 (b), the overall effect of defect repair on the aerial image is that the aerial image dip decreases as little as 3% at a 4.5 nm repair. The aerial image dip increases again when amount of repair is 6nm, which cause the phase over-corrected at defect location as shown in Figure 3-12 (a). This shows that the planarization of reflected phase from phase defects is critical to minimize the aerial image dip. The reason that the best repair amount 4.5 nm is larger than the Gaussian defect height 3 nm, is because the reduction of multilayer bilayer thickness in the defect treatment region also causes an additional phase shift from multilayer interference.

Overall these simulation results show that an optimum amount of e-beam treatment effectively removes the phase defect, but over-repair can cause the opposite type of phase defect and the resulted multilayer structure is hard to be repaired again. Since the

reflected phase can be used as the indicator of the degree of repair, an interferometer can be used to monitor the reflected phase from defects during the electron beam treatment process.

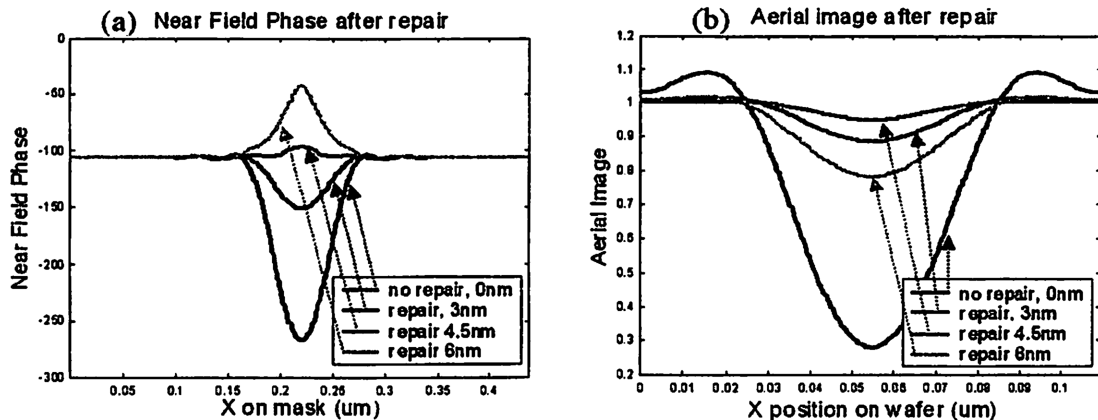

Figure 3-12. (a) Near field phase and (b) aerial images of phase defects after several amounts of e-beam treatment.

3.3 EUV multilayer mask patterning structures

This section will discuss various EUV mask patterning structures on the top the multilayer structure which is used as the mask blank. First, the process flow and resulted geometry profiles of these mask patterning structures will be described, and then the electromagnetic diffraction from these mask patterning structures will be discussed respectively [19-20]. Further discussion on their lithography imaging performance will be presented in the next chapter.

The EUV masks are usually composed of a patterned absorber layer and a buffer layer on the top of the reflective Mo/Si multilayer film deposited on a super-polished, low-thermal-expansion-material (LTEM) substrate. The pattern in the absorber layer represents the dark region of the database layout as EUV is absorbed there rather then re-

flected by the multilayer blank. This kind of EUV masks is referenced as multilayer mask with absorber stack as shown in Figure 3-13 (a).

As the multilayer structure in the mask blank provides high reflectivity for the imaging, it is possible to start from plain multilayer film without any absorber stack on the top and then subtractively etch the multilayer structure to form patterns. The resulted structure is called the etched multilayer mask structure as shown in Figure 3-13 (b). Because the reflective characteristics of multilayer mask, the field is bright only if the multilayer reflects light constructively. The damage of this periodic structure can cause the multiple reflections to be destroyed so that the EUV radiation is absorbed instead of reflected. It is possible to etch into the Mo/Si multilayer to leave the patterned trenches on the mask where the EUV light is either not reflected or less reflected so that the etched region appears dark. The remaining bilayers in the etched region contribute to attenuated reflectivity, and the depth of the etched trench contributes the phase shift with the round-trip optical path difference. The resultant reflectivity and phase shift can be designed to achieve different types of masks with different imaging functionalities. The simple fully

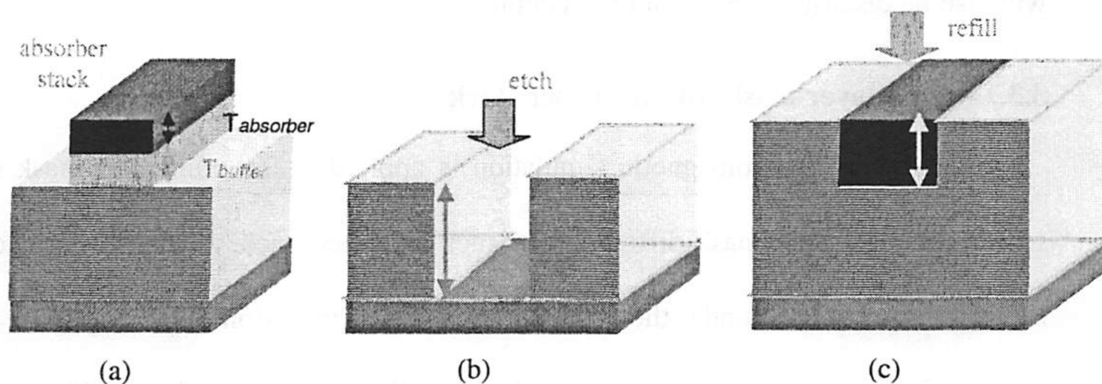

Figure 3-13. The 3D geometry of EUV mask: (a) the absorber stack on the top of planar multilayer (b) the etched multilayer binary mask (c) the refilled multilayer binary mask.

etched multilayer has a higher aerial image contrast of 99.96% than those of absorber stacks because only 0.09% light reflects off the substrate surface in the etched trench.

After the reactive ion etching in the patterning process of the etched multilayer mask, additional material can be deposited into the etched openings of multilayer masks. The mask structure resulted from above process is called the refilled multilayer mask as shown in Figure 3-13 (c). If the material has a high absorbing coefficient and the depth of openings is large enough, then the light incident on such etched and refilled regions will be absorbed and little light will be reflected back. Thus these regions will appear dark and the multilayer becomes a binary mask. The imaging contrast depends on the absorbing coefficient of the refilled material and on the refilling depth. Other kinds of imaging functionalities, such as attenuated PSM and alternating PSM, can be achieved via this scheme of etching and refilling in the multilayer structure with different choices of etching and refilling depths, refilled material properties etc.

There are also other kinds of mask structures obtained from different patterning methods, such as ion-mixed multilayer mask, and e-beam heated multilayer mask. They will also be discussed briefly in this section.

3.3.1 Multilayer mask with absorber stack

Rigorous electromagnetic simulation is applied to the multilayer mask with absorber stack to study mask diffraction of such absorber stack. A multilayer stack of 40 Mo/Si bilayers is used under the absorber stack. One dimensional line and space patterns are used in the simulation in this example. The EUV light is incident at 6° from normal and perpendicular to the line/space pattern. The near field simulation results in the ab-

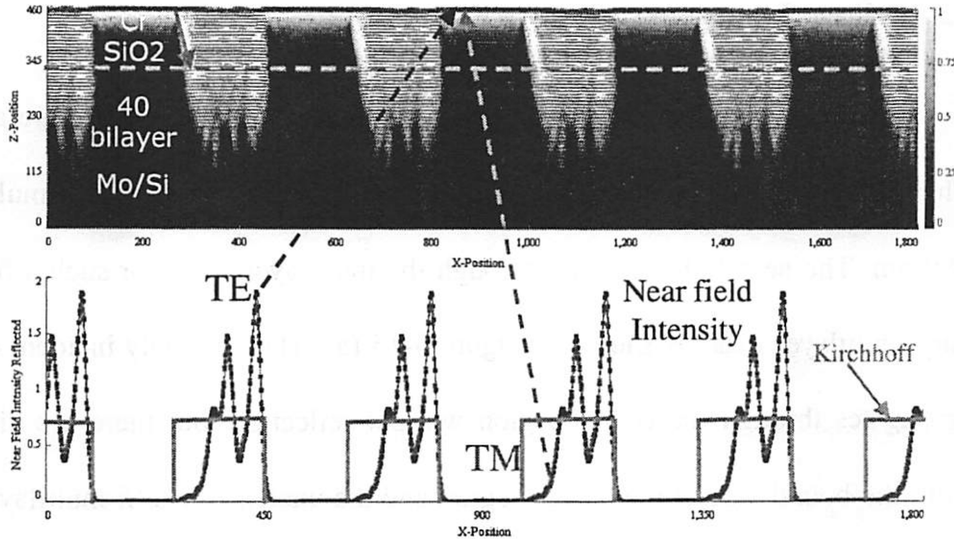

Figure 3-14. **The binary mask with absorber stacks on the top of planar multilayer: (a) E-field intensity through the domain (b) near field intensities reflected at the top.**

sorber stack and multilayer stack of this mask are shown in Figure 3-14 (a). Both incident fields and reflected fields are present so that there are standing wave patterns between absorber stacks. Figure 3-14 (b) shows the reflected field intensities taken at the output plane for both polarizations. The light is incident obliquely from the left side so that it leaves shadows at the right edge of the absorber stack where little light is reflected. On the left edge of the absorber stack, the edges of thick absorber trench tends to guide energy along a vertical path so that high electrical fields occur there and give rise to so called "edge streamers", or extreme high light intensities. While on the other edge, there is the shadow because the absorber stack absorbs EUV radiation when light incidents from top surface and passes through. This significant asymmetry is shown in the near field plot, which is also compared with a theoretic near filed from a Kirchhoff mask (thin-mask).

3.3.2 Etched multilayer mask

Similar line and space patterns on the etched multilayer mask are also simulated. The multilayer also consists of 40 Mo/Si bilayers, so the total height of multilayer stack is 280 nm. The near field intensity through the multilayer stack for such a fully etched binary multilayer mask is shown in Figure 3-15 (a). The obliquely incident electrical field propagates through the etched region without reflection, but there are diffracted fields from the boundaries of the etched region and the unetched Mo/Si multilayer region. The reflected near fields in Figure 3-15 (b) show no edge streamers and less shadow effects at edges compared with previous results from planar multilayer masks with absorber stacks. The other difference is that etched regions is dark but is lower in position, while absorber stacks are higher in position so that the shadow effects are in the opposite tone in two cases. Figure 3-15 (b) also shows the less asymmetry existing and more similarity be-

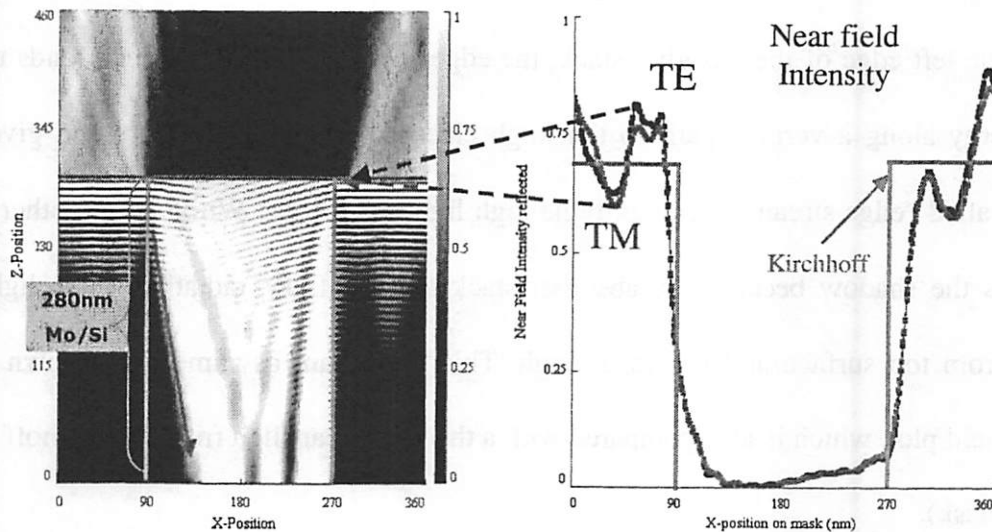

Figure 3-15. The etched binary multilayer mask: (a) E-field intensity through the domain (b) near field intensities reflected.

tween the near fields reflected from the etched binary multilayer mask and that from a Kirchhoff mask.

Besides the effect on the near field intensity, the subtractive etching in multilayer will also cause a phase change in the etched region. Figure 3-16 (a) shows the near fields intensity when only 11 top bilayers or 77 nm are etched in the center etched region and the EUV light is normal incident. Figure 3-16 (b) shows the near field phases reflected from such an etched structure. A 180° phase shift is observed between the near field reflected from the etched region and that from unetched region for both polarizations. The results from off-axis incident case also show such 180° phase shift besides the additional linear phase term due to nonzero value of *kx*.

This phase shift of the near fields is mainly due to the optical path difference of light propagation down to and up from the trench as shown by the diamond curve in Fig-

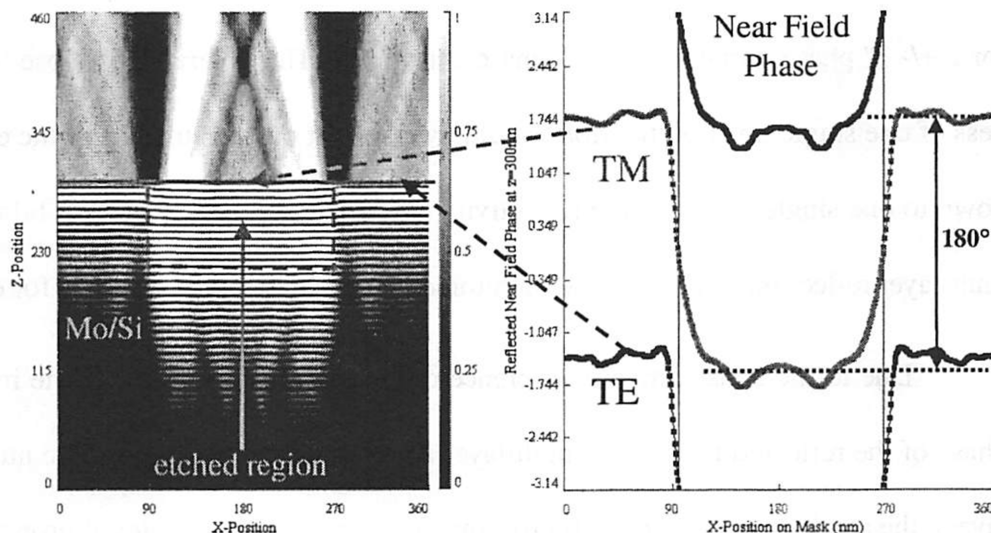

Figure 3-16. The etched phase shift multilayer mask: (a) E-field intensity through the domain (b) near field phase reflected.

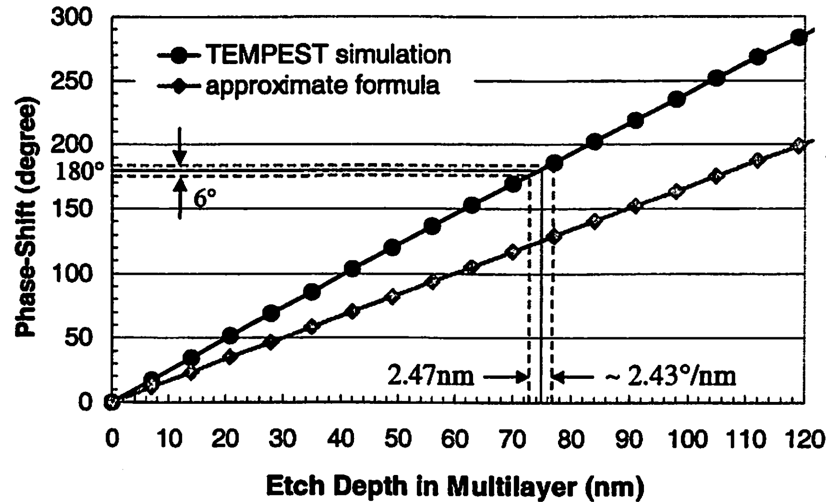

Figure 3-17. The linear relationship between the phase shift and the etched depth.

ure 3-17, which is calculated by $2*(2\pi/\lambda)*\text{etch depth}*(n_{air} - (0.6*n_{si}+0.4*n_{mo}))$. The dotted curve is the phase shift calculated from simulation. The difference between two curves is due to the reflected phase from multiple reflection of periodic structure in the multilayer. The simulation results show a linear relationship with a ratio of 2.43° phase shift per nm of the etched depth, which gives a tolerance of 2.47 nm in the etched depth for a +/- 3° phase variation at 180° phase shift point. This tolerance is close to the thickness of one single layer of the Mo/Si multilayer so that one has to control the etch process down to one single layer. As the reflectivity is sensitive on the number of bilayers during multilayer reflection, such it can be monitored and used as process control for etching.

Due to the constructive interference of the multilayer reflection, the intensity and phase of the reflected fields from multilayer are critically dependent on the number of bilayers, the single layer thickness, bilayer thickness ratio and the material properties of two materials. Thus careful design of the multilayer structure and the etched depth is needed to produce functionalities for different kinds of masks.

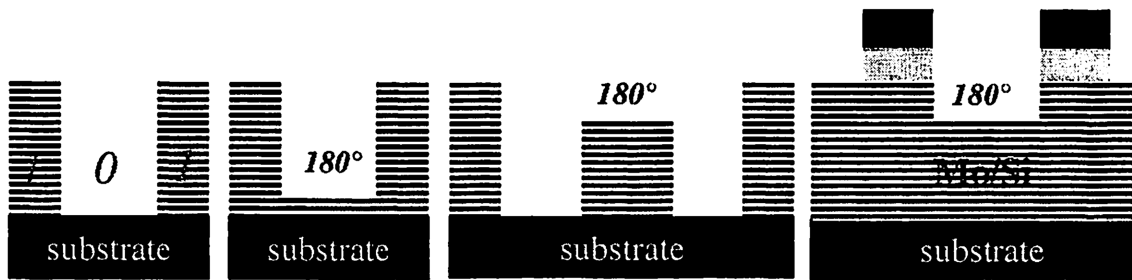

Figure 3-18. The etched multilayer structures: (a) binary mask (b) attenuated PSM (c) alternating PSM double etched (d) alternating PSM with absorber stacks.

Four possible mask structures are shown in Figure 3-18. If all Mo/Si bilayers are etched, a binary mask is produced as in Figure 3-18 (a). If the multilayer stack is etched with only 4 bilayers left and also the etched depth is about 231 nm, then the etched region has about a 6% attenuated field intensity and a 180° phase shift so that the multilayer mask becomes an attenuated PSM as shown in Figure 3-18 (b). If the etched region has about enough bilayers left for high reflectivity, then the etched region still keeps roughly the same reflectivity with the untreated region. The etched region with 77nm etch depth can be the 180° phase shift region in an alternating PSM. A double etched alternating phase shift mask can be also obtained by etching once more down to the substrate as shown in Figure 3-18 (c). It is also possible to deposit absorber stacks on the etched phase shift mask to obtain yet another type of alternating phase shift mask with absorber stacks as shown in Figure 3-18 (d).

3.3.3 Refilled multilayer mask

The refilled multilayer masks are based on a damascene process. The multilayer is first patterned and etched to certain depth required. The etching process can be a timed process via real time monitoring but the etch uniformity over large area of mask is of

concern. Another method to control the etching depth is to use a special etch stop layer in the middle of the multilayer stack, which would be made of a material with larger etch selectivity than Mo or Si [21]. This would allow good control of the etch process, which should stop at the etch stop layer. The material and thickness of this etch stop layer needs to be carefully chosen so that it will not decrease the total reflectivity of the multilayer film and yet provide good enough etch selectivity for processing.

With different choices of refilled material and depth of etching and refilling, different functionalities can be achieved using the refilled multilayer mask. If the material has a high absorbing coefficient at EUV wavelength and the refilling depth is thick enough, then the refilled material acts as the absorber so that the refilled mask becomes a binary mask as shown in Figure 3-19 (a) and 3-19 (b). If the etching depth and refilling depth is controlled well, the EUV light propagates down through the refilled material and is reflected by the underlying multilayer, and then propagates upwards and is attenuated so that a small amount of light (e.g. 6%) is reflected with a 180 degree phase-shift. The refilled mask then becomes an attenuated phase-shift mask, as shown in Figure 3-19 (c). If a less absorbing material is used for refilling, then alternating PSM or chromeless PSM

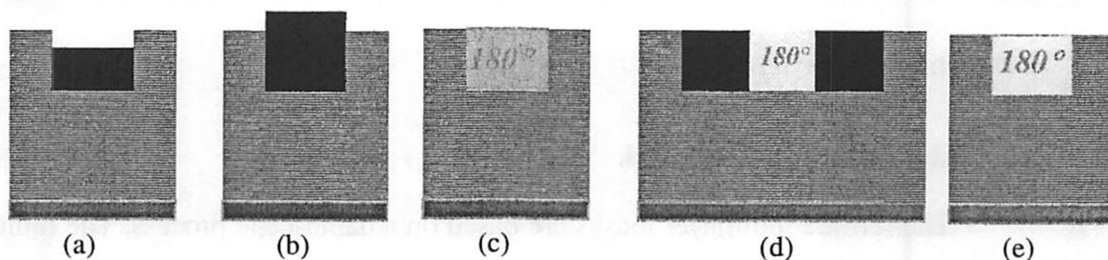

Figure 3-19. Variations in the structures and functionalities of refilled multilayer masks: (a) binary mask with refilled depth smaller than the etch depth (b) binary mask with refilled depth larger than the etch depth (c) attenuated phase-shift mask (d) alternating phase-shift mask (e) chromeless phase-shift mask.

can be obtained, as shown in Figure 3-19 (d) and (e).

The refilling process re-deposits materials into the openings etched in the multi-layer. The final profile is flat if the refilling depth is equal to the etching depth. The total reflection from this refilled region depends on the real and imaginary parts of refractive index of the refilled material and the refilling depth. This reflection contributes to the reduction of mask contrast and thus the imaging contrast. The effect of this reflection on the imaging is shown in Figure 3-20 (a), which plots the dependence of measured CD on the refilling depth for nominal 32 nm dense line and space patterns. The refilling depth is assumed to be equal to the etching depth and they vary together from 0 nm to 175 nm. The refilled material is assumed to be chrome. The data shows that 70 nm of chrome is enough to provide good contrast (99.3%) and small CD variation with the etching depth.

When the refilling depth is smaller or larger than the etching depth, a non-flat top surface is created in the refilling process. This non-planar geometry will affect the imag-

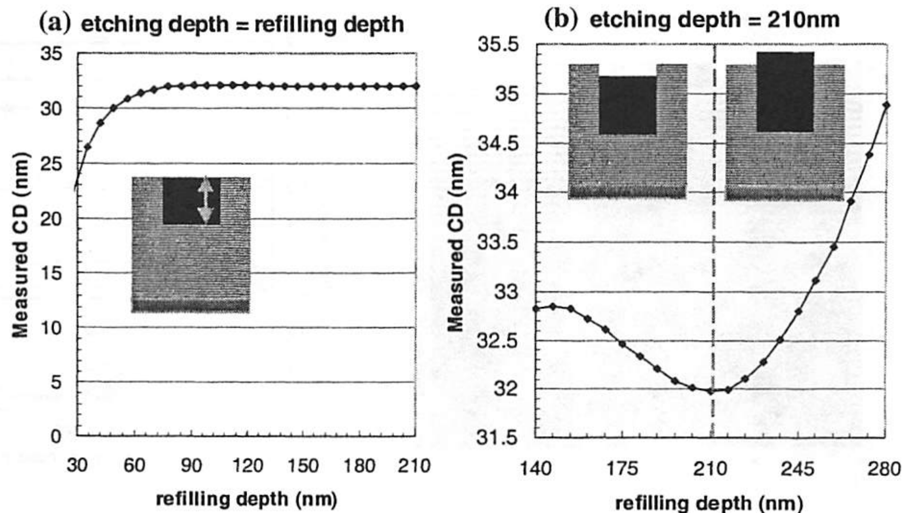

Figure 3-20. (a) CD obtained for different etched and refilled depth when they are equal (b) CD obtained for different refilled thickness when the multilayer is etched 210 nm deep.

ing. When the refilling depth is smaller, the small reflection from the top surface of the refilled opening will interfere with the reflection from multilayer top surface such that a small variation of line width is observed. When the refilling depth is larger, the refilled material acts like the absorber stack so that it causes a larger CD variation due to the shadowing effect besides the interference. As shown in Figure 3-20 (b), the line width increases when the refilling depth deviates from the etching depth 210 nm. A refilling depth larger than the etching depth has larger effects on CD than a refilling depth that is smaller than the etching depth.

The planar geometry of refilled multilayer masks has the benefits of avoiding large shadowing effects due to the oblique incidence of EUV light. It is even better than etched multilayer binary mask which still has a small optical thickness. But the existence of an absorbing refilled material may cause an interference effect due to the refilling depth variation. Figure 3-21 (a) shows the whole near field in the refilled multilayer mask

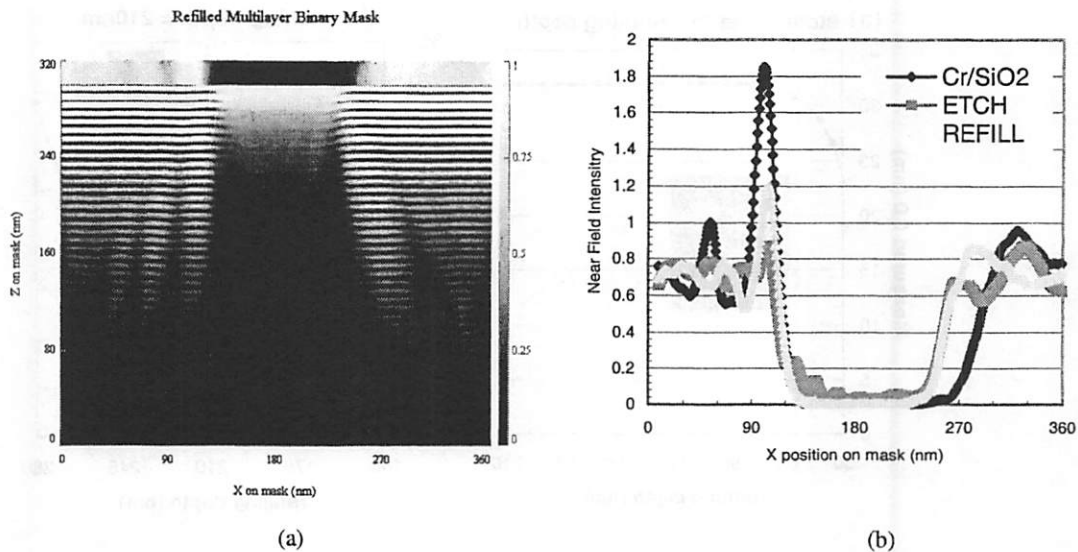

(a) (b)

Figure 3-21. The refilled multilayer binary mask: (a) E-field intensity through the domain (b) near field intensities reflected at the top compared with that of etched multilayer binary mask.

structure. Figure 3-21 (b) shows the near fields at the output plane for all three masks. The near field of refilled multilayer mask follows that of etched multilayer mask but differs only at the edges where it is more similar to that of Cr/SiO_2 absorber mask. The refilled multilayer mask has a higher intensity at the left edge due to the reflection at the left edge of refilled material, which is the same but weaker 'edge streamer' effect as in the Cr/SiO_2 absorber mask. It also has a higher intensity at the right edge than the etched multilayer binary mask because the lower refractive index of the refill material allows more light incident into the middle of multilayer at the right side instead of reflected in the etched multilayer case. Both refilled and etched mask near fields show much less shadowing at the right edge than that of Cr/SiO_2 absorber masks so that they will result in better images, in terms of H-V bias and IPE.

3.3.4 Ion-mixed multilayer mask

It is also possible to create the designed layout pattern on the mask by ion-mixing [22] as shown in Figure 3-22 (a). Don Tennant at Bell labs previously worked on such an approach. When the multilayer structure is bombarded by focused ion beams, the energetic ions penetrate the multilayer structure and mix the Si and Mo atoms so that the re-

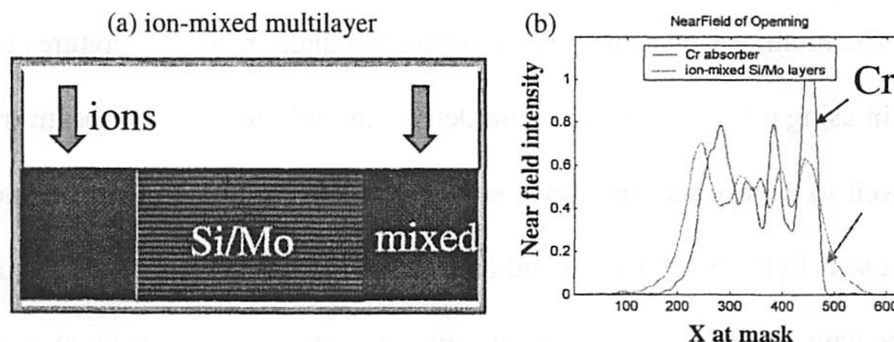

Figure 3-22. Ion-mixed multilayer mask: (a) geometry (b) near field intensity.

sulted mixture will no longer have the layer structure to Bragg reflect incident light. Therefore, this ion-mixed region can behave as the dark patterns on the multilayer masks. The process of ion beam mixing is very complicated so that the resulted ion-mixed regions usually encroach into to untreated regions. For simplicity, it is assumed that the ion-mixing causes straight boundaries between ion-mixed regions and untreated regions, and that the mixture materials in the ion-mixed region have the uniform average refractive index of 0.9690542 – j*0.003580612.

TEMPEST simulations are made for 6° off-axis illumination on the ion-mixed mask and the Cr absorber mask with the same line/space pattern. The near field intensities reflected from both masks are shown as in Figure 3-22 (b). The edges of thick absorber trench tends to guide energy along a vertical path so that high electrical fields occur there and give rise to so called "edge streamers" in the near field for Cr absorber mask case. The ion-mixing case does not have such high streamers but rather has broader fields, which also results a broader width of aerial images. If considering the encroachment of ion-mixed regions into reflective multilayer, the fields would be less broadened but the aerial image would be less sharp due to degradation of contrast.

3.3.5 E-beam heated multilayer mask

The multilayer structure can be contracted under high temperatures as shown previously in using e-beam to repair phase defects in multilayer. This e-beam treatment works very well to change the multilayer structure to optimize the amplitude and phase of reflected near field above defects and obtain minimum impact on imaging. The phase shift regions with specified amplitudes in multilayer mask blank can be also created directly

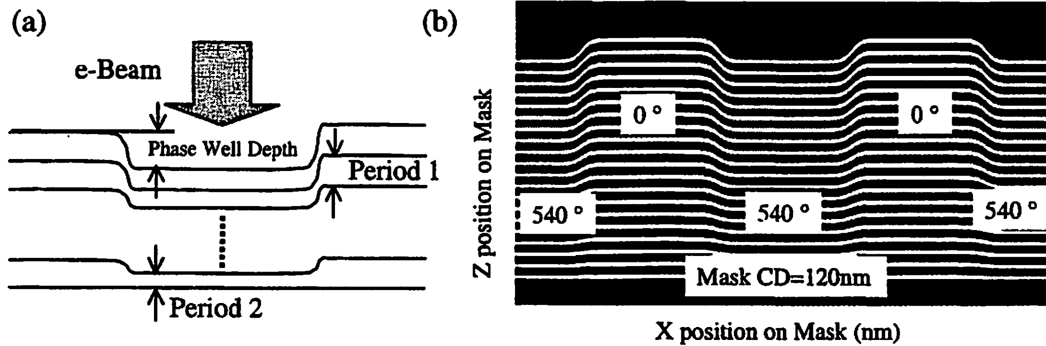

Figure 3-23. (a) The sketch of phase well created by e-beam treatment and (b) the geometry of example attPSM in multilayer.

using this e-beam treatment method [18]. Here we consider the multilayer phase well created by e-beam treatment as shown in Figure 3-23 (a). The depth of phase well is equal to the product of the number of bi-layers and the difference between the periods in the treated and untreated regions. Again the geometrical modeling is assumed including the uniform contraction of multilayer structure. For example, Figure 3-23 (b) shows the cross section of the geometry of an attenuated phase-shifted multilayer mask with phase well region of amplitude (6%) and phase shift (540°) by e-beam treatment.

For the case of 20 Mo/Si bi-layers in the multilayer, the amplitude and phase of the reflected near field are analytically calculated, and they are plotted in Figure 3-24. Figure 3-24 (a) shows the dependence of the multilayer reflectivity on the multilayer period. At the nominal multilayer period 6.938 nm in the untreated region, the reflectivity is about 0.6112. Figure 3-24 (b) shows the dependence of the phase shift on the multilayer period. The phase shift of this phase well structure is defined as the phase difference between phases of near field reflected from the treated and untreated regions. Figure 3-24 (b) shows that the phase shift obtained is always smaller than optical path difference (OPD) of the depth of the phase well. At the period of 6.683 nm and 6.312 nm, the phase shifts

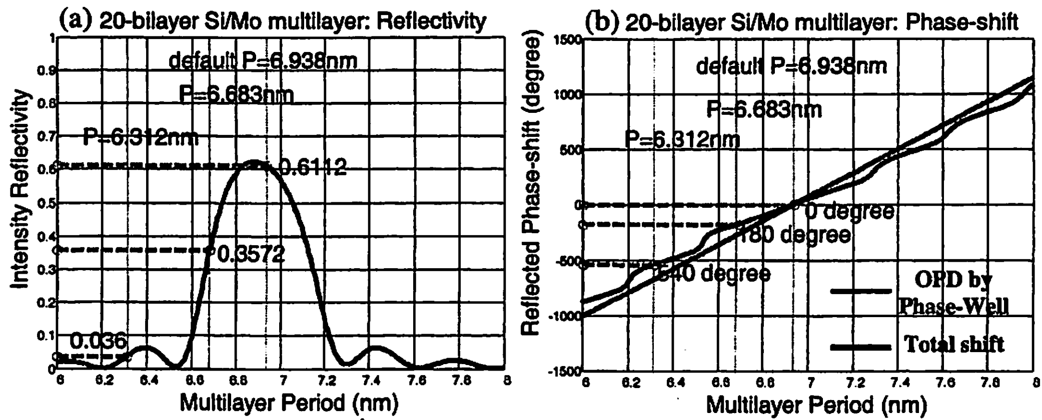

Figure 3-24. (a) Near field amplitude and (b) phase reflected from the 20 bi-layer Mo/Si multilayer.

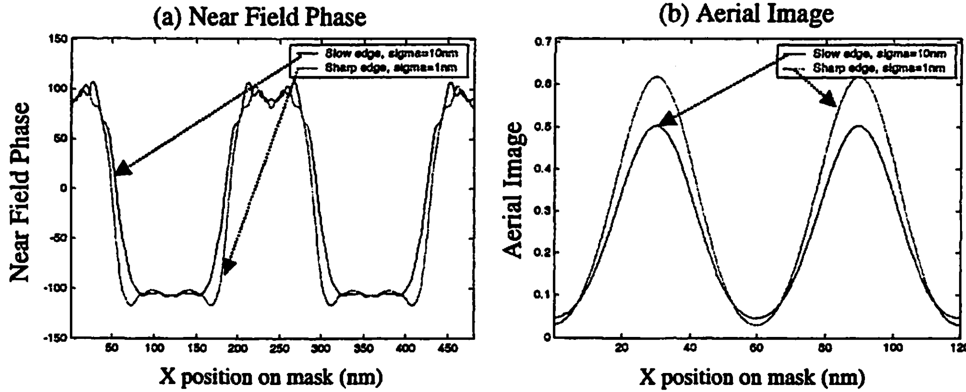

Figure 3-25. (a) Near field phase and (b) aerial images of attPSM structures.

are 180° and 540° respectively. The reflectivity at these two periods is 0.3572 and 0.0036 respectively from Figure 3-24 (a). Thus if the period of the multilayer in the phase well is 6.312 nm, a π phase shifted region with 0.0036/0.6112 or 6% of the normal clear field intensity is obtained. Using the data in Figure 3-24 or similar curves of reflectivity and phase shift *.vs.* the multilayer period for other numbers of bi-layers, one can design other configurations of given amplitudes and phase shifts for phase shift masks.

The attenuated phase-shifted multilayer mask shown in Figure 3-23 (b) has the above configuration of amplitude (6%) and phase shift (540°). Both e-beam treated and

untreated regions have lateral dimension of 120 nm on the mask. The edge between these two regions is described by an erfc function with sigma of 10 nm. This attPSM structure and a similar structure with sharper edges (erfc sigma = 1 nm) are simulated using TEMPEST.

Figure 3-25 (a) shows the near field phase reflected from two attPSM structures. They show the π phase difference between the treated and untreated regions clearly. Figure 3-25 (b) shows the aerial image at 4X of two attPSM structures. Comparison of aerial images of two cases shows that the image intensity is significantly degraded when erfc sigma increase from 1 nm to 10 nm, which also means that the transition between two regions is about 20% of their length. Thus to obtain the high performance with this type of attPSM, an e-beam system capable of much localized heating is necessary.

3.4 Conclusions

In this chapter, EUV Lithography is introduced and the EUV multilayer mask structures are modeled with rigorous electromagnetic simulations.

In the first part of the chapter, the buried multilayer substrate defects are modeled with TEMPEST simulation and Gullikson's analytical model for Gaussian substrate defect printability is analyzed. Three underline assumptions in the analytical model are tested for their scope of validity when compared with simulation results. Multilayer roughness is shown to play a second order role in defect printability. These rigorous electromagnetic simulation results also build an empirical model for substrate defect printability which covers the most interested range of defect heights and widths. This model helps greatly when making multilayer mask blank defect specifications. The further simu-

lation results on multilayer substrate defects repaired by e-beam show this defect repair method is able to recover multilayer almost without image degradation to the substrate defects when the repair process is appropriately controlled.

The second part of this chapter presents various innovative techniques for EUV multilayer masks patterning. Mask diffraction for these new multilayer mask structures are also modeled with rigorous electromagnetic simulations, and they are compared with the results from the normal multilayer with absorber stacks. From the detailed analysis of these simulation results, physical insights are obtained on how each multilayer mask structures impacts their imaging quality. The detailed analysis of advantages and disadvantages of these new mask patterning techniques is presented in the next chapter.

3.5 References

[1] G. D. Kubiak and D. R. Kania, eds, *Extreme Ultraviolet Lithography,* OSA Trends in Optics and Photonics, Vol. 4 (Optical Society of America, Washington, DC 1996).

[2] D. Attwood, *Soft X-rays and Extreme Ultraviolet Radiation: Principles and Applications* (Cambridge University Press, 1999).

[3] C. Gwyn, "EUV LLC Program Status and Plans", the first EUVL Workshop in Tokyo, May 23 (2001).

[4] T. Ogawa, T. Shoki, "EUVL Mask Development: The Current Status", the first EUVL Workshop in Tokyo, May 23 (2001).

[5] S. D. Hector, "EUVL Masks: Requirements and Potential Solutions", *Emerging Lithographic Technologies VI, SPIE Proceedings,* Vol. 4688, ed. Roxann Engelstad, pp. 134-149 (2002).

[6] S. D. Hector, P. Kearney, C. Montcalm, J. Folta, C. Walton, W. Tong, J. Taylor, P. Y. Yan and C. Gwyn, "Predictive model of the cost of extreme ultraviolet lithography masks", 20th Annual SPIE Symposium on Photomask Technology and Management, *SPIE Proceedings*, vol. 4186, pp. 733-48 (2000).

[7] P. B. Mirkarimi, D. G. Sterns *et al.*, "Investigating the Growth of Localized Defects in Thin-film using Gold Nanospheres", *Appl. Phys. Lett.* **77**, 2243 (2000).

[8] M. Brukman, Y. Deng, A.R. Neureuther, "Simulation of EUV Multi-layer Mirror Buried Defects", *Proc. of SPIE, Emerging Lithographic Technologies IV*, vol. 3997, pp. 799-806 (2000).

[9] E. M. Gullikson, C. Cerjan, D. G. Stearns, P. B. Mirkarimi, D. W. Sweeney, "Practical Approach for Modeling Extreme Ultraviolet Lithography Mask Defects", *J. Vac. Sci. Technol.* B 20(1), 81 Jan/Feb (2002).

[10] Y. Deng, T. Pistor, A.R. Neureuther, "Models for characterizing the printability of buried EUV defects", *Proc. of SPIE, Emerging Lithographic Technologies IV*, vol. 4343, pp. 551-558 (2001).

[11] D. A. Tichenor *et al.*, *Proc. SPIE*, vol. 3997, pp. 48-69 (2000).

[12] N.A. Beaudry, T.D. Milster, *Proc. SPIE*, vol. 3676, pp. 653-662 (1999).

[13] Eric Gullikson *et al.*, *Proc. SPIE*, vol. 3676, pp. 717-723 (1999).

[14] Y. Deng, T. Pistor, and A. R. Neureuther, "Effects of Multilayer Mask Roughness on EUV Lithography", J. Vac. Sci. Technol. B 20(1), pp. 344-349, Jan/Feb (2002).

[15] A. Barty, Paul B Mirkarimi, Daniel G. Stearns, Donald W. Sweeney, Henry N. Chapman, W. Miles Clift, Scott D. Hector, Moonsuk Yi, "EUVL mask blank repair", *Emerging Lithographic Technologies VI, Proc. SPIE*, vol. 4688, pp. 385-394 (2002).

[16] T. Liang, A. Stivers, R. Livengood, P.Y. Yan, G. Zhang, and F.C. Lo, "Progress in extreme ultraviolet mask repair using a focused ion beam", *J. Vac. Sci. Technol.* B 18(6), pp. 3216-3220, Nov/Dec (2000).

[17] P. B. Mirkarimi, D.G. Stearns, S. Baker, J. Elmer, D. Sweeney, and E. Gullikson, “Method of repairing Mo/Si Multilayer Thin Film Phase Defects in Reticles for Extreme Ultraviolet Lithography”, *J. Appl. Phys.* 91(1), 81 (2002).

[18] Y. Deng, B. L. Fontaine, A. R. Neureuther, “Performance of repaired defects and att-PSM in EUV multilayer masks”, the 22nd Annual BACUS Symposium on Photomask Technology,. Proc. SPIE, vol. 4889, pp. 418-425 (2002).

[19] Y. Deng, B. L. Fontaine, H. J. Levinson, A. R. Neureuther, “Rigorous EM simulation of the influence of the structure of mask patterns on EUVL imaging”, *Proc. SPIE*, vol. 5037, pp. 302-313, Jun (2003).

[20] Y. Deng, B. L. Fontaine, A. R. Pawloski, A. R. Neureuther, “Simulation of fine structures and defects in EUV etched multilayer masks”, *Proc. SPIE*, vol 5374, pp. 760-769, May (2004).

[21] S. I. Han, E. Weisbrod, Q. Xie, P. J. Mangat, S. D. Hector, W. J. Dauksher, “Design and method of fabricating phase-shift masks for extreme-ultraviolet lithography by partial etching into the EUV multilayer mirror”, *Proc. SPIE*, vol. 5037-41, pp. 314-330 (2003)

[22] Y. Deng, A. R. Neureuther, "EUV Phase-shifting Masks and Aberration Monitors", *Proc. SPIE*, vol. 4688, pp. 495-502 (2002)

[23] E. Spiller, S. L. Baker, P. B. Mirkarimi, V. Sperry, E. M. Gullikson, D. G. Stearns, *High-Performance Mo-Si Multilayer Coatings for Extreme-Ultraviolet Lithography by Ion-Beam Deposition*, Applied Optics, Vol. 42, Issue 19, pp. 4049-4058, July (2003)

[24] S. P. Hau-Riege, A. Barty, P. B. Mirkarimi, D. G. Stearns, H. N. Chapman, D. W. Sweeney, W. Miles Clift, E. Gullikson, M.-S. Yi, *Defect repair for extreme-ultraviolet lithography (EUVL) mask blanks*, Proc. SPIE, Vol. 5037, pp. 331-338 (2003).

4 Modeling Effects of EUV Masks on Lithographic Performance

4.1 Introduction

Physical model based simulation tools play a important role in early assessment and development of EUV Lithography [1-10], as in this chapter, rigorous electromagnetic simulations with TEMPEST are applied to analyze and assess the imaging performance of new EUV mask structures [11-14].

The imaging of EUV Lithography is different from the usaul DUV Lithogaphy in many ways due to the root cause of very different materials properties in EUV wavelegnth than in DUV wavelengths. The resulted major differences in imaging formation include:

(1) EUV masks are reflective instead of transmissive, so that EUV masks have to be illuminated in oblique incidence rather than the usual normal incidence in DUV lithography.

(2) The use of multilayer reflectors in all components in the optical system limits the size of lens or numerical aperture obtainable while meeting the exterme requirements on surface polish.

(3) Physical dimensions of EUV maks are not reduced as aggressive as the change of wavelegnth from EUV to DUV, so that relatively EUV mask patterns appear to

have large lateral dimensions than those new aggressive designs in high NA DUV imaging. This would reduce the optical interactions between neigboring patterns in mask diffraction.

(4) EUV mask stack have relatively larger thickness because thicker absorbers are needed due to the lower absorbing coefficients at this wavelength. Thus there is more scattering of EUV light in mask diffraction.

These new conditions exhibit many new and interesting electromagnetic phenomena in mask diffraction, which generates different near-field distributions. Hence EUV imaging formation at the wafer is also affected and exhibit different properties than that in DUV Lithography.

This chapter will first examine the lithography imaging performance of various mask patterning structures. Process window and other imaging properties of these mask structures are compared. Advantages and disadvantages of these mask stacks are discussed. The second part of chapter focuses on effects of non-ideal mask geomety on the imaging formation, such as defects and sidewall profiles. Espeically the patterning defects in the refilled multilayer masks are discussed and a defect repair scheme is proposed.

4.2 EUV multilayer mask imaging performance

In this section, three EUV mask patterning structures are examined via rigorous electromagnetic simulation with TEMPEST. These structures includes multilayer masks with absorber stack, etched multilayer binary masks, and refilled multilayer binary masks, whose mask diffraction are discussed in the last chapter.

In the past few years, various absorber stacks have been investigated [15-18]. Based on these recent developments, three kinds of absorber stacks are selected in the simulations of this chapter: Cr/SiO_2, TaN/SiO_2, and TaBN/Cr. The detailed characteristics of these structures are displayed in Table 4-1. Due to the interference between the reflection from absorber top surface and that from multilayer boundary, the reflection coefficient from such mask stack oscillates with absorber thickness. Considering the possible variations in the patterned absorber thickness, the absorber stack thicknesses are selected to have similar transmission and averaged reflection over small range around the nominal thickness so that they provides similar aerial image contrasts for comparison. Even with the large thickness of these absorber stacks, they still have less image contrast comparable to the desired 99.9% contrast of DUV photomasks.

Absorber	Absorber thickness (nm)	Buffer layer	Buffer layer thickness (nm)	Total height of absorber stack (nm)	Transmission of the stack (%)	Aerial image contrast (%)
Cr	70	SiO_2	80	150	0.13	98.55
TaN	60	SiO_2	80	140	0.15	99.21
TaBN	50	Cr	50	100	0.05	99.64

Table 4-1. The properties of three absorber stacks.

The etched multilayer mask used in this imaging performance comparison is a fully etched multilayer binary mask with 40 Mo/Si bilayers, which are the same for the multilayer used in absorber stack masks. Thus the total pattern stack thickness is 280 nm. The image contrast from such etched multilayer binary mask is 99.96%, which is better

than image contrasts of three absorber stacks. The refilled multilayer mask also has the same multilayer stack of 40 Mo/Si bilayers. Out of 280 nm total stack thickness, 30 bilayers of 210 nm are etched and all of them are refilled with Cr. So the final multilayer surface is assumed to be flat as shown in Figure 3-20.

TEMPEST is used to model the ecltromagnetic scattering process through these multilayer mask stacks. Simulation conditions are the same as those in Section 3.2.1. Aerial image calculation is carried out via a vector diffraction model. No resist model is considered so that the images compared are all aerial images. Refractive index of all materials used in the simulations of this chapter are obtained from CXRO website [19] and tabled as following:

Material	n	k
Silicon	0.999931	0.00182108
Molybdenum	0.922739	0.00621991
Chrome	0.933328	0.0381974
SiO_2	0.9787098	0.0105698
Carbon	0.962145	0.00674678
Yttrium	0.97423	0.00226462

Table 4-2. Refractive indices of all materials at EUV wavelegnth (13.4 nm)

4.2.1 CD variation with mask stack thickness variation

For the EUV masks with absorber stacks, it was found by K. Toh [5] that the line width could be significantly affected by small changes in the absorber stack thickness. It is due to the first interference between the field reflected from the multilayer surface and the small field reflected at the top of absorber surface, and the second interference between the field reflected from the multilayer surface and the small field, which penetrates

down through the absorber stack and reflects back from the buffer layer and the multi-layer. For the selected absorber stacks with large thickness, the second interference is damped due to absorption in the absorber stacks. These effects are studied by rigorous simulations of 45 nm dense line feature under several simulation conditions and for different absorber stacks.

Figure 4-1 (a) shows the periodic line width variations with the Cr thickness for the Cr/SiO_2 absorber stack under different simulation conditions. The dot curve shows the simulation results under monochromic EUV light λ = 13.4 nm and one rigorous electromagnetic simulation for one oblique incident angle θ = 6°. The rectangle curve shows the simulation results with 21 wavelengths in the total +/- 1% EUV bandwidth window. The increased number of EUV wavelengths applied in simulations decreases the amount of line width variations from 2 nm to 1.1 nm. The upper-triangle curve shows the simulation results with 15 rigorous electromagnetic simulations for 15 angles from 3°~9° respectively. The resulted line width variations are still about 2.4 nm. These curves all have the periods of about 6.7 nm, which is the half the EUV wavelength. This line width variation

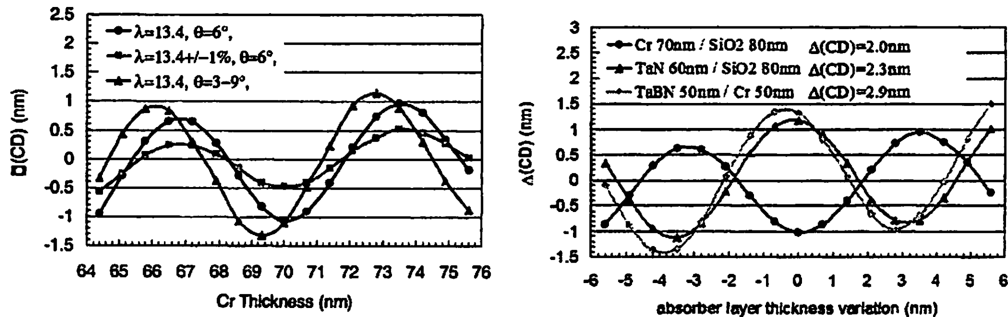

Figure 4-1. The line width variation of 45 nm line space features: (a) for Cr/SiO_2 absorber stacks (b) for different absorber stacks.

in small range of absorber thickness change is due to the first interference effect. Figure 4-1 (b) shows the line width variations when the absorber thickness changes from the nominal thickness for three absorber stacks. The line width changes are from 2 nm to 2.9 nm. The TaBN/Cr absorber stack has the largest ΔCD because it has the highest reflection coefficient.

In the etched multilayer binary mask, because the multilayer stack is fully etched, there is no variation of stack thickness. If considering the residue left over by the etching process, the effect should still be small as the Mo/Si materials left on the bottom of multilayer stack can not reflect much light out of 280nm thick trench as their interference structure is destroyed. For the refilled multilayer masks, the line width does changes as shown in Figure 3-20 if considering the thickness variation of the refilled materials. The curve of measured CD vs refilling depth in Figure 3-20 (b) is not oscillating and more like a parabolic curve so that it has a very small change at 32 nm when the refilled multilayer mask is flat.

4.2.2 Effects of sidewall profile in mask imaging

The etching process during mask patterning can cause sidewall profiles in the mask structures. The robustness of process window with respect to variation of sidewall profiles is important. Both positive and negative sidewall angle cases are simulated and samples of near fields for three multilayer mask stacks are shown in Figure 4-2 (a). The negative sidewalls generally allow more light absorbed by absorber or transmitted to substrate and thus there are less light reflected. This will result in a higher image contrast and a slightly wider line printed. On the contrary, the positive sidewalls reflected more light

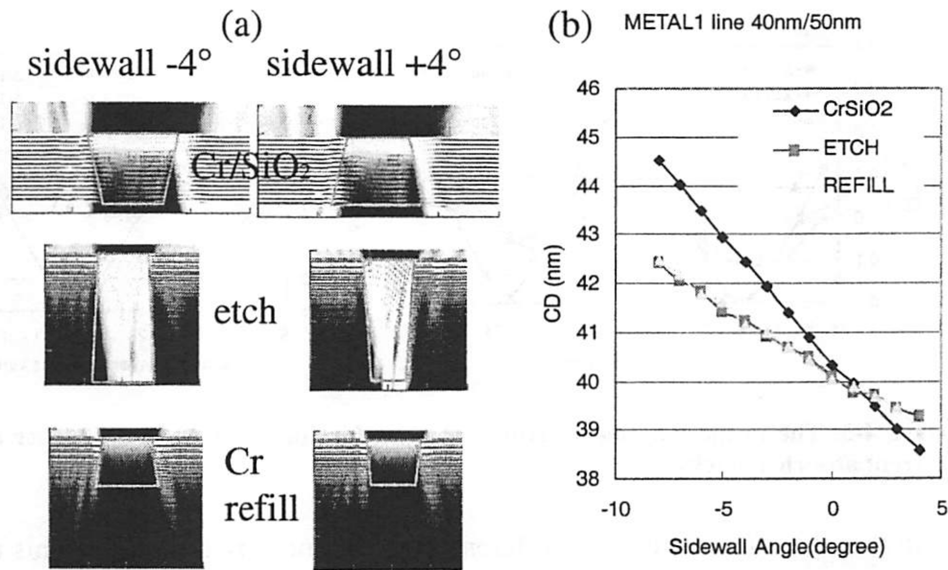

Figure 4-2. (a) Near fields for three types of masks with negative and positive sidewall angles (b) Measured CD dependence on sidewall angle of METAL1 masks.

and result in a narrower line printed. Figure 4-2 (b) shows the measured CD for three types of masks when sidewall angle is changed. All three curves have larger CDs at negative sidewalls and smaller CDs at positive sidewalls. The curve of Cr/SiO_2 absorber mask has larger slope about twice of those for etched and refilled multilayer masks as expected due to the larger shadowing effect of thick Cr/SiO_2 absorber.

The effects of sidewall profiles on the process windows of three multilayer mask stacks are also discussed in later section.

4.2.3 Image placement error (IPE) and H-V bias

Due to the oblique incident of EUV light, the image position of horizontal line is shifted relative to the feature position on the mask [20]. This position shift is called image placement error (IPE). For vertical lines, the light is incident parallel to the line edges so that there is no shift in the image position. Also the vertical line does not have the shad-

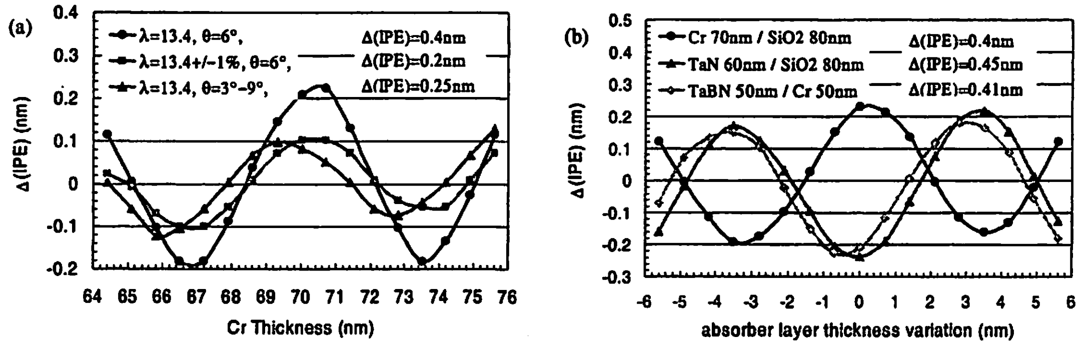

Figure 4-3. The image placement error variations for: (a) for Cr/SiO_2 absorber stacks (b) for different absorber stacks

ows so that the effective dose is different from that of horizontal line. This results different line widths at the same exposure dose for horizontal lines and vertical lines. This line width difference is called H-V bias. Rigorous 3D simulations of horizontal and vertical lines are used to study this H-V bias and the image shift IPE for three absorber stack masks, the etched binary multilayer mask and refilled multilayer mask.

For the multilayer masks with absorber stacks, the absorber thickness change will also change IPE due to the same the interference effects. Figure 4-3 (a) shows the periodic changes of IPE with the Cr thickness for the Cr/SiO_2 absorber stack under three

EUV Mask Stack	Stack Thickness (nm)	H-V Bias (nm)	Image Placement Error (nm)
TaBN 50nm / Cr 50nm	100	3.1	4.6
TaN 60nm / SiO2 80nm	140	5.1	5.9
Cr 70nm / SiO2 80nm	150	5.9	6.6
Etched Multilayer Binary Mask	280	-2.4	1.5
Refilled Multilayer Binary Mask	210	-2.1	1.2

Table 4-3. The imaging properties for different EUV mask stacks.

simulation conditions. The range of IPE change is about 5 times smaller than the line width variations. Not only more wavelengths but also more angles used in simulations decrease the IPE change. Figure 4-3 (b) shows the IPE changes for three absorber stacks. The total line width changes are about 0.4 nm range.

Table 4-3 summarizes the simulation results. The results of absorber stacks show that the H-V bias and IPE are almost linearly depended on the thickness of absorber stack because of the geometrical shadowing effects. Also the interference causes a 2nm variation on the line width while it produces only a 0.4 nm range of variation on the IPE. The effect of interference on H-V bias is smaller considering it also causes line width variations for the vertical lines. The shadowing effects are also depended on the absorption efficient of the absorber stack. With the same absorber stack thickness, the more absorbing stack has larger shadowing effects than the less absorbing stack. But usually the more absorbing stack has smaller thickness for the same image contrast so that it effectively has less shadowing effects.

The etched binary multilayer mask shows much less H-V bias and IPE even though the etched depth of multilayer is 280nm large. This is because the EUV light is reflected at the top surfaces of multilayer rather than at the bottom of trenches in the absorber stacks. If the reflection of multilayer is modeled as that of a single reflection surface, this surface is positioned about 35 nm below the top surface of the multilayer. This 35 nm effective thickness of the multilayer contributes to the much smaller shadowing effects in H-V bias and IPE of the etched binary multilayer mask than those of absorber stack masks. The refilled multilayer binary mask has similar results of etched binary

masks, as their structures are very close actually with only difference in the refilled absorber, which helps a little bit in absorbing EUV light.

To meet the CD uniformity 7 nm budget and IPE and overlay budget 18 nm for the 45 nm node in the ITRS 2002 update roadmap, the large H-V bias and IPE of the absorber stack masks require that the features on the mask should be corrected. Those of the etched or refilled binary multilayer mask are tolerable but might also need to be corrected in practice if they are adopted.

4.2.4 Process window and depth of focus

Rigorous electromagnetic simulations are applied for the above three types of EUV mask structures to compare their lithography imaging performance in terms of depth of focus. Among three absorber stacks, Cr/SiO2 absorber stack is chosen in this simulation study. The set of features simulated includes a 30 nm *POLY* line in a 90 nm pitch, a 50 nm *METAL1* space in a 90 nm pitch, and a 25 nm *ISO* line (in a 350 nm pitch in the simulation domain) at image scale for the 32 nm technology node. They are all oriented horizontally as the incident rays of EUV light are perpendicular to the line/space edges. Small mask line width variations, such as the systematic changes of mask CD bias from -10 nm to 10 nm at image plane and mask opening sidewall angle from -10° to 4°, are also applied to these mask structures.

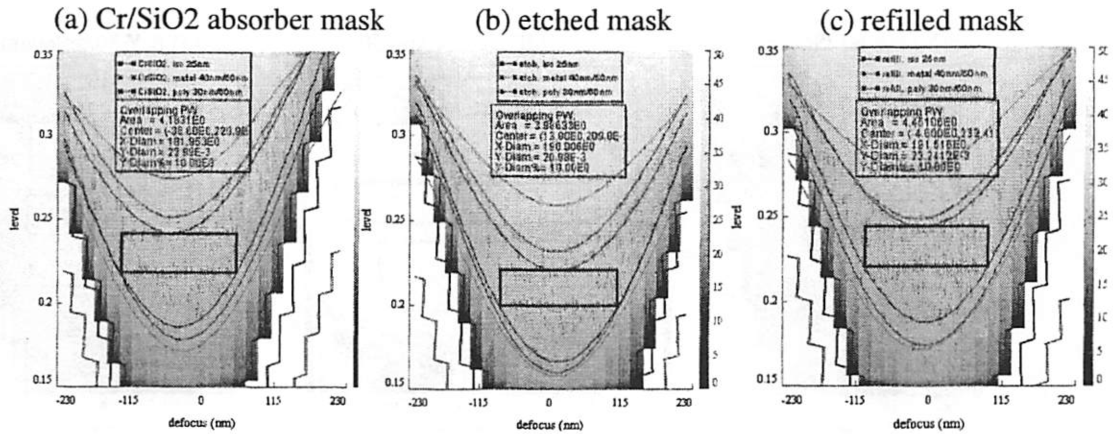

Figure 4-4. The combined process window for the set of features in (a) Cr/SiO_2 absorber mask (b) etched mask (c) refilled mask.

The combined process window for the set of features is calculated for all three types of masks. The rectangular process windows under 10% does/level variation conditions are 182 nm for Cr/SiO_2 absorber stack masks, 190 nm for etched mask, and 192 nm for refilled masks as shown in Figure 4-5. The best process window for Cr/SiO_2 absorber masks is obtained at 7 nm CD bias at the image plane for all three features. For etched and refilled multilayer masks, the best process windows are both obtained at 3 nm CD bias for ISO, 2 nm CD bias for METAL1 and POLY at the image plane. The critical feature is the ISO line as the process window is almost limited by that of ISO line as shown by the dark curves in Figure 4-4. The Cr/SiO_2 absorber masks have the smaller process window as expected due to the thick mask effect as the shadowing effect is canceled via biasing. This thick mask effect also results in the tilt of process window curves toward negative defocus as the best focus is at -36.8 nm. The etched multilayer masks have almost the same process window as that of refilled multilayer masks, though the etched multilayer masks also have a small positive best focus shift at 13.8 nm. The refilled multilayer masks have the smallest best focus shift at -4.6 nm.

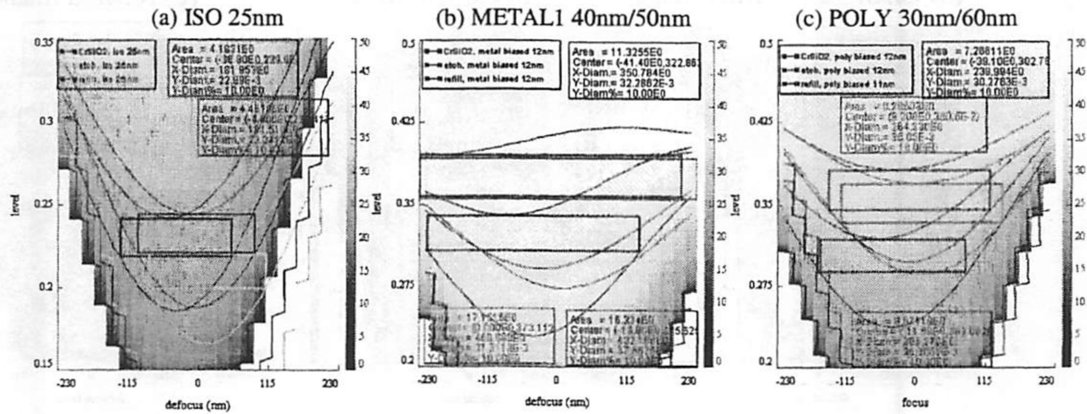

Figure 4-5. The respective process window for three mask structures: (a) ISO 25nm (b) METAL1 40nm/50nm (c) POLY 30nm/60nm.

The process windows of three mask structures are also plotted together for each individual feature as shown in Figure 4-5. These plots again clearly show that the etched and refilled binary masks have larger depth of focus especially for the limiting feature ISO 23nm line.

The effects of sidewall profiles on the process window are also analyzed via simulations for three multilayer mask structures. The same sidewall angle (-4° and -4°) are applied to each mask structure. But these simulations for masks with sidewalls are done for features with nominal CDs without biases. Thus the process windows for such features are smaller than those for biased features shown in Figure 4-4, but they follow the same trend for different types of masks.

The process window results are compared for the effects of sidewall. Considering the process window degradation under the variations of sidewall profile, the combined process window for features with 0° and -4° (or 0° and 4°) sidewall angles are calculated and compared. The sidewall with a positive angle tends to decrease line width so that an

effective CD bias is applied. Thus the combined process windows for features with 0°and 4° sidewalls is larger that those of features with 0° and -4°. These combined process windows for Cr/SiO_2 absorber masks show a 30% to 45% drop from the original process window at for features with sidewall angle 0°, while there are less than 20% decrease of process window for etched and refilled multilayer masks. This agrees with the previous results of CD variations due to the sidewall profiles in Figure 4-2 (b).

4.2.5 Experimental results

In previous sections, the etched and refilled multilayer masks have been analyzed with rigorous electromagnetic simulations. The results are compared with those of absorber stack masks and they show etched and refilled multilayer masks have significant advantages in lithography imaging performance. Some of these advantages are also observed in the experimental study when I worked as an intern at AMD.

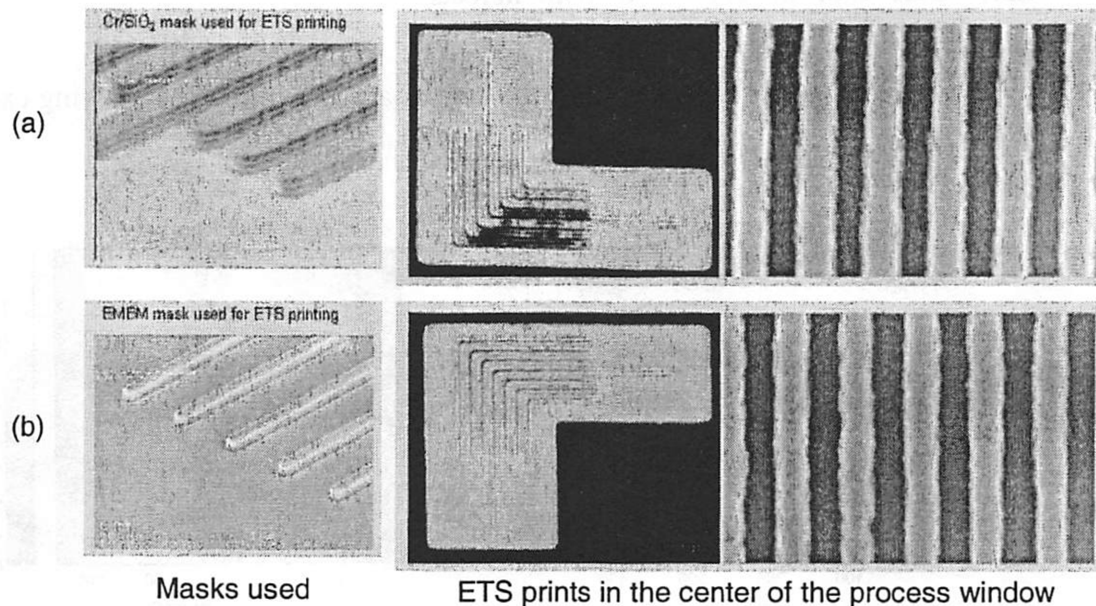

Figure 4-6. SEM images of mask used and ETS prints for (a) Cr/SiO2 absorber stack mask (b) etched multilayer binary mask. (courtesy of AMD)

Figure 4-6 shows the SEM images of both mask structures and early wafer printing results from EUV ETS. Figure 4-6 (a) clearly shows the bilayer structure of the absorber stack and the worse printing results for horizontal lines compared to vertical lines. Figure 4-6 (b) shows that both horizontal and vertical lines are printing very well at the center of process window.

4.3 Effects of defects in multilayer mask on imaging performance

In this section, defects in EUV patterned multilayer mask are discussed for their effects on imaging. First part of the section briefly discusses the effects of buried substrate defects o patterning printing with one simulation example. The second part of section discusses the patterning defects in etched and refilled multilayer masks. One new defect repair scheme is proposed and its repair performance is analyzed with simulations.

4.3.1 Effects of multilayer substrate defects

The effects of multilayer substrate defects are shown in the following example of

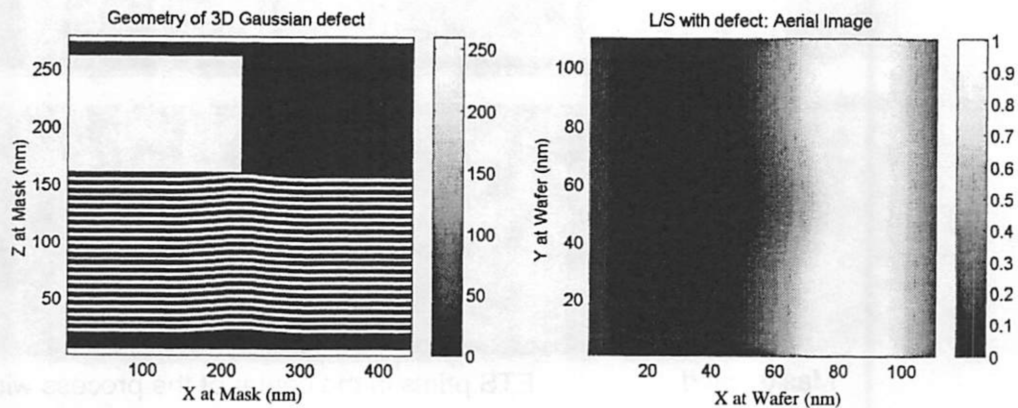

Figure 4-7. The 3D Gaussian buried substrate defect centered on the Cr edge: (a) geometry of whole mask stack (b) 2D aerial image result.

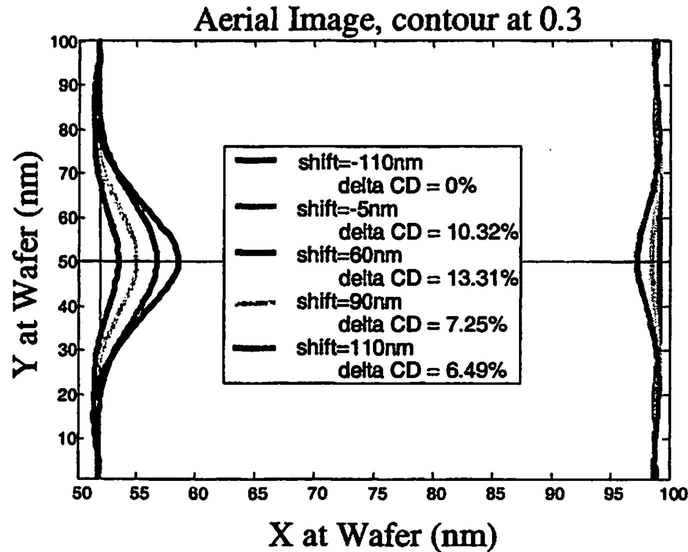

Figure 4-8. The 2D aerial image contour at 0.3 threshold for multiple defect locations.

TEMPEST simulation. A 3D Gaussian defect with sigma width of 60 nm is buried in the multilayer stack. A 55nm/55nm line and space pattern with 100 nm Cr absorber is placed on the top of the multilayer surface. Figure 4-7 (a) shows the geometry of whole mask stack when the Gaussian defect is centered on the Cr edge. The 2D aerial image result is plotted in Figure 4-7 (b). It clearly shows that the Gaussian defect reduces the light scattering in the middle of line such that the line space appears wider in the middle.

The buried Gaussian defect is shifted from under the middle of Cr absorber (x = -110 nm on mask), to almost at edge of Cr absorber (x = -5 nm), to outside absorber (x = 90 nm), and to the center of space (x = 110nm). The aerial image contours at threshold of 0.3 for these masks configurations are plotted in Figure 4-8. It clearly shown that the maximum change of line width happens at x = 60 nm, when the defect is away from the absorber edge by about 60 nm the same as the defect size.

4.3.2 Patterning defects and repair in refilled multilayer masks

Defects can occur during the patterning process such that the patterns on the mask deviate from those in the database as designed. These patterning defects do not necessarily print as significant wafer defects but they may reduce the process windows or cause CD variations.

Patterning defects on the absorber stack masks has been studied [20] and their repair can be treated in the traditional way [21]. But for the subtractive process on the multilayer stack used in etched or refilled multilayer masks, it is very hard to repair such patterning defects as they are part of multilayer stack. Special care needs to be taken to avoid the damage of the multilayer reflector structure. The voids inside multilayer stacks are even worse.

Figure 4-9 (a) shows the sketch of a void defect on the edge of etched openings. In the etched multilayer mask, the multilayer structure is missing at this defect position, while in the refilled multilayer mask, there is the absorbing material filling this additional

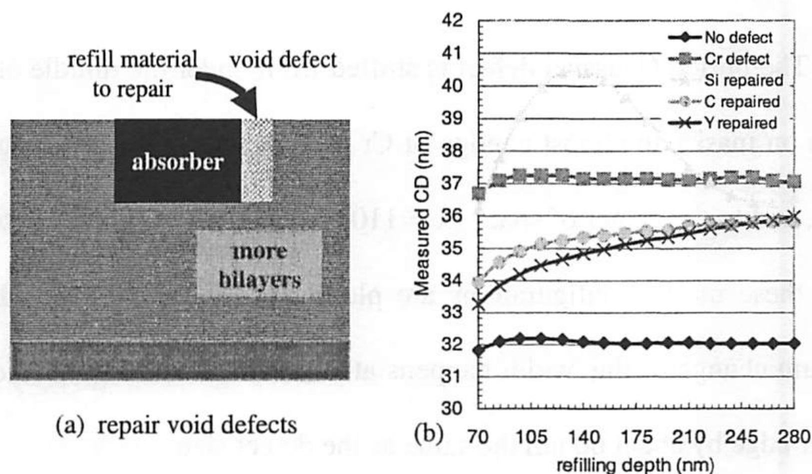

Figure 4-9. (a) Void defect in the multilayer stack (b) dependence of measured CD on the refilling depth after repaired with different materials.

space of void defect. The void defect in the etched multilayer mask cannot be repaired because that the damaged multilayer structure cannot be rebuilt in the defect position. The void defect in the refilled multilayer mask can be mitigated or repaired if there are enough bilayers left under the etched openings and a transparent material instead of the absorbing material is deposited into the defect position. The transparent material fills the space of void defect and allows light to propagate into the underlying multilayer and reflect back so that the reflected light is restored at this position.

The transparent material can be deposited into the void defect via the focused ion beam (FIB) deposition or the low damage method of focused electron beam deposition [22], so that this material must be compatible with the deposition process. Due to the fact that all materials are absorbing in EUV wavelength, there will be light attenuation through the deposited repair material. Three materials, Si, C or Y, are chosen in series of 2D simulations to study effectiveness of this defect repair scheme for a 20 nm void defect

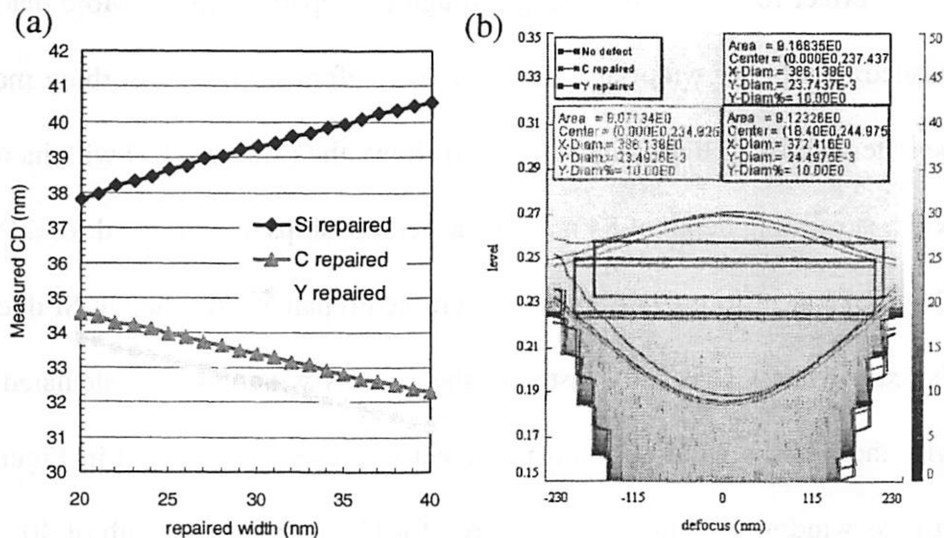

Figure 4-10. Effects of repair with different materials: (a) dependence of measured CD on refilling width after (b) Process window after repair.

on the mask with 32 nm/32nm line and space pattern at image scale. The measured CDs before and after repair are plotted in Figure 4-9 (b) against the refilling depth that is equal to the etching depth too. The size of repair material is assumed to be equal to the defect size. The blue diamond curve is the line CD without defect (~ 32 nm). The magenta square curve is the line CD with defect (~ 37 nm). The yellow upper-triangle curve is the line CD for defect repaired with Si, which oscillates and does not restore CD at all. The reason is that Si has a real part of refractive index close to 1, differing significantly from that of multilayer, so that it results in a phase shift and effectively increases the CD. C or Y has a better matched real part of refractive index but a higher imagery part so that the measured CD increases when the refilling depth increases. In the case of 70 nm refilling depth, the 5 nm CD variation is reduced to 2 nm and 1.2 nm, respectively for C and Y.

As shown in Figure 4-9 (b), the CD value is not fully restored if the repair material fills only the space of void defect in deposition due to the absorbing of light and the shadowing effect for light propagating through the repaired region. More material can be deposited to a larger width at the void defect before refilling absorbing materials to compensate the loss of light. Figure 4-10 (a) shows the measured CD with increasing of repair width at refilling depth of 84 nm. Linear relationships are observed for all three materials. C and Y can restore CD fully with increased repair width, though Si does not help. For the case when CD is fully restored, the process windows are calculated and compared with the process window when no defect is present. As plotted in Figure 4-10 (b), the process window is almost fully restored for C repair with a width of 40 nm but shows a small reduction of depth of focus for Y repair with a width of 34 nm.

4.4 Discussion and conclusions

In this chapter, the imaging properties and lithography performance of three types of EUV multilayer masks are compared via rigorous electromagnetic simulations. The etched/refilled multilayer masks seem to be superior to absorber stack masks in all aerial image properties. The subtractive process of etched/refilled multilayer masks provides a much smaller effective stack thickness which has inherent advantages over thick absorber stacks. The image quality of etched/refilled multilayer binary masks is close to that of transmission chrome-on-glass mask in DUV lithography where the Kirchhoff thin-mask model can be used, so that it reduce the needs of more complex optical modeling of EUVL mask.

The direct result of this similarity is that the etched/refilled multilayer binary mask has larger depth of focus than the multilayer masks with absorber stacks as shown in the focus exposure window plots. The second advantage of the etched/refilled binary multilayer masks is that they have a higher contrast. Third they have much less line width variation due to the interference phenomenon compared with absorber stack masks. Although the line width dependence on absorber thickness for EUVL masks with absorber stacks is reduced with increased EUV bandwidth, this variation is only reduced by about 50% even with the full 2% bandwidth of EUV illumination. So that the tight control on the absorber thickness remains as a concern for the overall CD budget.

The smaller effective stack thickness of the etched/refilled multilayer masks also results better H-V bias and IPE results also than multilayer masks with absorber stacks. This is because the reflection occurs mainly at the top layers of the multilayer film, so that

in absorber stacks, the light has to propagate down and back up on the mask openings. This additional propagation causes larger H-V bias and IPE.

There could be other advantages of the etched multilayer mask. It should have a high contrast in reflection at deep UV wavelengths and should be inspectable in transmission because the areas where the Mo/Si reflector is removed should allow light to go through the mask without much absorption while the areas where the Mo/Si multilayer remains will absorb the light, thus providing good contrast. In addition, the emissivity of the substrate, which effectively acts as the absorber for the etched-multilayer mask, is significantly higher than that of Cr or TaN, so that the effect of the EUV power incident on the masks should produce a lower temperature rise and therefore less distortion of masks.

But the patterning defects remain a concern for the etched multilayer masks. In this case, the refilled multilayer masks preserve much of the same advantages of etched multilayer masks, and improve on the defect reparability with new defect repair scheme proposed. The subtractive mask patterning technique by etching is new compared with the more developed patterning method with absorber stacks. There are still concerns such as the control of etch process, the etching quality of trench profile, and the oxidation of Mo/Si at the edges, the defect inspection and repair, which need further investigations.

In conclusion, rigorous electromagnetic simulations are very effective in modeling the new masks technologies used in EUV Lithography. These simulations provide valuable physical insights to access new techniques and also provide quantitative guidelines for new he mask developments.

4.5 References

[1] G. D. Kubiak and D. R. Kania, eds, *Extreme Ultraviolet Lithography*, OSA Trends in Optics and Photonics, Vol. 4 (Optical Society of America, Washington, DC 1996).

[2] D.M. Tennant, J.E. Bjorkholm, R.M. D'Souza, L. Eichner, R.R. Freeman, J.Z. Pastalan, L.H. Szeto, O.R. Wood II, T.E. Jewell, W.M. Mansfield, W.K. Waskiewicz, D.L. White, D.L. Windt, and A.A. MacDowell, *Reflective mask technologies and imaging results in soft x-ray projection lithography*, J. Vac. Sci. Technol. B **9** (6), pp 3176-3183 (1991)

[3] O.R. Wood, D.L. White, J.E. Bjorkholm, L.E. Fetter, D.M. Tennant, A.A. MacDowell, B. La Fontaine, and G.D. Kubiak, *Use of attenuated phase masks in extreme ultraviolet lithography,* J. Vac. Sci. Technol. B 15 (6), pp. 2448-2451 (1997)

[4] T. Pistor, K. Adam, and A. Neureuther, *Rigorous simulation of mask corner effects in extreme ultraviolet lithography*, J. Vac. Sci. Technol. B 16 (6) pp. 3449-3455 (1998)

[5] K. Toh *et al.*, *EUV Stepper Characterization using Lithography Modeling*, 2nd Annual International Workshop on Extreme Ultraviolet Lithography, Oct 16-19 (2000)

[6] Bruno La Fontaine, N. Sidarous, *EUVL Mask Patterning Studies: 3D imaging simulations of masks with different absorber stacks*, First EUV Workshop at AMD (2001).

[7] C. Krautschik, M. Ito, I. Nishiyama, and T. Mori, *Quantifying EUV Imaging Tolerances for the 70, 50, and 35 nm Nodes through Rigorous Aerial Image Simulations*, Proc. SPIE Vol. 4343, p. 524-534 (2001)

[8] A. Wolter, F.M. Kamm, and S. Wurm; *Performance of EUV masks: Simulated Influence of Mask Parameters on the EUV Process Window*, First International Symposium on Extreme Ultraviolet Lithography, Dallas, October 14-17 (2002)

[9] S.D. Hector, S.I. Han, N.V. Edwards, K. Williams, R. Gregory, P.J.S. Mangat, and K. Rosford, *Requirements for fabricating attenuated phase-shift masks for EUV lithography*, First International Symposium on Extreme Ultraviolet Lithography, Dallas, Oct. 14-17 (2002)

[10] Sang-In Han, Eric Weisbrod, Qianghua Xie, Pawitter J. Mangat, Scott D. Hector, William J. Dauksher, *Design and method of fabricating phase-shift masks for extreme-ultraviolet lithography by partial etching into the EUV multilayer mirror*, Proc. SPIE, vol. 5037-41, p.314-330 (2003)

[11] Yunfei Deng, Bruno La Fontaine, Andrew R. Neureuther, *Performance of repaired defects and attPSM in EUV multilayer masks,* 22nd Annual BACUS Symposium on Photomask Technology, Proc. SPIE, Vol. 4889, p. 418-425 (2002)

[12] Yunfei Deng, Andrew R. Neureuther, *EUV Phase-shifting Masks and Aberration Monitors,* Proc. SPIE vol. 4688 (2002).

[13] Yunfei Deng, Bruno La Fontaine, Harry J. Levinson, Andrew R. Neureuther, *Rigorous EM simulation of the influence of the structure of mask patterns on EUVL imaging*, Proc. SPIE, vol. 5037-41, p.302-313 (2003)

[14] B. M. La Fontaine, A. R. Pawloski, Y. Deng,O. R. Wood II, H. J. Levinson, C. Chovino, L. Dieu, *Architectural choices for EUV lithography masks: patterned absorbers and patterned reflectors*, Proc. SPIE, vol. 5374 (2004)

[15] T. Ogawa, T. Shoki, "EUVL Mask Development: The Current Status", the first EUVL Workshop in Tokyo, May 23 (2001).

[16] P. Yan, G. Zhang, P. Kofron, J.E. Powers, M. Tran, T. Liang, A.R. Stivers, F.-C. Lo, *EUV Mask absorber characterization and selection*, Proc. SPIE Vol. 4066, p. 116-123 (2000).

[17] S. D. Hector, *EUVL masks: requirements and potential solutions*, Proc. SPIE Vol. 4688, p. 134-149 (2002).

[18] L. Dieu, E.L. Fanucchi, G.H. Hughes, D.L. Mellenthin, B. La Fontaine, H.J. Levinson, P.J.S. Mangat, S.D. Hector, and E.A. Delarosa, *EUV Mask Fabrication at the Reticle Technology Center*, First International Symposium on Extreme Ultraviolet Lithography, Dallas, October 14-17 (2002)

[19] Online data of optical constants at Center of X-Ray Optics (CXRO), http://www-cxro.lbl.gov/optical_constants/

[20] T. Pistor, A. R. Neureuther, R. J. Socha, *Modeling oblique incidence effects in photomasks*, Proc. SPIE, Vol. 4000, p. 228-237 (2000)

[21] P. Yan, S. Yan, G. Zhang, P. A. Kearney, J. Richards, P. Kofron, J. Chow, *EUV mask absorber defect repair with focused ion beam*, Proc. SPIE Vol. 3546, p. 206-213 (1998)

[22] Claus Burkhardt, Sven Bauerdick, Volker Bucher, Wolfang Barth, Albrecht Ehrmann, Tarek Lutz, Jenspeter Rau, *Investigation of Low Damage Mask Repair by Combination of Electron Beam and Scanning Force Technology,* Micro and Nano Engineering (2002).

5 Nanoimprint Lithography with clear-opaque mold

5.1 Introduction

Another promising next generation lithography technology is Nanoimprint Lithography [1] which presents a radical new approach to lithography. Many variants of imprint lithography technologies [1-7] were developed and aimed to meet or exceed the technology node targets outlined in the SIA roadmap, while circumventing the expensive sources and optics required by other more conventional projection lithography technologies. One of these technologies is Step and Flash Imprint Lithography (SFIL) from UT Austin, which is based on a dual-layer imprint scheme that utilizes the *in situ* photopolymerization of a low viscosity organic-coated substrate. SFIL is a novel, high throughput, room-temperature, low cost patterning technique with a sub-100 nm resolution capability [8]. Small features down to 20 nm have been demonstrated in research labs using SFIL. But there are still many aspects of the process and issues to be understood and solved before it can be adopted in semiconductor manufacturing.

A revised scheme based on Step and Flash Imprint Lithography was proposed by White and Wood [9]. This scheme replaces the transparent template or mold used in the UT Austin group's approach with a clear-opaque mold, which is similar to the traditional binary masks. This new scheme aims to solve many of the challenges present in etch processing control, alignment control, and defect inspection etc. Rigorous electromag-

netic simulation [10] is extremely valuable in this case as it can quickly assess material selection and design choices.

This chapter starts with a description of the Step and Flash Imprint Lithography process flow and the use of clear-opaque molds instead of transparent molds. Next, the rigorous electromagnetic simulation is applied to model the exposure step in the process flow. The effects of mold feature topography and material properties are discussed. Finally the alignment process is modeled and alignment signals under several use conditions are presented.

5.2 Clear-opaque mold in Nanoimprint Lithography

A sketch of process flow in the original Step-and-Flash Imprint Lithography is drawn in Figure 5-1 (a). At first, an organic transfer layer is spin-coated on a silicon substrate. A surface-treated transparent template with relief structures of circuit patterns is closely aligned just above the coated silicon surface as in step (1). Then a drop of photo-

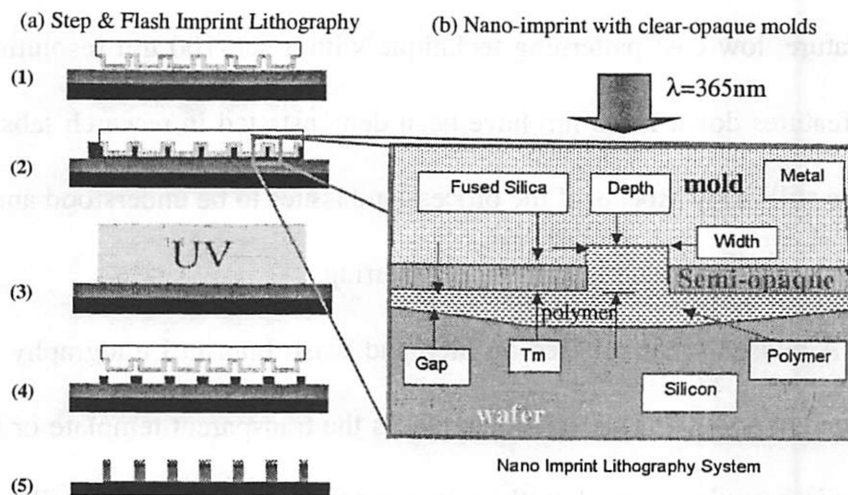

Figure 5-1. The sketch of step-and-flash imprint lithography (a) process flow (b) clear-opaque binary mold.

polymerizable organosilicon solution with a low viscosity fills the gap between the template and the substrate via capillary action, and the template is pushed down to close the gap and make contact with the transfer layer as in step (2). In step (3), ultraviolet (UV) radiation cures the photopolymer. Upon removing the template after curing, a relief image is left on the coated substrate as in step (4). An RIE etch is applied through the transfer layer and creates the final high aspect ratio image on the substrate as in step (5). These process steps appear to be simple but involve many interesting challenges in processing and materials.

In trying to solve some of these challenges, White and Wood proposed a revised scheme with a new type of clear-opaque binary mold as shown in Figure 5-1 (b). In this system, the rigid fused-silica mold is binary in the sense that it has a relief pattern, part of which is semi-opaque and transmits only a few percent of incident UV radiation. For example a thin metal absorbing layer with thickness *Tm* is deposited on the fused-silica mold and features with small widths are etched through the metal layer. The depth of features may equal or exceed the thickness of the metal layer.

The advantages of a clear-opaque binary mold over a transparent mold are that it helps control the CD and facilities mold/substrate separation. With the metal layer, the depth of the features can be controlled much better than by etching into the fused-silica. The metal absorbing regions around features limit the light transmission near the features so that the dimensions of the polymer features after exposure are closer to the dimensions on the mold. The polymer under the metal layer is partially exposed so that it can be rinsed away with a developer without additional RIE etch, which might degrade the features. This results in features of high aspect ratio on a bare substrate, helping to control

feature size, depth, etc during pattern transfer. With a clear-opaque binary mold, in all regions the fully or partially exposed polymer is solidified in such a way that it pulls away from the mold surface yet cling to the wafer. This facilitates the separation of the mold from the wafer less.

The clear-opaque binary mold also introduces several new challenges that must be solved. First, the feature size on the mold is the same as that on the wafer, which is usually in the sub-100 nm region. This size is much smaller than the UV radiation wavelength in the fused-silica so that the transmission through features on the semi-opaque metal layer is greatly reduced, degrading throughput. Second, the near-field transmission of light through features can be highly depended on the topographical properties of the feature such as the feature width, depth, and the metal layer thickness, and the optical properties of the absorber and the mold. These effects are examined in later sections. The performance of the system also depends on the choice of exposure wavelength and gap size between the binary mold and the wafer.

5.3 Modeling exposure process

The electrical fields passing through the mold feature during exposure are very important in determining the final feature profile. An example of an isolated 40 nm feature as shown in Figure 5-1 (b) has been simulated under three conditions: (a) 2D infinite space under TM polarization (b) 2D infinite space under TE polarization (c) 3D hole under both TE and TM polarizations. The following simulation conditions are used throughout this chapter unless otherwise stated. The dimension of the domain are Lx = 600 nm, (Ly = 600 um in 3D cases), and Lz = 300 nm. The node size of the discretization

mesh is $dx = dy = dz = 2$ nm. The gap between mold and wafer is fixed at 20 nm. The typical material used in the semi-opaque metal layer is Cr. The metal layer thickness is 50 nm. The features have a width of 40 nm and depth of 50 nm. The UV light source is described by a wavelength $\lambda = 365$ nm and the light is exicted at the top. At this wavelength, fused-silica has a refractive index of 1.4747, the polymer is assumed to have a refractive index of 1.5, silicon has a refractive index of 6.5282 – j*2.608, and chrome has a refractive index of 1.402 - j*3.257. The reflection output plane is located just above the excitation plane and, for inspection, the transmission output plane is just beneath the complementary metal layer on the wafer.

The simulated electrical fields in the regions around the feature are plotted in a $\log_{10}$ scale in Figure 2. In the 2D TM polarization case (a), the excited electrical field is in the x-direction, Ex, and propagates along the opening inside the metal layer fairly well until it is absorbed by the silicon wafer. The light also penetrates the metal via the skin effect, especially near the feature. There is moderate electrical field excited at the lower boundary of the metal layer and also the light penetration inside metal in this case is

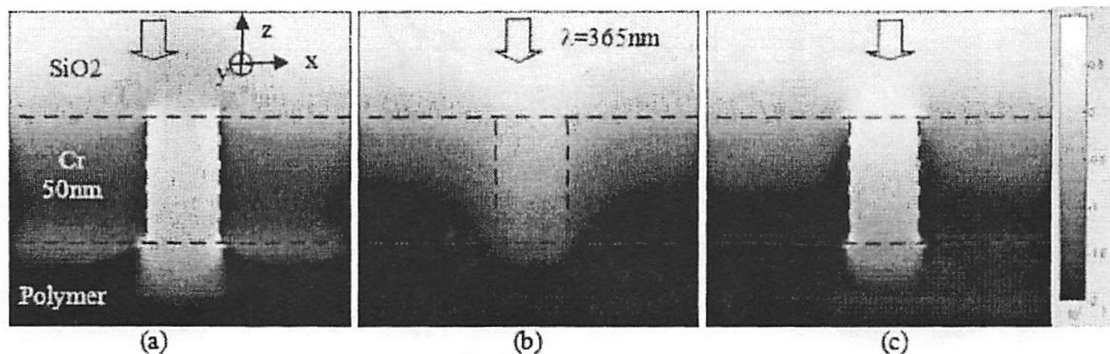

Figure 5-2. The electrical field intensity in the structure of small dimension holes: (a) 2D case with TM polarization (b) 2D case with TE polarization (c) 3D case with TM or TE polarization. The dash lines show the geometry of the hole or line trench.

higher than it is in the other two cases. The higher light exposure around a feature in this case might cause trouble in controlling the line profile especially when coupled with other two cases which can conflict in the same exposure process. In the 2D case (b), the TE polarization puts the excited electrical field in the y-direction, Ey, which can hardly propagates into the trench due to the boundary conditions at the metal edges of the small trench in the metal layer. So the TE polarization may not give adequate light to imprint line features. In the 3D case (c), the circular hole feature gives no preference to the choice of polarization, but due to the small feature size, the light is attenuated when propagating through the hole. Overall, the light intensity in the 3D case is between those of the 2D TM and TE cases, as shown by the field intensites at the center of the feature in Figure 5-3.

5.3.1 Effects of feature topography

The near field transmitted through the clear-opaque molds is closely dependent on the geometry of the hole as the feature sizes are often below the light wavelength. A Se-

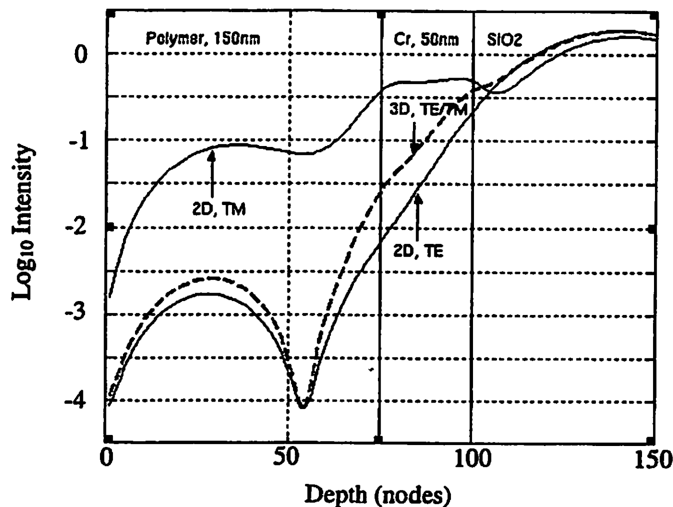

Figure 5-3. Field intensities plotted at the center of the feature.

ries of simulations have been carried out for the 2D feature with sizes varying from 10 nm to 300 nm. The simulation results are shown in Figure 5-4. Here, light under the Cr layer refers to the average light intensity in the polymer in the gap under the Cr layer. Light beneath the feature refers to the average light intensity in the gap beneath the feature opening. Light inside the feature refers to the average light intensity inside the opening etched into the metal layer and the mold.

The light intensity under the Cr layer does not vary greatly overall since this region is far away from the feature. The light intensity beneath the feature is independent of feature size when the size is larger than half of the wavelength. When the feature size is smaller than half of the wavelength, the light intensity beneath the feature decreases linearly for the TE polarization but actually increases for the TM polarization. The light in-

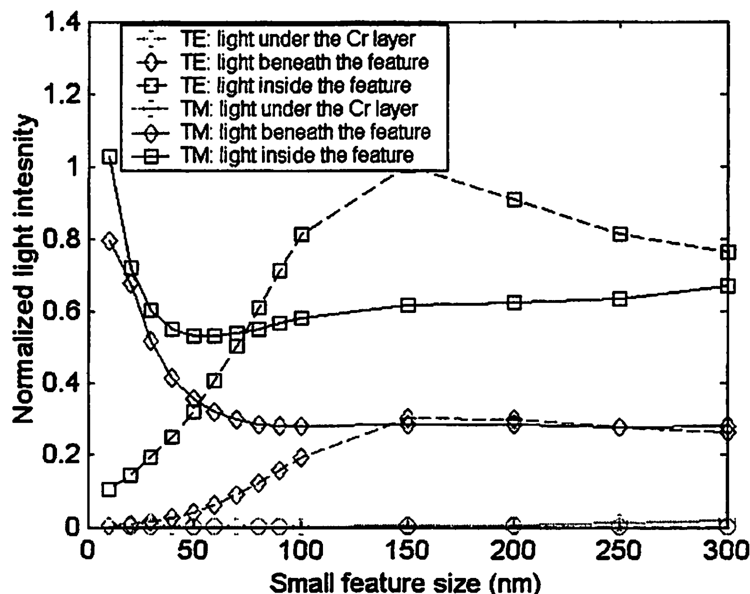

Figure 5-4. The dependence of average light intensities upon the feature size under both TE and TM polarizations.

tensity inside the feature shows a similar behavior but the TE result is larger initially when the feature size is large, indicating a possible resonance effect.

As discussed previously, a 3D hole passes less light than a 2D line feature of the same size. So even with unpolarized UV radiation as source, the light inside the 3D hole is less than that inside a 2D line feature. A coaxial hole was considered to enhance field propagation using the principle of coaxial wave guides. Two cases with core radii of 5 nm and 7.5 nm were simulated and compared with a 3D empty hole simulation with the same outer radius. The results show that there is only a minor improvement of about 10% in light intensity inside the feature but the cost of fabricating the complex coaxial hole structure is high. H-shaped guide might transmit than a coaxial hole.

It is also possible to design additional structures around the main feature to assist the transmission of light, but at the expense of additional fabrication complexities. One suggestion is to over-etch the feature and refill the over-etched volume with a high refrac-

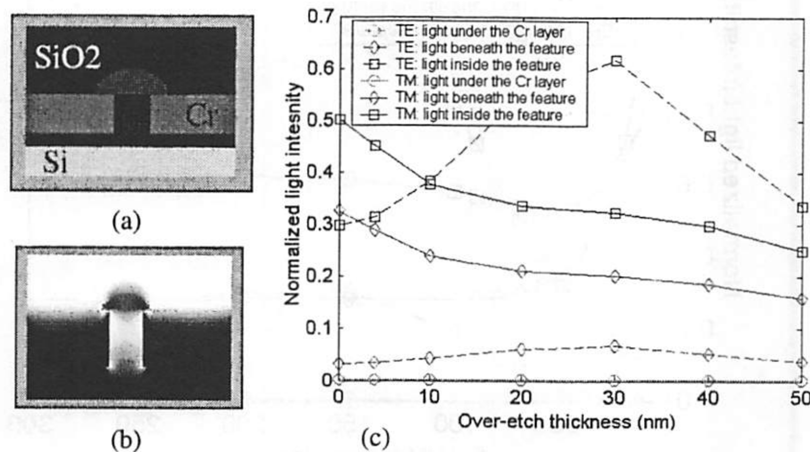

Figure 5-5. Light intensity for an over-etched and refilled structure: (a) topography when over-etch thickness is 10 nm (b) the light distribution and (c) the dependence of average light intensities upon over-etch thickness.

tive index material. The high refractive index material would act as an immersion lens to bring more light to the feature. A series of simulations were applied to such a structure with the over-etch thickness ranging from 0 nm to 50 nm and a refractive index of 2.4 for the refill material. An example of the topography of this structure with the over-etch thickness of 10 nm is shown in Figure 5-5 (a). Figure 5-5 (b) plots the light distribution of this example. Figure 5-5 (c) shows the dependence of average light intensities upon over-etch thickness. Results show that this structure does help the light propagation under the TE polarization while it decreases the light intensities under the TM polarization. This might however be a solution for balancing light propagation of different feature types.

The reduced light distribution inside and beneath the feature is greatly influenced by to the near-field propagation properties of the small sub-wavelength feature. An exponential decay of the light due to the metal layer is expected. It is possible to increase the light intensities by reducing the thickness of the metal layer. The greatest benefit occurs when the metal layer is thinner than the depth of a feature.

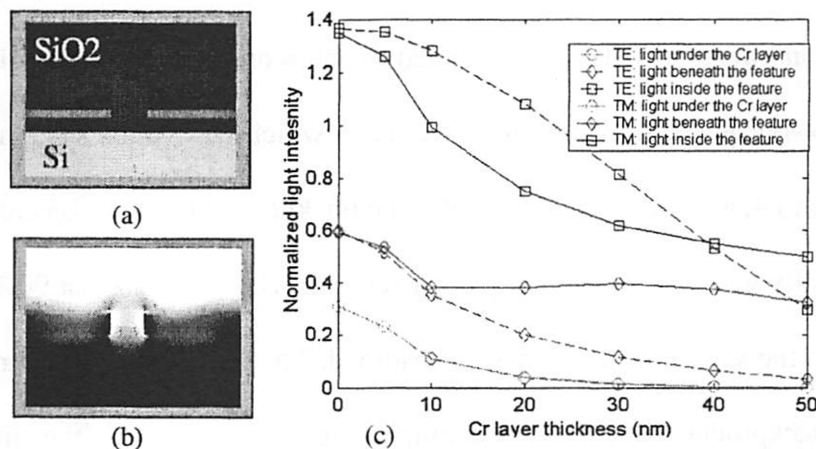

Figure 5-6. Light intensity for a variable thickness Cr layer: (a) the topography when the metal layer thickness is 10 nm (b) the light distribution and (c) the dependence of average light intensities upon Cr layer thickness.

A series of simulations have been run for the metal (Cr) layer thickness ranging from 0 nm to 50 nm. An example of the topography of this structure with the metal layer thickness of10 nm is shown as Figure 5-6 (a). Figure 5-6 (b) plots the light distribution of this specific example. Figure 5-6 (c) shows the dependence of average light intensities upon the metal layer thickness is exponential as expected. The improvement for very thin Cr layers is more effective for the TE polarization case than for the TM polarization case. So using thin metal layer in the semi-opaque binary molds is an effective way to solve under-exposure problems, though the advantage of mold etching control is lost.

5.3.2 Effects of mold material properties

In the new nano-imprint lithography system, different materials are chosen for each component. Of special interest is the key component in the new clear-opaque binary mold, the semi-opaque layer. Besides satisfying microfabrication processing requirements, the absorbing material also needs to meet optical requirements, such as allowing relatively more light collected in the mold feature apertures, to be cost effective,.

To select the best material suitable for the absorber in the opaque layer, series of simulations were carried out for isolated trenches and holes with a typical size of 40 nm. The semi-opaque layer had a refractive index which was varied systematically, such as n from 0.2 to 4, and k from 1.33 to 6.69. The thickness of the semi-opaque layer was varied reciprocally with the imaginary part of refractive index, k, so that 90% of the light incident into the semi-opaque layer was absorbed. The remaining 10% transmission contributes to background exposure. For example, Figure 5-7 (a) shows the simulation geometry when the semi-opaque layer is 50 nm thick with k = 1.33. The near field intensity of this trench simulation is plotted in Figure 5-7 (b). It is noticed that when n is low such as 0.2

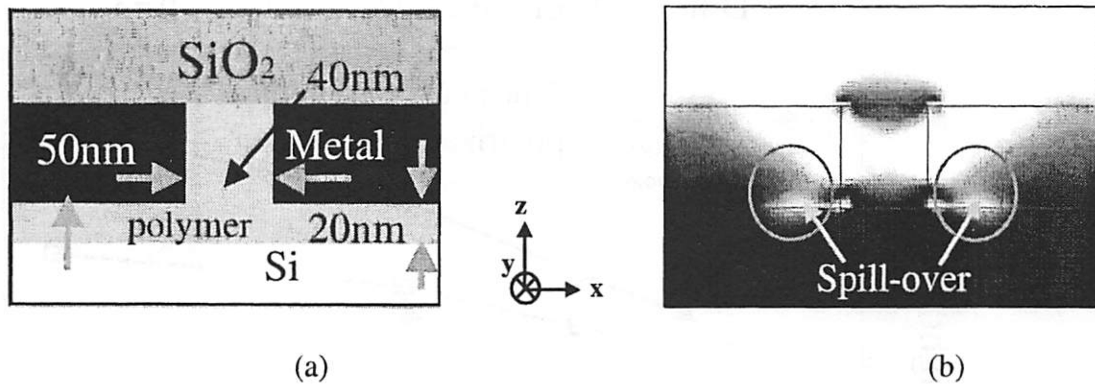

(a) (b)

Figure 5-7. The example clear opaque mold with the semi-opaque layer of n=0.2 and k=1.33: (a) geometry with the semi-opaque layer thickness of 50nm (b) light intensity.

in the case of abnormal dispersion, the light is spilled over into the nearby region of the feature. The intensity of spillover is high enough to expose the polymer so that defects may appear in subsequent processing steps. The physical reason behind this phenomenon might come from excited surface plasmons propagating sideways. When n is higher, the spillover is greatly reduced and remains inside the semi-opaque layer.

The simulation results of semi-opaque layer materials with n = 3 are plotted in Figure 5-8 for the light intensity averaged under the semi-opaque layer in the polymer gap, under the hole feature in the polymer gap, beside the hole in the semi-opaque layer, 40 nm away from the feature, and inside the hole within the semi-opaque layer. The results of other cases with different n values are similar in that all the curves increase with the increase of k or the decrease of semi-opaque layer thickness in the cut planes both parallel to and perpendicular to the incident light polarization direction. Thus the thin semi-opaque layer material with high k helps increase light transmission in the features, and the semi-opaque layer material with high n helps avoid spillover and control feature

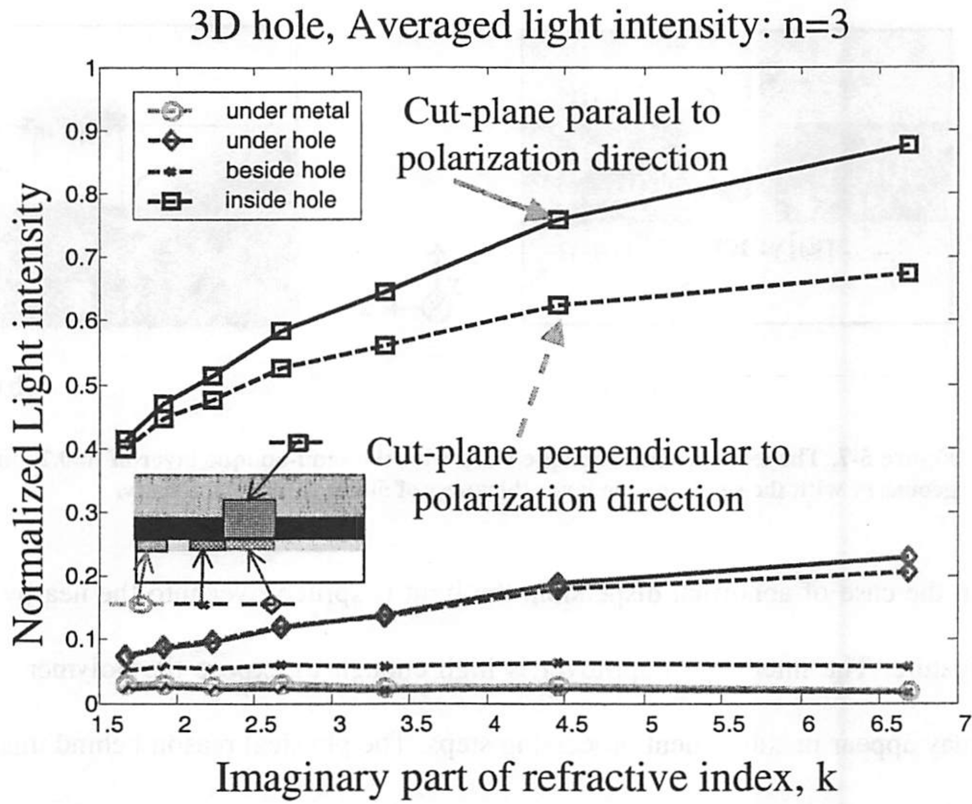

Figure 5-8. The average light intensity at various positions in the 3D hole simulated for opaque materials with n=3 and k from 1.33 to 6.69. (Solid lines are intensity averaged at the cut plane parallel to the polarization direction. Dashed lines are intensity averaged at the cut plane perpendicular to the polarization direction.)

profiles. For this reason, a 24 nm layer of molybdenum, which has a relatively high n & k, was selected for the simulations of defect inspection presented in the next chapter.

5.3.3 Effects of gap size between the mold and the substrate

When the mold is pushed down to the substrate, it is impossible to comepletely close the gap between the mold and substrate. Additionally, this gap size can vary too when considering the substrate is not perfectly flat. Thus the flash step must exposure the polymer under a range of gap size simultaneously. This requires the dose collected during the exposure to remain relatively constant across different gap sizes.

A series of simulations were performed with gap size varying from 10 nm to 40 nm. Examples of the near fields are shown in Figure 5-9. There is a potential problem of spill-over when the gap is as large as 40 nm as in Figure 5-10 (a). Such spill-over into regions near the feature could solify polymer and cause defects. Other than this spill-over problem, the gap has relatively small effect on the average light intensity collected as shown in Figure 5-10 (b). But smaller gaps result in more TE light, thus a smaller gap is perfered. However, there is a practical limit on the gap size set by how close the mold can be pushed close to the substrate. A 20 nm gap is assumed in later sections.

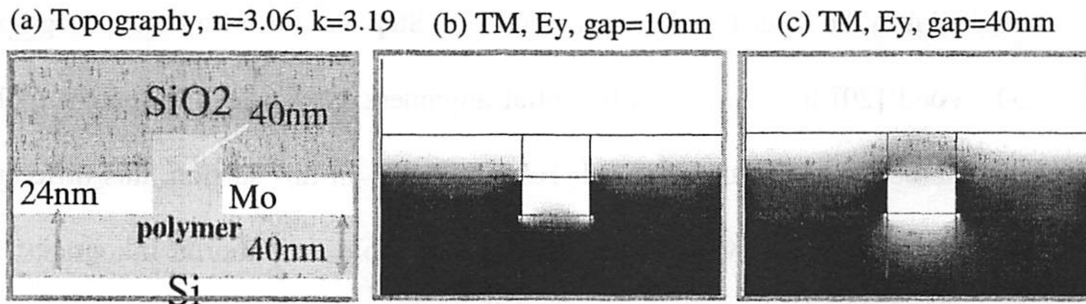

Figure 5-9. The example clear opaque mold with the semi-opaque layer of n=0.306 and k=3.19: (a) geometry (b) Ey intensity when gap = 10 nm (c) Ey intensity when gap = 40 nm.

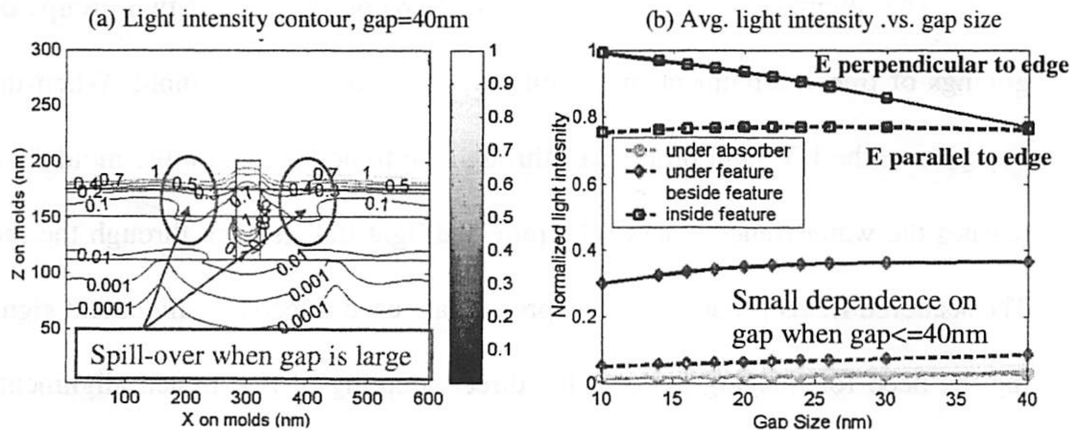

Figure 5-10. Effects of gap size: (a) spill over when gap = 40 nm (b) average light intensity .vs. gap size.

5.4 Modeling alignment process

Alignment at smaller and smaller features sizes is increasingly important and difficult. For example, the baseline alignment accuracy requirement is only a few percent of the wavelength used. Yet line-edge profile shapes and depths are known to significantly affect signal quality and alignment systems must adapt to variations in signal quality. Special care needs to be taken for nanoimprint lithography system as they are targeted to print sub-50 nm features, which are much smaller than the ultraviolet wavelength.

Simulation has been used by many authors [11-18] to analyze electromagnetic scattering from topographies of alignment marks and understand these factors. B. Choi [19] looked into the layer-to-layer alignment for a Step and flash Imprint Lithography system. O. Wood [20] introduced a differential alignment system for transparent mold nanoimprint lithography for the deep sub-100 nm realm. In this section, this differential alignment scheme and its variants for clear-opaque mold nanoimprint lithography system are analyzed using rigorous electromagnetic simulation [21].

5.4.1 Alignment marks on transparent molds

The alignment system proposed by O. Wood consists of two groups of periodic gratings of trench alignment marks on both the wafer and the mold. When the mold is transparent, the UV light propagates through the trench marks on the mold first and then reaches the wafer trench marks. The reflected light travels back through the mold again. The scattered fields produced in this process are used directly as alignment signals avoiding the need for imaging optics. This direct coupling of two trench alignment marks is sensitive to the misalignment so the system can adjust the mold position to balancing the signals in +1 and −1 orders.

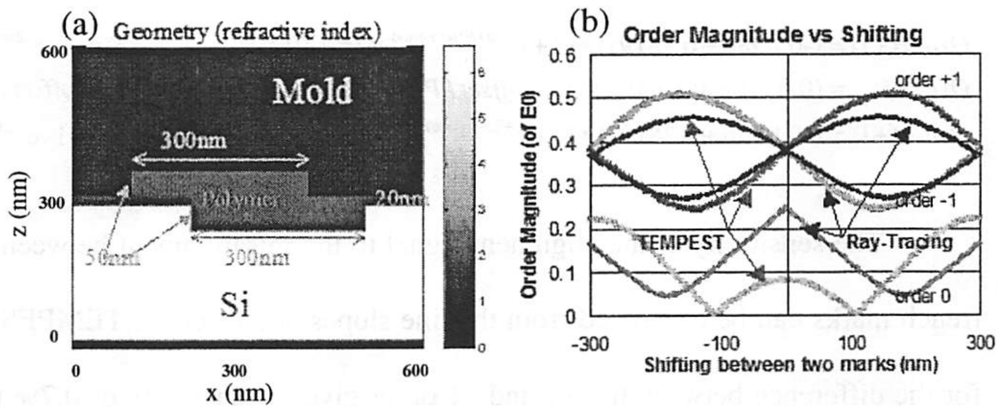

Figure 5-11. Simulation results on alignment marks (a) geometry (b) reflected orders by TEMPEST simulations and ray-tracing analysis.

The design is based on the expectation that the alignment signal imbalance will increase monotonically with misalignment. This dependence was estimated by O. Wood using ray-tracing. TEMPEST has been applied to simulate such alignment mark structures to check the accuracy of the hypothesis. The 2D simulation domain is $Lx = Lz = 600$ nm, and $dx = dz = 2$ nm. Both trenches are 300 nm wide and 50 nm deep. The wavelength used in this alignment system is 365 nm. The mold has refractive index 1.5 and silicon has refractive index 6.592 -j2.703. The space between the mold and the wafer is filled with a polymer with refractive index of 1.9. The mis-alignment between two trenches varies from –300 nm to 300 nm. An example of a misaligned topography is shown in Figure 5-11 (a).

TEMPEST simulation results and the ray-tracing results for the full-period case are shown in Figure 5-11 (b). When there is misalignment a sinusoidal difference occurs between the +1 and –1 diffracted orders. For misalignments smaller than +/- 40nm, the dependence is nearly linearly proportional to the lateral displacement. The ray-tracing analysis [23] gives an analytical expression for the three reflected orders as follows:

$$Order(+1) = (-0.8986 + 0.7819\,\mathrm{i}) * (1 + e^{-2\pi i * \mathrm{offset/Period}})/2\pi + (0.4010 - 1.0786\,\mathrm{i}) * (1 - e^{-2\pi i * \mathrm{offset/Period}})/2\pi$$
$$Order(0) = (0.3376 + 0.3630\,\mathrm{i}) * (1/2 - offset / Period) + (-0.3098 - 0.1152\,\mathrm{i}) * (offset / Period)$$
$$Order(+1) = (-0.8986 + 0.7819\,\mathrm{i}) * (1 + e^{+2\pi i * \mathrm{offset/Period}})/2\pi + (0.4010 - 1.0786\,\mathrm{i}) * (1 - e^{+2\pi i * \mathrm{offset/Period}})/2\pi$$

The sensitivity of the alignment signal to the misalignment between the mold and trench marks can be calculated from the line slopes at the center. TEMPEST simulations for the difference between the +1 and –1 order gives a sensitivity of 0.7% per nm, while ray-tracing predicts 0.5% per nm. The latter is adequate for system design purposes.

Imperfections such as asymmetry in the trench bottom or sidewall with tilted bottom as in Figure 5-13 (a), or asymmetrical sidewalls, will cause an asymmetry between the +1 and –1 orders. The result is that the signal balance point for the two orders will be off-set from the point of perfect alignment. An example of a trench with a 5° slope in the bottom plane is shown in Figure 5-12 (a). Figure 5-12 (b) shows the reflected orders versus misalignment for this trench. The signal balance point for the two orders is off-set from the point of perfect alignment by about 50 nm. But +1 and -1 orders still vary linearly at this balance point, so the differential scheme is still valid.

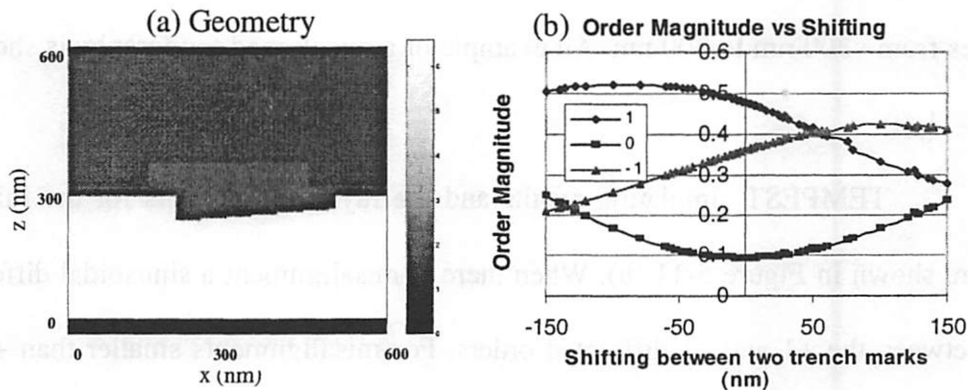

Figure 5-12. Alignment mark with an asymmetrical trench bottom: (a) geometry (b) reflected orders .vs. the misalginment.

5.4.2 Alignment marks on clear-opaque molds during printing

Similar simulations have been carried out after switching the transparent mold to the clear-opaque binary mold. Figure 5-13 (a) shows the geometry when the shifting between the centers of two alignment marks is 250 nm. Figure 5-13 (b) plots the light distribution of this example. Figure 5-13 (c) shows the dependence of reflected orders on the shifting between two alignment marks.

In the plots, the position of 0 nm shifting is when the trench mark on the mold is exactly on the top of the trench mark on the Si wafer, so that two alignment marks leave an opening through two metal layers and the reflected signals are large. The position of a 300 nm or –300 nm shift is when two trench marks are at the complementary position so that they leave no opening except the vertical gap between two metal layers might leak light. As shown in Figure 5-13 (c), the difference between +1 and -1 orders is not strongly depended on the shifting around the zero offset point as had been used for quartz molds. But it is still possible to apply the similar alignment scheme at the 300 nm alignment po-

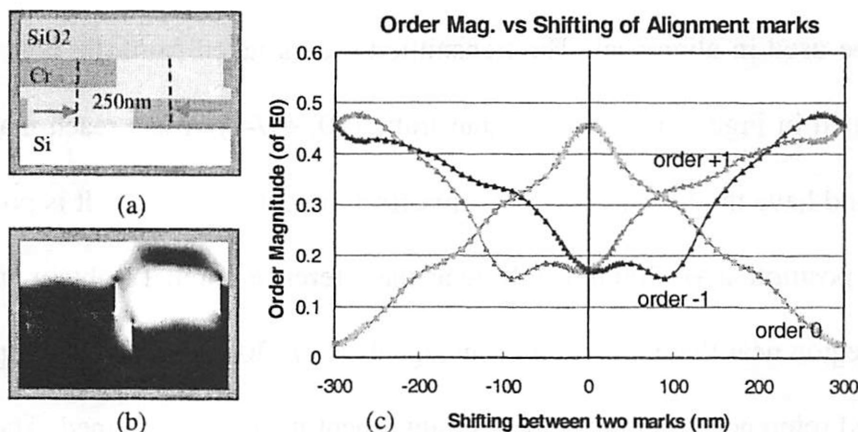

Figure 5-13. Alignments marks on both mold and substrate during printing: (a) topography when the offset of two marks is 250 nm (b) the field distribution (c) diffracted orders reflected from alignment marks.

sition, though the slope there is smaller than that in the case of quartz molds.

Figure 5-13 (c) shows that the 0th order has the maximum at 0 nm offset, and it decreases almost linearly to zero at 300 nm. If the 0th order were used for alignment, it would likely be necessary to misalign intentionally such as using 30 nm in each direction and use the imbalance to determine the correct alignment position. Because the reflected field basically comes from the interference of two waves reflected from two metal layers, the reflected orders such as the 0th order are depended on the roundtrip distance which is twice the trench depth plus the gap height. So the height of alignment marks can be designed to improve the alignment signal.

5.4.3 Alignment marks on clear-opaque molds during inspection

Similar TEMPEST simulations have also been applied to the alignment system for clear-opaque molds during complementary inspection. The simulations results are plotted in Figure 5-14. The reflected orders taken from the top output plane in TEMPEST are plotted in Figure 5-14 (a). They are similar to reflected orders during printing in Figure 5-13 (c). Since the bottom layer is also fused-silica, the transmitted orders are also of interest to be used in alignment. The transmitted orders taken from the bottom output plane are plotted in Figure 5-14 (b). All transmitted (0, +1/-1) orders reach maximum at 0 nm offset and have the minimum at 300 nm offset or –300 nm offset. It is possible to use the nulling position at +/- 300 nm shifting as the reference point. To obtain precise alignment in the region near that point, alignment signals at +/- 30 nm could be compared to find the balanced reference point or the perfect alginment position as defined. The alignment signal could be chosen as the total transmitted light or the 0th order, which both have a strong linear slope with the offset relative to the 300 nm shifted nulling position. Since

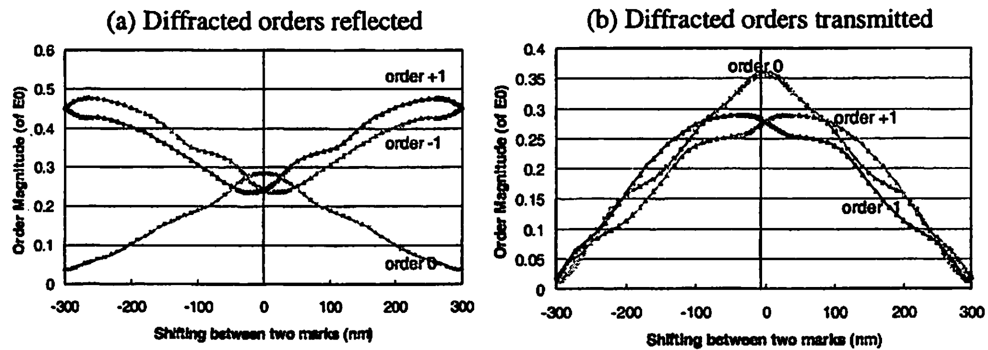

Figure 5-14. Diffracted orders in complementary mold inspection:(a) reflected (b) transmitted.

the residual light at the nulling point is due to the transmitted light through metal layer and the leakage light at the edges of two alignment marks, it is sensitive to the vertical separation of two molds. TEMPEST simulation of two molds separated by 40 nm gap instead of 20 nm gap causes a 100% increase in the 0th order intensity from 0.001 to 0.002 when normalized to the incident light intensity.

5.5 Conclusions

In this chapter, the novel Step and Flash Imprint Lithography process with clear-opaque binary molds is modeled with rigorous electromagnetic simulation.

The effects of feature geometry and mold material properties are analyzed systematically. With the new clear-opaque mold, the small feature size limits light transmission through the mold aperture. While little can be done with auxiliary structures to attract more light into small feature apertures, a thin semi-opaque layer with high k will help increase light transmission in the feature apertures. High n of the semi-opaque layer material can help to avoid defects due to light spillover and have better control of feature profiles. The analysis on the gap size between the mold and the substrate shows the exposure

depends little on the gap size once it is below 40 nm, but potential defects can arise due to the light spillover at large gap sizes.

The differential alignment scheme in nanoimprint lithography is also modeled. Rigorous electromagnetic simulations verify qualitatively the ray-tracing results for alignment marks on the transparent molds. The differential signal between +1 and -1 reflected orders shows a sensitivity of 0.7% per nm of the misalignment compared with 0.5% given by ray-tracing. This sensitivity is reduced if trench profile of the alignment mark deviates from perfection. A slanted substrate indentation will also cause a 10nm offset per degree of tilt. Alignment marks on the clear-opaque molds have more complex diffraction along absorber edges so that +1 and -1 ordes are no longer good alignment signals in the differential alignment scheme, but the nulling position of 0th order can be used instead. Though the small background transmission through the absorber layer and the vertical separation between complementary alignment marks create a leakage signal equivalent to 1 nm misalignment, satisfactory alignment can be obtained by measuring alignment signals over +/- 30 nm range.

5.6 References

[1] Chou, S. Y., P. R. Krauss, P. R. Renstrom, "Nanoimprint Lithography", *J. Vac. Sci. Technol.* B, 14(6), 4129-33 (1996)

[2] Xia Y. and Whitesides G. M., "Soft Lithography," *Angew. Chem. Int.* 37, p.550-575 (1998)

[3] B. Michel, A. Bernard *et al.*, "Printing meets lithography: Soft approaches to high-resolution patterning", *IBM Journal of Research and Development* - Advanced Semiconductor Lithography, Vol. 45, No. 5 (2001).

[4] T. Haatainen, Jouni Ahopelto, Gabi Gruetzner, Marion Fink, Karl Pfeiffer, "Step and Stamp Imprint Lithography using a Commercial Flip Chip Bonder", *Proc. SPIE, Emerging Lithographic Technologies IV*, vol 3997 (2000).

[5] M. Colburn, S. Johnson, M. Stewart, S. Damle, T. Bailey, B. Choi, M. Wedlake, T. Michaelson, S.V. Sreenivasan, J.G. Ekerdt and C.G. Willson. "Step and Flash Imprint Lithography: A new approach to high resolution patterning." *Proc. SPIE,* vol 3676, p. 379 (1999).

[6] M. Colburn, A. Grot, M. Amistoso, B. J. Choi, T. Bailey, J. Ekerdt, S.V. Sreenivasan, J. Hollenhorst and C. G.Willson, "Step and Flash imprint Lithography for sub-100 nm patterning', *Proc. SPIE,* vol. 3997, p. 453-457 (2000).

[7] Chou, S. Y., Keimel, C. and Gu, J. *Nature*, *417*, 835 – 837, 2002.

[8] M.E. Colburn, *Step and Flash Imprint Lithography: A Low-Pressure, Room-Temperature Nanoimprint Lithography*. Ph.D. Thesis. 2001, The University of Texas at Austin.

[9] D. L. White, O. R. Wood II, *A complete system of nano-imprint lithography for IC production, Proc. SPIE*, vol 4688, p. 214-222 (2002).

[10] Y. Deng, A. R. Neureuther, "Simulation of Exposure and Alignment for Nano-imprint Lithography", *Proc. SPIE*, vol. 4688, p. 842-849 (2002)

[11] D. Nyyssonen, "Theory of optical edge detection and imaging of thick layers", *J. Opt. Soc. Am.* Vol 72, no. 10, pp. 1425-1435, Oct. 1982.

[12] G. M. Gallatin, J. C. Wedster, E. C. Kintner, and F. Wu, "Modeling the images of alignment marks under photoresist", *Proc. SPIE, Optical Microlithography VI*, vol. 772, pp. 193-201, 1987.

[13] N. Bobroff and A. Rosenbluth, "Alignment errors from resist coating topography," *J. Vac. Sci. Technol.*, B6 (10), pp. 403-408, 1988.

[14] T. Matsuzawa, A. Moniwa, N. Hasegawa, and H. Sunami, "Two-Dimensional Simulation of Photolithography on Reflective Stepped Substrate", *IEEE Trans. CAD*, vol. CAD-6, no. 3, pp. 446-451, May 1987.

[15] C.-M. Yuan, and A. J. Strojwas, et al, "Modeling Optical Equipment for Wafer Alignment and Line-Width Measurement", *IEEE Trans. Semiconductor Manufacturing*, vol. 4, no. 2, pp.99-110, May 1991.

[16] R. Guerrieri, J. Gamelin, K. Tadros, and A. Neureuther, "Massively Parallel Algorithms for Scattering in Optical lithography," *IEEE Trans. CAD.*, vol. 10., No. 9, pp. 1091-1100, Sept 1991.

[17] G. Wojcik, D. Vaughn, and L. Galbriath, "Calculation of Light Scatter from Structures on Silicon Surface", *Proc. SPIE, Optical/Laser Microlithography*, vol. 772, pp.21-31, 1987.

[18] A. Wong, T. Doi, D. Dunn, and A.R. Neureuther, "Experimental and Simulation Studies of Alignment Marks," *Proc. SPIE*, Vol. 1463, pp. 315-323 (1991)

[19] B. J. Choi, M. Meissl, M. Colburn, T. Bailey, P. Ruchhoeft, S. V. Sreenivasan, F. Prins, S. Banerjee, J. G. Ekerdt and C. G. Willson. "Layer-to-Layer Alignment for Step and Flash Imprint Lithography", *Proc. SPIE,* vol 4343, p. 436-439 (2001).

[20] D. L. White, O. R. Wood, "A Novel Alignment System for Imprint Lithography", *J. Vac. Sci. Technol B*, vol 18, 3552 (2000).

[21] Y. Deng, T. Pistor, A. R. Neureuther, "Rigorous Electromagnetic Simulation Applied in Alignment Systems", *Proc. SPIE*, vol 4346, p. 1533-1540 (2001).

[22] Max Born and Emil Wolf, *Principle of Optics*, Pergamon Press, 1989.

6 Complementary inspection for Nanoimprint Lithography

6.1 Introduction

Imprint Lithography [1-4] promises to be a low cost method to print nanometer scale patterns. But its inherent nature of contacting the wafer raises skeptism that defects will likely appear in the resulting patterns. The defects can occur due to particles or contaminants that originate on the imprint template, bubbles formed between the template and underlayers, features adhering to the template and pulled off from the substrate during releasing.

Relative to other imprinting processes, Step and Flash Imprint Lithgraphy (SFIL) has particular advantages in solving above defect issues. Though these imprint methods all using the topography of the template to define the pattern created on the substrate. SFIL is special in that it uses a transparent and rigid template together with a low viscosity photocurable liquid as the etch barrier [4]. This eliminates the needs of high pressure and high temperature used in other thermal-based imprinting processes, which can cause distortion of the template. The use of etch barrier solutions can entrain those contamination defects on the template thus SFIL effectively is self-cleaning [5]. Though imprinting with untreated templates may result in catastrophic loss of pattern fidelity, the surface treatment reaction can lower the template surface energy so that the solidified etch barrier material can release successfully from the template [6].

However, the SFIL process uses a 1X scale template and thus relatively has higher requirements for features on the template. If it is to be considered as a viable methods for a high density, high throughput semiconductor manufacturing, then tools have to be available to both inspect and repair these templates. Optical inspection [7] for imprint templates with a state of art DUV reticle inspection system was discussed previously by Hess [8]. He also briefly explored the use of e-beam inspection. The complete system of nanoimprint lithography for IC production from White and Wood [9] also covers a complementary inspection scheme with the use of clear-opaque molds instead of transparent templates.

Rigorous electromagnetic simulation with TEMPEST is applied in this chapter to analyze the complementary inspection system [10]. Results from this analysis include in the second part of this chapter the study of improving signals with angular filtering, selection of material properties and immersion [11].

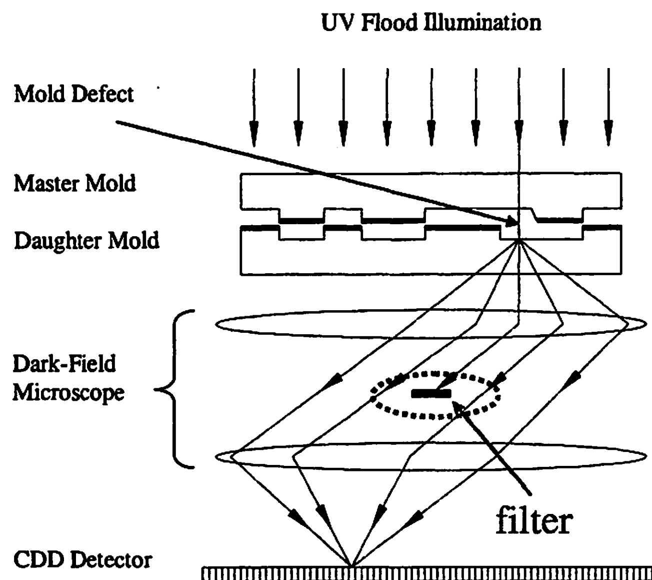

Figure 6-1. A schematic diagram of complementary mold inspection system.

6.2 Complementary inspection of clear-opaque mold

The proposed novel complementary mold inspection scheme is similar to the complementary alignment scheme discussed previously. This inspection system compares features in one mold to those in another supposedly identical mold, but of opposite tone, by placing two molds face-to-face so that they become a nearly opaque bilayer except for the leakages at edges, corners and defects, as shown in Figure 6-1. A pinhole defect transmits extra light during inspection so that a hot spot appears in the image, even though it is not resolvable by the optics. An angular filter at pupil may help improve the signal. The detection limit will depend on the signal to noise ratio obtained from the defects. SEM examination may be performed subsequently at the hot spots to determine if they are true defects. The above detection is only good for pinhole defects. Opaque defects can also be detected by making a complementary daughter mold from the master mold and inspecting pinhole defects on the daughter mold.

An L-shaped gate test structure is designed to test this inspection scheme as shown in Figure 6-2 (a). The test structure is composed of a long gate with length of 240 nm, and an 80 nm square contact. The gate test structures are placed in the center of simulation domain with fixed sizes of $L_x = L_y = 600$ nm, $L_z = 300$ nm and the discretization mesh is $d_x = d_y = d_z = 2$ nm. Two complementary molds are closely placed with a 20 nm gap. The Perfectly Matched layer (PML) absorbing boundary condition is applied on the top and bottom Z boundaries, while a periodic boundary condition is used on the X and Y boundaries. Thus the mask geometry is repeated in X and Y and it will enhance all signals in diffraction orders. This is equivalent to a small illuminated field, but it is a valid approximation to the configuration of inspection system. The semi-opaque layer is 20 nm

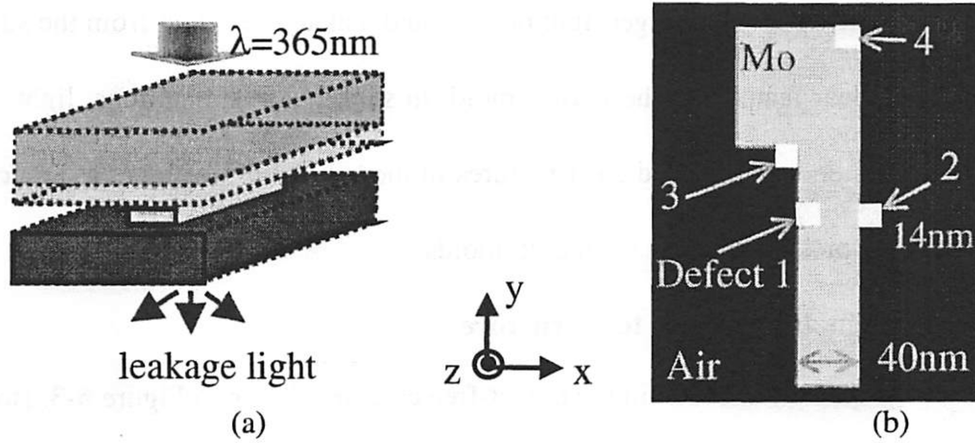

Figure 6-2. The geometry of the L-shaped test structure with defects placed in various positions for inspection.

thick and features are etched to a depth of 50 nm (30 nm in the fused silica substrate). The simulations are done with a 365 nm wavelength light. The semi-opaque layer material is molybdenum with a refractive index of 3.06 –j* 3.19. The fused silica has a refractive index of 1.4747. The inspection optics is assumed to have a NA of 0.95.

The programmed defects have square cross sections with a size of 14 nm, a third of the minimum feature width 40 nm and are also etched 50 nm deep. The pinhole defects are placed in the opaque layer at four positions respectively as shown in Figure 6-2 (b): defect 1 against the middle of left edge of the bottom mold, defect 2 against the middle of right edge of the top mold, defect 3 at the inner corner of the top mold, and defect 4 at the outer corner of the bottom mold.

Since both molds are clear-opaque molds, it is possible to illuminate from either sides of the mold sandwich. To inspect defects in the isolated clear features on the master mold, it is preferred to illuminate from the master mold side rather than the daughter mold side. Otherwise if light were illuminated from the daughter mold, which are the op-

posite tone of the master mold, light would first incident on the large clear regions and there would be a much larger light background leakage than that from the sub-wavelength isolated clear feature on the master mold. In subsequent simulations, light is illuminated from the side with isolated clear features in the test structure. Two inspections from both sides may pick up all defects on both molds.

6.2.1 Signals from gate test structure

Simulation results in the defect-free case are shown in Figure 6-3. Both Ex and Ey components of the transmitted light in the bottom mold under both TE and TM polarized illuminations are plotted. The Ex field under TM polarization has the strongest leakage since the long leg is along the y direction. For the same polarized E fields, the leakage light is highly polarized in the sense that only the edges perpendicular to the incident field

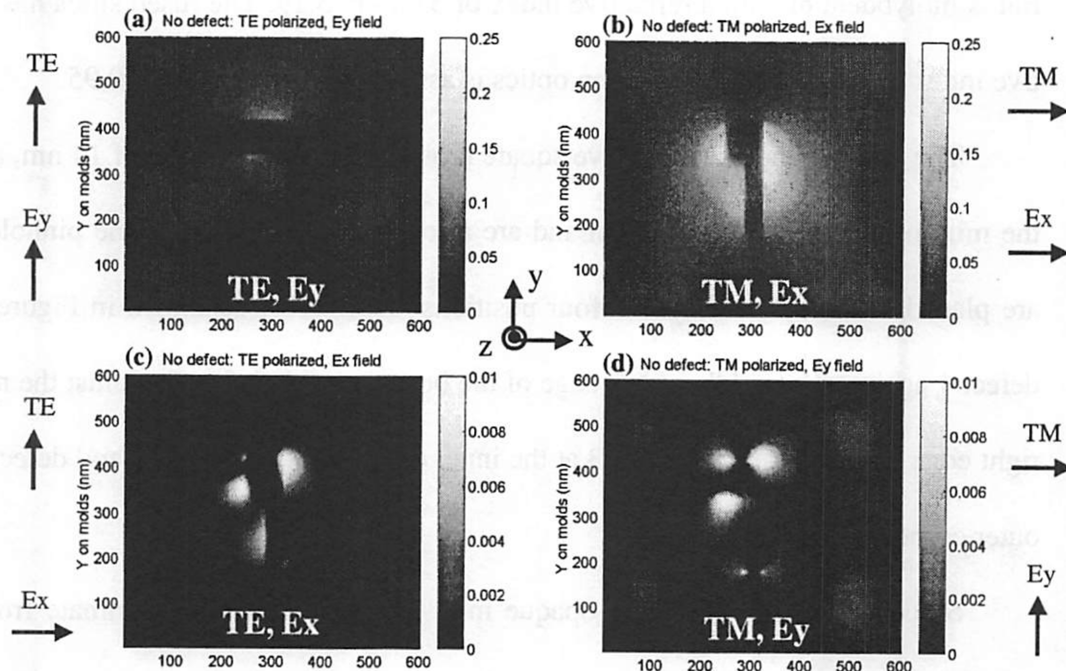

Figure 6-3. The transmitted light intensities in the bottom mold from the test structure without defects: (a) Ey field under TE polarization (b) Ex field under TM polarization (c) Ex field under TE polarization (d) Ey field under TM polarization

direction scatter and leak light in that direction. The strength of leakage light depends on the intensity of light reaching the gap at these edges and increases quickly with the dimensions of these edges. On the other hand, for the cross polarized E fields, the leakage only happens at the corners and is related to the dimensions of edges which are parallel to the incident light field direction.

The test structure with defects is also simulated. For example, Figure 6-4 (a) shows the transmitted near field Ex under TM polarization light when defect 1 is present. There are noticeable difference at defect 1 location compared with the field in Figure 6-3 (b), but they cannot be resolved in far field due to much smaller defect size compared with wavelength. Figure 6-4 (b) shows the angular spectrum from two sandwiched molds. Due the small feature sizes of test pattern, the angular spectrum covers over in a rather large angle range. The diffraction from the main L-shaped features dominates in the intensity and it focuses along kx and ky axises due to Manhattan shapes of main features. However, the diffraction from small defects is much lower and spills uniformly over the pupil.

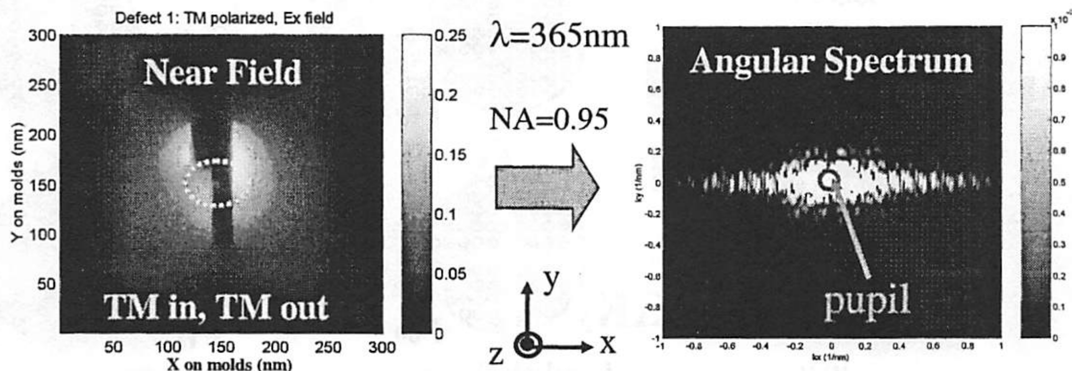

Figure 6-3. The transmitted light intensities in the bottom mold from the test structure with defect 1: (a) Ex field under TM polarization (b) angular spectrum.

6.2.2 Signal enhancement via filtering

As shown in last page, because the features are sub-wavelength and defects are even smaller, defects can be resolved by the optics. But a simple block filter in the center of the lens pupil can reduce the contribution from the main features and improve the signals from defects. Ten filters are used in this section as shown in Figure 6-5.

The first one is the simplest filter (F_0) which only blocks the 0th order. Three filters block signals along the k_x axis with one slice of orders on k_x axis only (F_{x0}), three slices of orders with k_y order number $|n_y|$ <= 1 (F_{x1}), and five slices of orders with k_y order number $|n_y|$ <=2 (F_{x2}) individually. Three filters work along k_y axis (F_{0y}, F_{1y}, F_{2y}) and three filters work along both k_x and k_y axes (F_{00}, F_{11}, F_{22}). The transmitted near fields from simulations for each defect are examined for their angular spectrum and passed through these

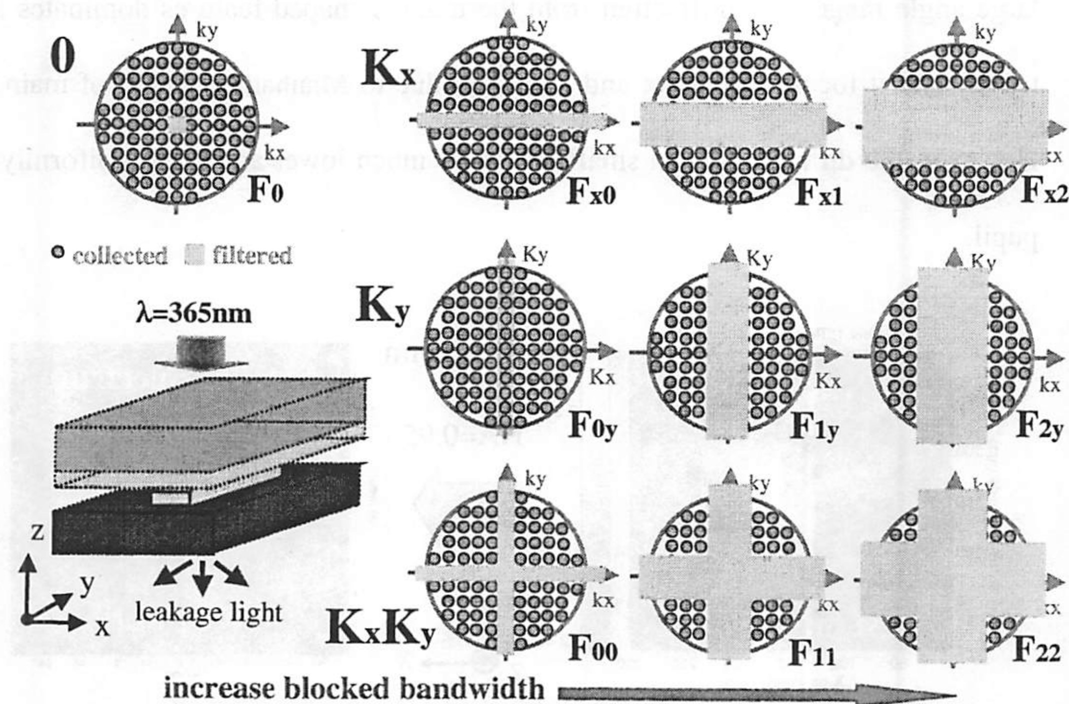

Figure 6-5. The sketch of complementary inspection scheme for clear opaque nanoimprint mold and the sketch diagrams for ten angular filters.

filters, analyzed for the total light energy. The energies remaining after filtering are then normalized to the filtered energies of the defect-free case for each filter individually. The difference of these normalized energies and 1 are referred as the defect signal.

Figure 6-6 shows the analysis results for signals with the same polarization. Defect signals on the edges of line features are more enhanced when they are filtered along the direction perpendicular to the line edges. Defects on the corners have larger signals with filtering along both k_x and k_y axes. The maximum signal after filtering is about 12%. Figure 6-7 shows the analysis results for the cross-polarization signals. Because the cross-polarization light has no 0th order background light, defect signals are large even without filtering. The unfiltered signals for defects on the line edges show that cross polarization

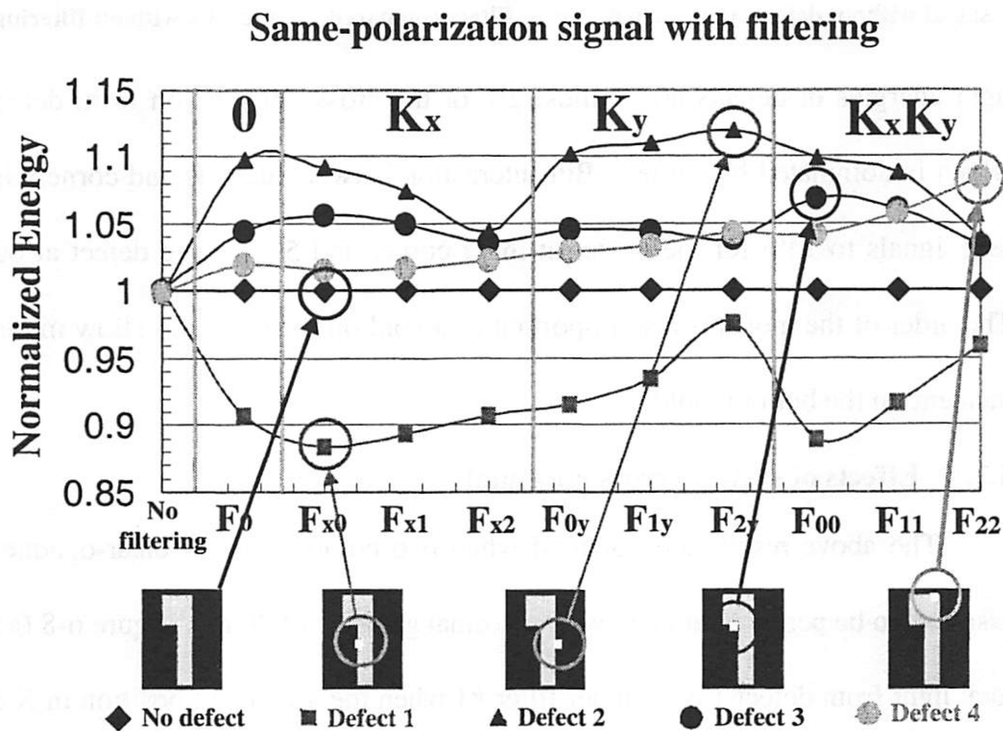

Figure 6-6. The same-polarization light signals from defects at four positions normalized to the signal without defects under ten different filters compared with results without filtering.

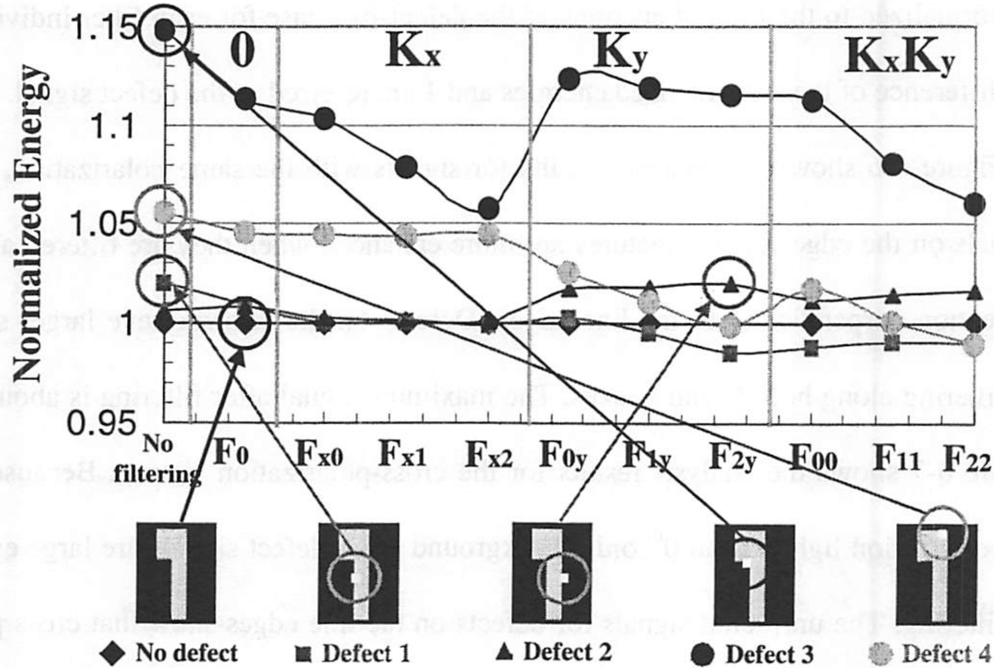

Figure 6-7. The cross-polarization light signals from defects at four positions normalized to the signal without defects under ten different filters compared with results without filtering.

light energies of defects are at most 2% of the cross-polarization from defect free case which is dominated by corners. But interaction between defects and corners increase defect signals to 15% for the defect at inner corner and 5% for the defect at outer corner. The order of the molds is also important as a void on the top mold allow more light to be incident on the bottom mold.

6.2.3 Effects of system errors on signal

The above results are obtained when two complementary clear-opaque molds are assumed to be perfectly aligned with a normal gap size of 20 nm. Figure 6-8 (a) shows the total light from defect 1 case under filter #1 when the alignment position in X direction is shifted from -16 nm to 16 nm. When the two molds are shifted, the filtered transmitted light increases. The asymmetry of curves comes from the asymmetry of the L-shaped fea-

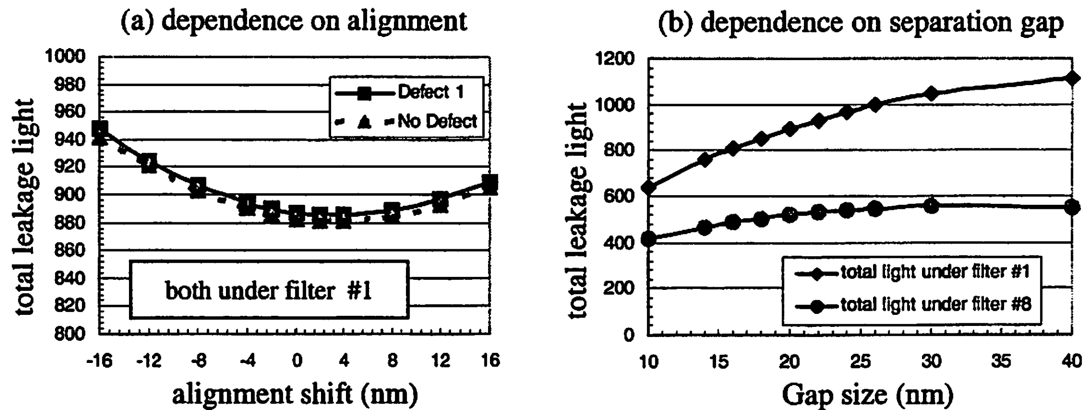

Figure 6-8. (a) Dependence of total light after filtering on alignment position (b) Dependence of total light after filtering on separation gap size.

tures. Two curves vary with each other, so the ratio is not significantly affected. Figure 6-8 (b) shows the total light from defect 2 case under filter #1 and #8 when the gap size is varied from 10 nm to 40 nm. The filtered transmitted light increases with the increase of the separation gap size.

Considering all the system noises, a few percent differences achieved in the earlier analysis are not enough for a good reliable fast defect detection system. But the simulation technique is very useful to further investigate and improve this inspection system. For example at smaller gaps, the leakage light from edges and corners is expected to decrease but the leakage from defect remains at the same level. Although even with an adaptive mold holder [9] two hard molds cannot be very close, a soft opaque resist can be patterned on the daughter mold instead of a hard opaque metal layer so that two mold can be placed very close to each other. Another approach is to use a thicker metal opaque layer with high k which has less transmitted light, but it might also impact the exposure dose and thus throughput.

6.3 Scattering from small defects

Other approaches to improve inspection signals include the use of a shorter wavelength or inspecting with immersion. Light scattering by small defects is simulated and analyzed for the effects of material contrast and wavelength effects with immersion for isolated defects without features. Physical insights of electromagnetic interaction between the incident light and small defects can be drawn from such scattering simulations under different conditions.

The defect scattering study uses light with a shorter wavelength of 193 nm. Series of feature-free defects with a 50nm thickness and square cross sections with sizes from 4 nm to 40 nm are examined as shown in Figure 6-9. These defects are referred as square defects and differ from cubic defects with equal sizes in all three dimensions. These

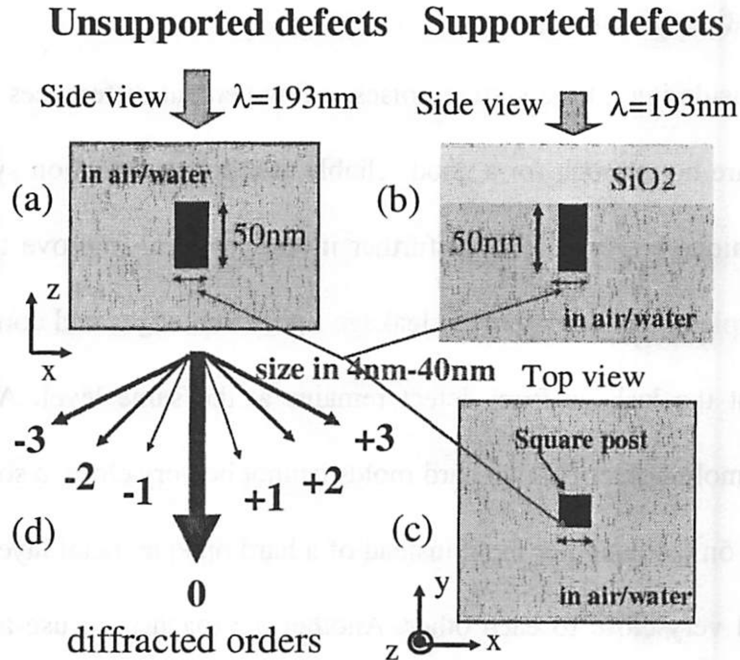

Figure 6-9. The geometries of the small rectangle defects: (a) the side view of unsupported defects (b) the side view of supported defects (c) the top view of defects (d) the sketch of diffracted orders from defects.

simulations. The defect material can be molybdenum with a refractive index of 0.792 - j*2.389, metals with real part of refractive indices varying as 0.8, 1, 1.437 for the study of material contrast (with an imaginary part of refractive index of 2 for absorbing coefficient), or fused silica with a refractive index of 1.5595. Four types of defects are studied: post or void defects unsupported or supported by fused silica substrate. Figure 6-9 (d) shows a sketch of diffracted orders from these defects. Due to the limited size of the simulation domain and the periodic boundary condition applied in the XY plane, only discrete diffracted orders from -3rd to +3rd can be obtained from simulation results. However, these orders still give correct total scattered light integrated over scattered angles. Both small post and void defects are simulated within environment of air or immersion liquid such as water with refractive index n=1.437 or a hypothetical media with higher refractive index n = 1.8. The defect can be isolated or supported by the transparent fused silica substrate.

6.3.1 Effects of defect size on scattering

Figure 6-10 (a) shows the distribution of order magnitudes along k_y axis in pupil space for different sizes of defects with a refractive index 0.8 - j*2. The 0th order dominates the total transmitted light in the normal incident case. The non-zero orders are more of interest for inspection signals. These orders show a same parabolic distribution and increase quadratic ally with defect size. The parabolic distribution occurs because the light is not quite uniformly distributed along the k_x direction due to the aspect ratio of the square post defects. Also the transmitted light consolidates into discrete orders with different solid angles in the angle space. Figure 6-10 (b) shows the largest orders (3rd) as a function of defect area for four types of defects. At small sizes, the order magnitudes are

linear with defect area (or really the defect volume since the defects have fixed thickness). This agrees with classical Rayleigh theory of scattering [12]. When defect size is larger than 20 nm, the order magnitudes are sub-linear owing to the presence of geometrical size effects.

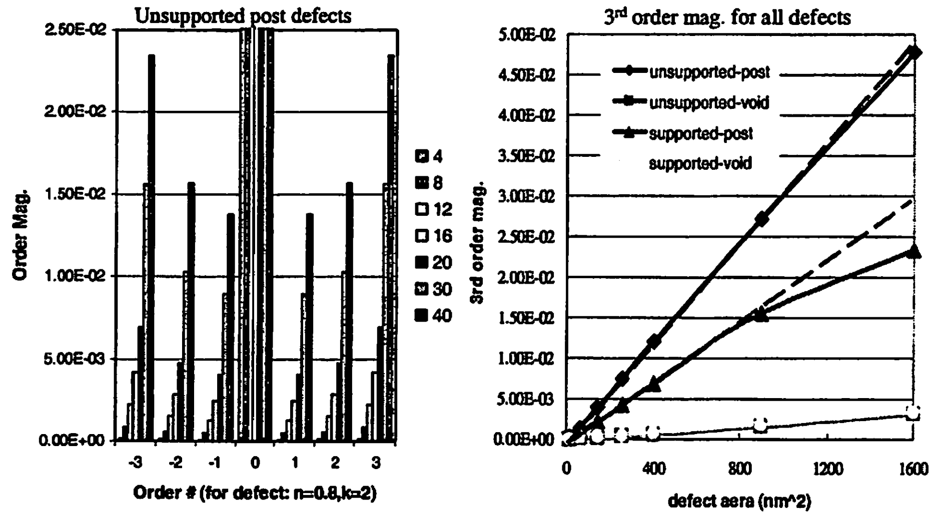

Figure 6-10. Effects of defect size: (a) diffracted orders from a unsupported post defect (b) the 3rd diffracted order magnitude for different defect types.

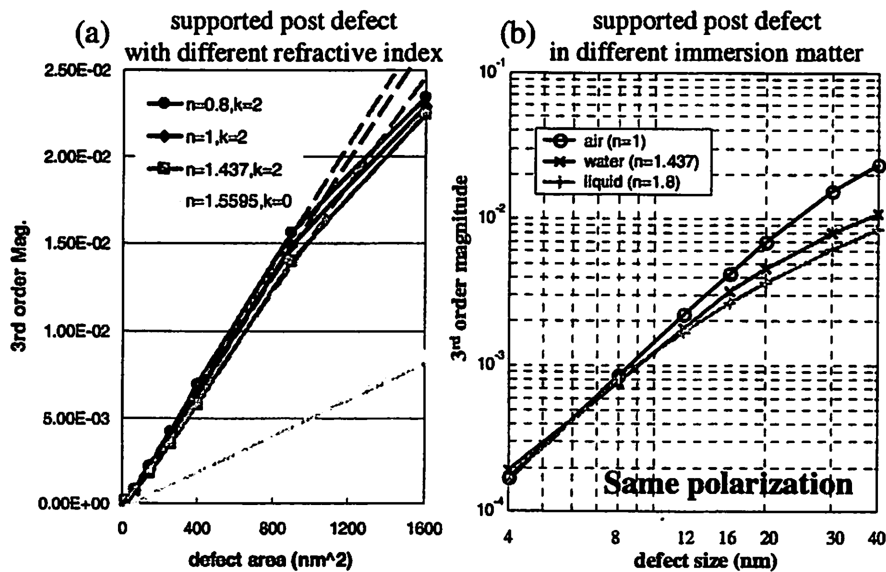

Figure 6-11. Effects of material contrast and immersion: (a) The 3rd diffracted order scaled with defect size for different post defect materials (b) the 3rd diffracted order for the same polarization scaled with defect size for different immersion environments.

6.3.2 Effects of material contrast and immersion

Figure 6-11 (a) shows the 3rd order magnitudes for supported defects with different material properties for normal incidence. The scattered orders decrease as the material contrast decreases, especially for the fused silica defect which has much lower levels of scattered light. Figure 6-11 (b) shows the 3rd order magnitudes for supported defects in different immersion environments. The same polarization signals show little changes in magnitude at small defect sizes and low rates of increase with defect size due to the fact that with immersion defects appear to have larger sizes and begin to increase sub-linearly at smaller sizes.

6.3.3 Effects of incident angle

When the light is off-axis incident such as in Figure 6-12 (a), the forward non-scattered order (+3rd) dominates and there is also a bi-directional scattered order (-3rd) with significant magnitude. Figure 6-12 (b) shows that this bi-directional scattered light dominates the total transmitted light until other defect scattered orders catch up when the defect size is about 16 nm. The off-axis order magnitudes are generally 30% larger than those of normal incident cases. This enhancement indicates that the substrate support provides imaging charges which enhance the radiation and thus increase scattered light signals. For comparison simulations are also run for cubic defects with various sizes. The order magnitudes from such cubic defects increase cubically with defect size as expected.

6.3.4 Effects of wavelength scaling with immersion on total scattered light

The total scattered light energy integrated over non-zero diffracted orders (referred as the total energy) is analyzed for four types of molybdenum defects. Figure 6-13 shows the results for unsupported post defects for the same and cross polarizations. The total

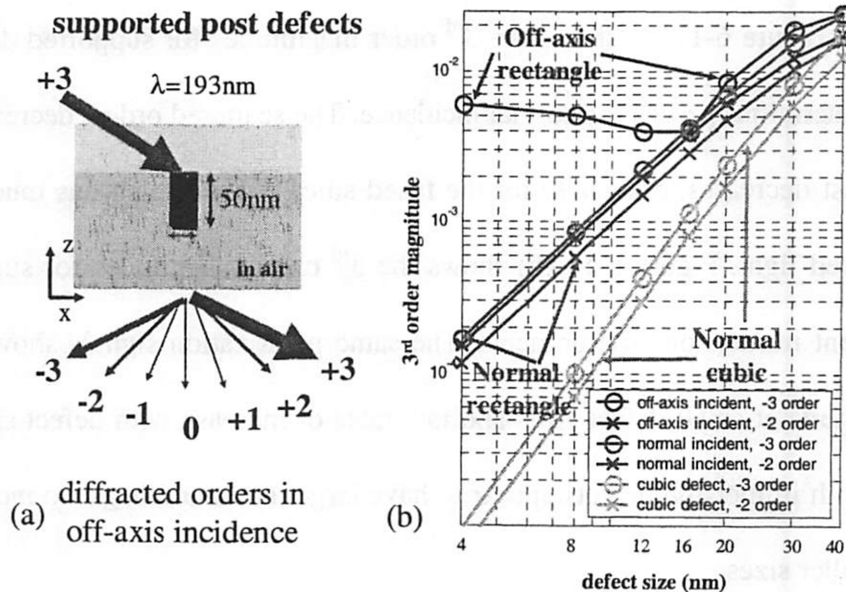

Figure 6-12. Effects of off-axis incident angle: (a) the sketch of diffracted orders from defects (b) the 3rd diffracted order magnitude scaled with defect size for the cases when light is normal and off-axis incident on rectangle defects compared with the case when light is normal incident on cubic defects.

energy is proportional to the defect area^2 or size^4 at small sizes. When the defect size is larger than 20 nm, the total energy goes almost as the size^2. The use of immersion in water increases the total energy of cross polarization roughly by the six power of the refractive index of water 1.437. It shows that the defect is effective 1.437 times bigger for cross polarization. However, the total energy of same polarization is not affected much. Figure 6-14 shows the total energies from supported post and void defects for the same and cross polarizations. They behave similarly when the defect size and the immersion material changes. But the total energies from post are 100 times stronger than those from void defects. One reason is that the void defects have smaller effective scattering area and post defects have larger effective scattering area due to the electrical field boundary conditions. The second reason is that the light is much attenuated when passing through subwavelength void defects in the opaque layer.

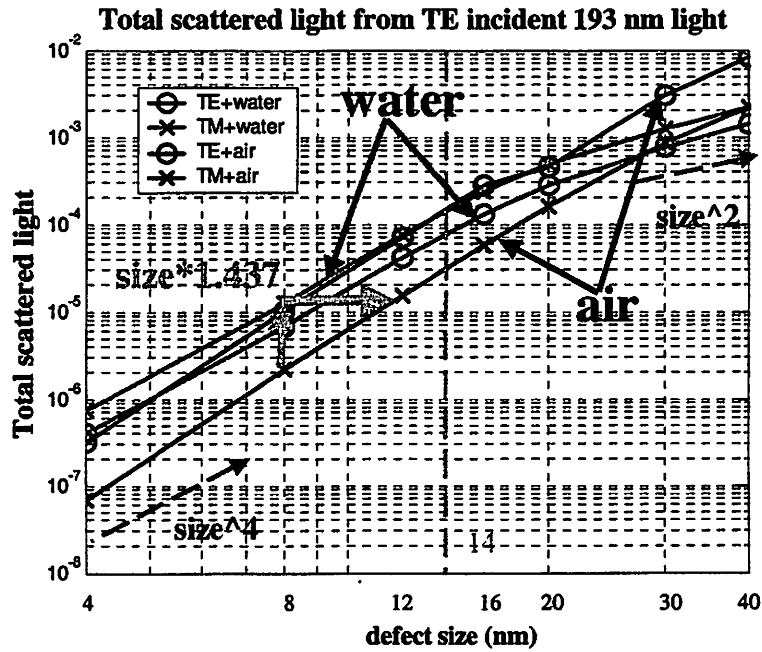

Figure 6-13. The total scattered light of same and cross polarizations for unsupported post defects in air compared with in water.

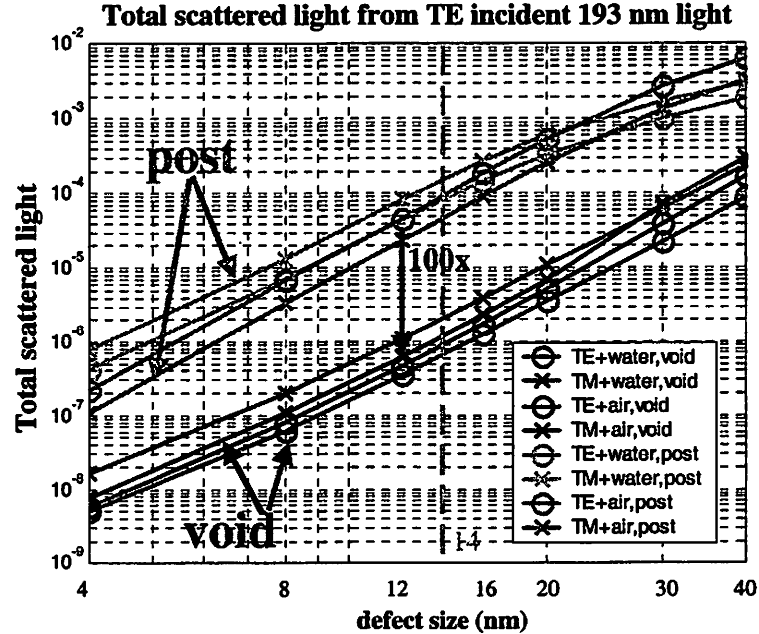

Figure 6-14. The total scattered light of the same and cross polarizations for supported post and void defects in air compared with in water.

6.4 Conclusions

In this chapter rigorous electromagnetic simulation with TEMPEST has been used to study the physical phenomena and quantitative effects in the complementary inspection in Nanoimprint Lithography with clear-opaque molds.

It is shown that the leakage light increases roughly as the square of misalignment and is about 2% for a 10 nm misalignment. The leakage light increases roughly linearly with separation at a rate of about 2% per nm at 20 nm separation. Angular filters can increase defect signals up to 12% for the same polarization, but not very effective on the cross polarization. For the cross polarization, defects on the line edges have small signals about 2%. Due to the interaction between defects and corners, defect signals increases to 15% for the defect at inner corner and 5% for the defect at outer corner.

With a 193 nm light, simulation results on small defect scattering show the classical Rayleigh behavior but geometrical size effects become visible at sizes larger than 20 nm. Scattering signals increase when the material contrast increases between defects and fused silica or immersion liquid. The use of immersion affects little the same polarization light but it increases the cross polarization light because the effective defect size is increased by the refractive index of immersion liquid. This shows an advantage of using cross polarization light as the inspection signal for small defects with immersion.

6.5 References

[1] S. Y. Chou, P. R. Krauss, W. Zhang, L. Guo and L. Zhuang, "Sub-10 nm imprint lithography and applications," *J. Vac. Sci. Technol. B* **15**, 2897 (1997).

[2] Y. Xia, J. J. McClelland, R. Gupta, D. Qin, X.-M. Zhao, L. L. Sohn, R. J. Celotta nd G. M. Whitesides, "Replica molding using polymeric materials: a practical step toward nanomanufacturing," *Adv. Mater.* **9**, 147 (1997).

[3] T. K. Widden *et al*, *Nanotechnology* 7, 447 (1996).

[4] M. Colburn, S. Johnson, M. Stewart, S. Damle, T. Bailey, B. Choi, M. Wedlake, T. Michaelson, S.V. Sreenivasan, J.G. Ekerdt and C.G. Willson. "Step and Flash Imprint Lithography: A new approach to high resolution patterning." *Proc. SPIE,* vol 3676, p. 379 (1999).

[5] T. Bailey, B.J. Smith, B.J. Choi, M. Colburn, M. Meissl, S.V. Sreenivasan, J.G. Ekerdt and C.G. Willson. "Step and Flash Imprint Lithography: Defect Analysis." *J. Vac. Sci. Tech.* B 19(6), p. 2806 (2001).

[6] T. Bailey, B. J. Choi, M. Colburn, A. Grot, M. Meissl, S. Shaya, J.G. Ekerdt, S.V. Sreenivasan, C.G. Willson, "Step and Flash Imprint Lithography: Template Surface Treatment and Defect Analysis", *J. of Vac. Sci. & Technol.* B 18(6), pp. 3572-3577, Nov/Dec (2000).

[7] C. Hung, C. Yoo, C. Lin, W. Volk, J. Wiley, S. Khanna, S. Biellak, D. Wang, Proc. SPIE, vol. 4409, p. 520-531 (2001)

[8] H. Hess, D. Pettibone, D. Adler, K. Bertsche, K. Nordquist, D. Mancini, W. Daukshur, D. Resnick, "Inspection of templates for imprint lithography", J. *Vac. Sci. Technol.* B 22(6), pp. 3300-3305, Nov/Dec (2004).

[9] D. L. White, O. R. Wood II, "A complete system of nano-imprint lithography for IC production", *Proc. SPIE*, vol 4688, p. 214-222 (2002).

[10] Y. Deng, A. R. Neureuther, "Electromagnetic Characterization of Nano-imprint Mold Inspection", *J. Vac. Sci. Technol.* B 21(1), pp. 130-134, Jan/Feb (2003)

[11] Y. Deng, A. R. Neureuther, "Characterization of material contrast and effective wavelength effects in immersion inspection", *J. Vac. Sci. Technol.,* Apr/May (2004)

[12] John D. Jackson, *Classical Electrodynamics*, John Wiley & Sons (1999).

7 Applications in Opto-electronics

7.1 Introduction

Previous sections cover a wide range of electromagnetic applications related to lithography or inspection. But there is no such limit in TEMPEST's capability that it can not be applied to other electromagnetic problems. An interesting question is how well the finite-difference time-domain algorithm in TEMPEST will meet the challenges in these differing types of applications.

Rigorous electromagnetic simulation with TMEPEST was used in the dissertation studies to explore a diverse set of applications, including Opto-electronics structures [1], laser thermal annealing [2], early work on TPF coronagraph pupil masks [3]. The Opto-electronics are 1D and 2D subwavelength gratings and they will be discussed in detail in this chapter. The earlier work on TPF pupil masks was handed over to and is being continued by D. Ceperley [4-5].

Broadband mirrors ($\Delta\lambda/\lambda$>15%) with very high reflectivity (R>99%) are essential for numerous applications, including telecommunications, surveillance, sensors and imaging, ranging from 0.7μm to 12μm wavelength regimes. Metal mirrors are limited by absorption loss, and dielectric mirrors are limited by deposition process and material contrast. It is a challenge to design a mirror with broadband reflection, low loss and compatibility with optoelectronic processing.

Sub-wavelength gratings have been used either to create structures with either sharp highly reflective peaks at resonance wavelengths [6-7] or broad antireflective bands [8]. The final spectral characteristic of the grating can be further tailored by the materials used and parameters chosen.

A novel sub-wavelength grating was proposed by Professor Connie J. Chang-Hasnain's group [1]. This kind of grating has a very broad reflection spectrum and very high reflectivity. Two examples are shown for R>99% with $\Delta\lambda/\lambda$ > 30% and R>95% with $\Delta\lambda/\lambda \approx 50\%$. The design is scalable for different wavelengths. It facilitates monolithic integration of optoelectronic devices at a wide range of wavelengths from visible to far infrared.

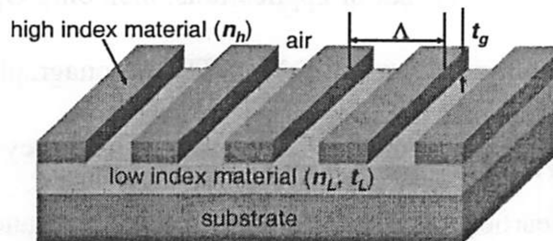

Figure 7-1. Scheme of the 1D sub-wavelength grating reflector. The low index material under the grating is essential for the broadband mirror effect.

7.2 1D sub-wavelength gratings

The proposed structure has a large refractive index difference among materials, resulting in a very broadband reflector. Figure 7-1 shows the scheme of such a mirror that consists of lines of high/low index material surrounded by two low index layers. The larger the difference between high and low indices is, the larger the reflection band. The low index layer under the grating is critical for the mirror effect. Design parameters for the

structure include the materials involved (index of refraction), thickness of the low index layer under the grating (t_L), grating period (Λ), grating thickness (t_g) and fill factor. Fill factor is defined as the ratio of the width of the high index material to Λ.

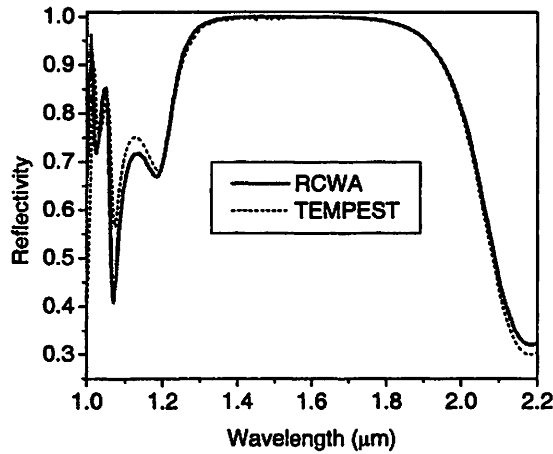

(a)

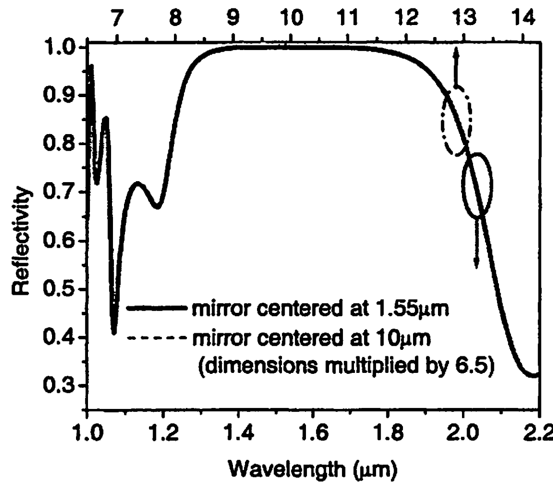

(b)

Figure 7-2. Reflected power for light polarized perpendicularly to the grating lines. (a) Thick line was obtained based on Rigorous Coupled Wave Analysis (RCWA) while dashed with TEMPEST. (b) A simple scaling factor (6.5) applied to the dimensions gives completely overlapped traces. Thick line is centered at 1.55μm while dashed at 10 μm.

Rigorous electromagnetic simulation with TMEPEST was applied to study the reflection signals from such structure. Rigorous Coupled Wave Analysis (RCWA) [9] simulations were carried out by M. Huang. The results from two simulation methods are in excellent agreement. A very broadband mirror $\Delta\lambda/\lambda > 30\%$, with $R > 0.99$, was obtained around 1.55μm, over the range 1.33μm to 1.80μm, as depicted by Figure 7-2 (a). The mirror is also very broad for $R > 0.999$ (1.40μm to 1.67μm or $\Delta\lambda/\lambda > 17\%$). The parameters used in the simulation were: Si substrate (n=3.48), $\Lambda = 0.7\mu m$, $n_h = 3.48$ (Poly-Si), low index material in and above the grating = 1 (air), $n_L = 1.47(SiO2)$, $t_g = 0.46\mu m$ and fill factor = 0.75. The index of refraction was considered constant along the covered range, which is a very good approximation since most semiconductor materials such as Si, GaAs and ZnSe have index of refraction practically independent of wavelength in the considered ranges.

It is interesting to note that the broadband reflectivity does not result from a resonance, as the period of the grating is sub-wavelength but not half-wavelength. Furthermore, the reflectivity spectrum can be scaled with wavelength, as shown in Figure 2(b). By simply multiplying the dimensions by a constant, in this case 6.5, while keeping the other parameters, the reflection band shifts to the 8.6-11.7μm wavelength range with all features and values being identical. Hence, any different wavelength regime can use the same design. Note that the same constant has also multiplied the horizontal scale in order to make the comparison easier. Although it may be obvious that any periodic structure should be wavelength scalable, the scaling here is easily manufacturable since it only requires changing the layer dimensions.

7.3 2D sub-wavelength gratings

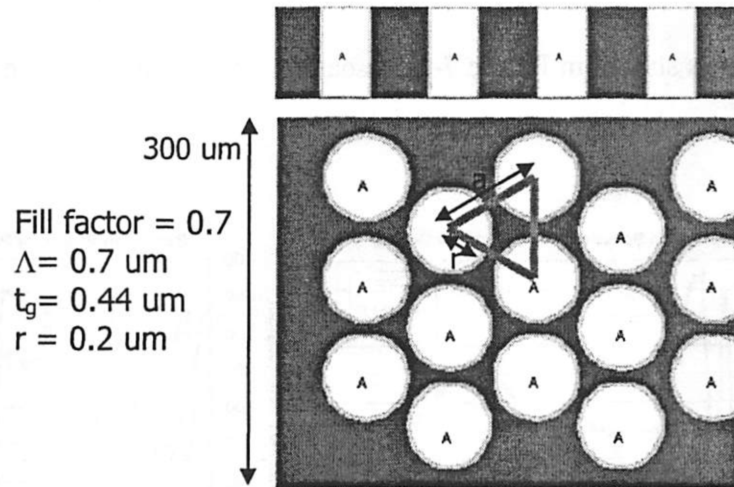

Figure 7-3. Scheme of the 2D sub-wavelength grating reflector.

The 1D subwavelength grating in the previous section works well as a broadband mirror for the polarization perpendicular to the grating lines (TM). However, tfor the polarization parallel to the grating lines (TE), there is no long a broad range spectrum where the gating maintains a high reflectivity. This shows this is highly polarization dependent.

It is of interesting to design a 2D subwavelength grating, which ideally would have polarization-independent high reflectivity in a broadband spectrum as shown in Figure 7-2 (a). A 2D structure with circular holes in a hexagonal array was tested. The design parameters are similar to those of the 1D gratings: the same material properties, $\Lambda = 0.7\mu m$, $t_g = 0.44\mu m$, fill factor = 0.7, and the radius of hole $r = 0.2\ \mu m$.

Figure 7-4 (a) shows the reflection spectrum from such 2D subwavelength gratings for both polarizations. In contrast to the broadband high reflectivity for 1D subwavelength gratings in Figure 7-2 (a), reflections from both polarizations do not have high reflectivity in most regions of spectrum considered. It is interesting that both polarizations

have almost the same reflectivity, though their reflected field phases are quite different. Their reflection spectrum looks more like the reflection from the other polarization from 1D gratings as shown in Figure 7-5. A search through design parameters may get a better result.

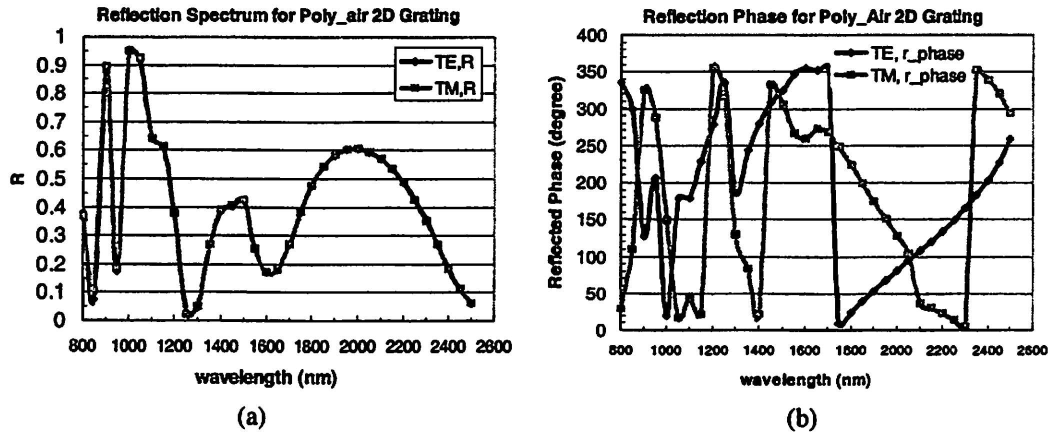

Figure 7-4. TEMPEST simulation results on 2D gratings under both polarizations: (a) reflected power (b) reflected phase.

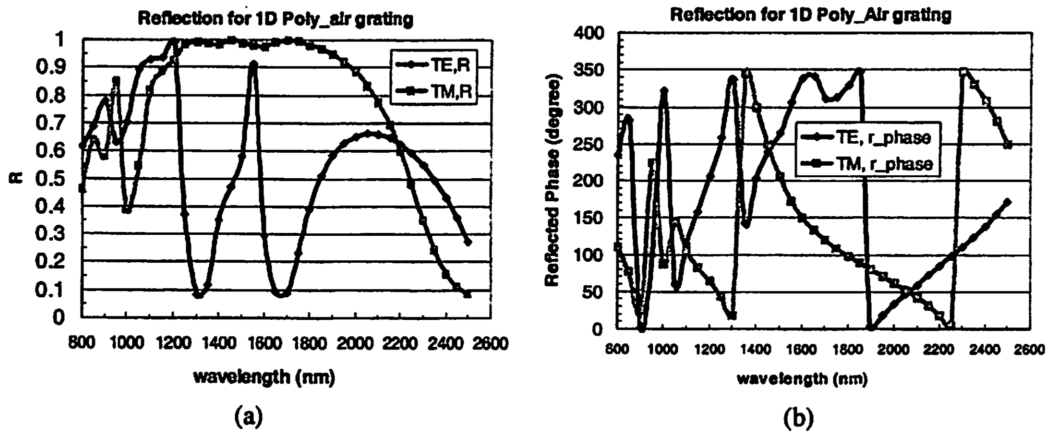

Figure 7-5. TEMPEST simulation results on 1D gratings under both polarizations: (a) reflected power (b) reflected phase.

When running simulations of above 1D and 2D grating structures, it was observed that the electrical fields inside the simulation domain are slow to converge. This is expected as these gratings are high-Q structures and the resonance modes inside the struc-

ture can evolve and do not decay along the time. It is desirable that TEMPEST can extract these resonance modes out and solve for the leaky modes.

7.4 Conclusions

Rigorous electromagnetic simulation was applied to a broad range of applications besides those related to lithography discussed in earlier chapters. This diverse set of applications includes Opto-electronics structures [1], laser thermal annealing [2], TPF coronagraph pupil masks. Only sub-wavelength gratings are presented in detailed in this chapter.

The novel sub-wavelength grating performance is verified through simulations that these 1D sub-wavelength gratings have a very broad reflection spectrum and very high reflectivity. The design is also scalable for different wavelengths. It facilitates monolithic integration of optoelectronic devices at a wide range of wavelengths from visible to far infrared. The extension to 2D sub-wavelength gratings does not fulfill the same properties of these 1D sub-wavelength gratings. However, a search through design parameters may produce better results.

7.5 References

[1] Carlos F. R. Mateus, Michael C. Y. Huang, Yunfei Deng, Andrew R. Neureuther, Connie J. Chang-Hasnain, "Ultra Broadband Mirror Using Low-Index Cladded Sub-Wavelength Grating", *IEEE Photonics Technology Letters*, vol. 16, no. 2, Feb 2004.

[2] Y. Deng, A. R. Nerureuther, internal presentation at UltraStepper, 2003.

[3] Y. Deng, A. R. Nerureuther, *JPL-TPF pupil mask proposal*, 2003.

[4] D. Ceperley, A. R. Nerureuther, M. Lieber, J .Kasdin, and T.-M. Shih, "Vector scattering ananlysis of TPF Coronagraph pupil masks", *Stray Light in Optical Systems: Analysis, Measurement, and Suppression, 5526B, SPIE*, Aug 2004.

[5] D. Ceperley, A. R. Nerureuther, M. Lieber, J .Kasdin, "Characterizing edge generated stray light sources for TPF Coronagraphy pupil masks", *Techniques and Instrumentation for Detection of Exo-Planets, SPIE*, Aug 2005.

[6] R. Magnusson and S.S. Wang, "New principle for optical filters", *Appl. Phys. Lett.* 61 (9), pp. 1022-4, August 1992.

[7] B. Cunningham, P. Li, B. Lin and J. Pepper, "Colorimetric resonant reflection as a direct biochemical assay technique", *Sensors and Actuators B* **81**, pp. 316-28, 2002.

[8] Y. Kanamori and K. Hane, "Broadband antireflection subwavelength gratings for polymethyl methacrylate fabricated with molding technique", *Optical Review,* Vol.9, no.5, pp.183-5, Sept.-Oct. 2002.

[9] M. G. Moharam and T. K. Gaylord, "Rigorous coupled-wave analysis of planar-grating diffraction", *J. Opt. Soc. Am.* Vol. 71, No. 7, pp.811-18, July 1981.

8 Conclusions

8.1 Summary

This thesis discusses the problems related to electromagnetic simulation and modeling applied to broad range of electromagnetic processes in lithography and optoelectronics. With the continuing increase of computation capability and the improvement of physical models built into simulators, simulation and modeling are now frequently replacing experimentation as the initial choice of cost-effective means for testing innovations. They provide a unique capability to explore new technologies when experimental tools are not available yet.

This thesis covers a wide scope of electromagnetic applications, including EUV Lithography, Nanoimprint Lithography, Opto-electronics, laser thermal annealing, and even pupil-plane masks for space telescopes. This diverse set of applications have a wide range of requirements on modeling capability, accuracy and speed for electromagnetic simulation tools, and present a broad range of challenges for the TEMPEST electromagnetic simulation program initially developed for lithography application. These challenges have stimulated the further development of the simulation methodology, and have provided a large set of use cases to test the performance and usefulness of simulation and modeling.

A geometry to refractive index converter, SAM2TEM was developed to link TEMPEST with 3D topography simulation in SAMPLE-3D, and thus extend the capability of electromagnetic simulation to a large range of application involving modeling topog-

raphic changes during process besides the EUV multilayer, such as phase defects in PSM masks.

To address the difficulty of modeling low-profile Gaussian substrate defects in EUV multilayer, the average material properties technique was developed. It provides subcell resolution for the better geometry description and improves the finite difference time domain algorithms with conformal surface modeling. Test cases verified the approximation in using this technique converges to the physical solutions at nearly the same convergence rate of refining the cell size. In other words, the average material properties technique provide almost the same accuracy of refining cell size for curved surface problems and without increasing memory usage and runtime.

A remaining challenge is excessive memory usage and/or long runtimes for 3D TEMPEST simulations with large domain sizes, such as for 3D EUV multilayer structures. Parallel computation was exploited and tested on a large scale network of workstations. Benchmarks on the Millennium Cluster show that on a medium size simulation, a speedup of 6 is obtained when using 10 processors, though the speedup drops when communication and parallelization overhead take over when running with too many processors in parallel. It is expected that the speedup will scale better for large 3D simulations as overhead time becomes a small portion of total computation time.

The combinations of the above enhancements to TEMPEST enable rigorous electromagnetic simulation and modeling of the printability for EUV Gaussian defects. Comparison with Gullikson's analytical model shows his second assumption of coherent illumination limits the model's validity for larger defects, while the third assumption of single surface approximation limits the model's validity for small but relatively high defects.

Further investigation on substrate defect repair shows that e-beam heating can recover multilayer reflectivity almost without image degradation when the process is controlled.

The study of e-beam treated multilayer structures triggered explorations of using d-spacing modified or patterned multilayer directly as photomask in EUV Lithography. Besides the attenuated phase shift mask made from e-beam treated multilayer structures, two new types of multilayer structures, the etched and refilled multilayer masks, are proposed. The analysis of mask diffraction via rigorous electromagnetic simulations shows the intrinsic advantages of etched and refilled multilayer masks.

Further lithography imaging performance studies show that the etched and refilled multilayer masks have better image quality in H-V bias, IPE, smaller CD variations, and larger depth of focus than the normal EUV multilayer masks with absorber stacks, though they are relatively new and facing many processing challenges, such as the control of etch process, defect inspection and repair. During investigation of these problems, a new pattern defect repair scheme on refilled multilayer masks was proposed.

Electromagnetic simulation provides the opportunity to explore new technologies even before conducting initial experiments. This capability is of great value in assessing new technologies for next generation lithography (NGL). One example is the study of the novel Step and Flash Imprint Lithography process with clear-opaque binary molds.

The modeling of the exposure process for this imprint method shows that auxiliary geometry around features help little for feature printing, but the selection of high k material for the opaque layer will help increase light transmission in the feature apertures. High n of the semi-opaque layer material can help to avoid defects due to light spillover and can produce better control of feature profiles.

The modeling of differential alignment scheme used in nanoimprint lithography verifies that complementary alignment marks can be used in nanoimprint lithography systems either with transparent molds or with clear-opaque molds. Alignment marks on the transparent molds perform better in face to face position with alignment signals linearly proportional to misalignment, while alignment marks on the clear-opaque molds have to work on the nulling position which has a small background transmission, though satisfactory alignment can be obtained by measuring alignment signals over +/- 30 nm range.

The complementary inspection in Nanoimprint Lithography with clear-opaque molds was analyzed with rigorous electromagnetic simulation with TEMPEST. Results show at UV wavelength, defect signals are too small even with angular filters, such as maximum 12% for the same polarization or 15% for cross polarization. The leakage light increases roughly as the square of misalignment and is about 2% for a 10 nm misalignment. The leakage light increases roughly linearly with separation at a rate of about 2% per nm at 20 nm separation.

With a 193 nm light, simulation results on small defect scattering show the classical Rayleigh behavior but geometrical size effects become visible at sizes larger than 20 nm. Scattering signals increase when the material contrast increases between defects and fused silica or immersion liquid. The use of immersion affects little the same polarization light but it increases the cross polarization light because the effective defect size is increased by the refractive index of immersion liquid. This shows an advantage of using cross polarization light as the inspection signal for small defects with immersion.

The explorations of applications other than lithography were fruitful but also present new challenges to the existing capability of TEMPEST. The study on subwavelength

gratings demonstrated TEMPEST agrees well with RCWA simulations for 1D gratings, though it did take TEMPEST much longer than normal to converge due to the high-Q nature of these gratings. However, TEMPEST provides the opportunities to study 2D gratings with 3D simulations, and the possibility to investigate effects of topographic changes in manufacturing, such as defects.

In summary, electromagnetic simulation and modeling provides unique opportunities to examine electromagnetic processes for better understanding and to gain physical insights. It also provides guidelines and quantitative design data to explore new technologies or new directions in existing technologies. The diversity of applications shown in this thesis shows the strong capability of the simulator, and the wide usefulness of the simulation.

8.2 Future work

Simulation and modeling will continue to play a key role in developing new photolithography technologies. The use of a flexible FDTD engine coupled with geometry preprocessors and application performance post processors is well suited for initial looks at challenging electromagnetic issues for new applications as they emerge. Alternative approaches or modifications of FDTD for to exploit application specific attributes will likely be required for the computationally intense 3D cases. Computationally, the use of more than 8 multiple processors will be dependent on new developments in communication among processors.

The scope of the use of simulation and modeling will continue to grow with the applications from general purpose tools which augment or aid the process development to frameworks that provide and apply quantitative data in design.